ABSTRACT

Title of dissertation: AN EXPERIMENTAL 2D+T INVESTIGATION OF BREAKING BOW WAVES

Mostafa Shakeri, Doctor of Philosophy, 2005

Dissertation directed by: Professor James H. Duncan
Department of Mechanical Engineering

This experimental research is part of a larger project whose broad goal is to improve our understanding of the dynamics of breaking bow waves including the entrainment of air bubbles into the flow and the generation of turbulence and vorticity. The bow waves studied in this project are generated with a technique known as 2D+T. In this technique, a two-dimensional wave maker moves horizontally and deforms in a manner that approximates the time varying intersection of one side of the hull of the three-dimensional ship and a fixed vertical plane oriented normal to the ships path. Under many conditions, the wave generated by the wave maker breaks by the formation of a plunging jet and creates a turbulent two-phase flow. The specific objectives for this thesis were to construct the wave tank; assemble, test and improve the 2D+T wave maker; develop a technique for measuring the wave profiles; develop a holographic PIV technique for measurement of bubble size distributions and motions; and to measure and analyze the surface profile histories of the wave system as a function of the equivalent forward speed of the ship model.

Measurements were performed for ship model profiles simulating a realistic ship. The histories of the surface profiles of the breakers were measured with a photographic technique that employs a laser light sheet, fluorescent dye and a high-speed digital movie camera. The images record the wave profile at the center plane of the tank where the light sheet intersects the water surface. The results of the measurements include observations of the main features of the wave patterns, plots of the entire wave pattern around the equivalent ship model, and the time histories of various geometric parameters including the contact point of the water surface on the hull, the wave crest, the plunging jet and the splash created by the jet impact. A scaling study was made to examine the effects of the ship speed on these geometric parameters.

AN EXPERIMENTAL 2D+T INVESTIGATION OF BREAKING BOW WAVES

by

Mostafa Shakeri

Dissertation submitted to the Faculty of the Graduate School of the
University of Maryland, College Park in partial fulfillment
of the requirements for the degree of
Doctor of Philosophy
2005

Advisory Commmittee:

Professor James H. Duncan, Chair/Advisor
Professor John D. Anderson
Associate Professor Kenneth T. Kiger
Professor Michael Ohadi
Professor James M. Wallace

DEDICATION

To my parents

ACKNOWLEDGMENTS

I would like to express my deepest gratitude and sincere thanks to Dr. James H. Duncan for his encouragement, support and guidance during the course of this study. Over the past several years, Dr. Duncan has shown many of the best academic qualities which I admire and respect deeply. I would also like to thank Dr. John D. Anderson, Dr. Kenneth T. Kiger, Dr. Michael Ohadi, and Dr. James M. Wallace for serving on my dissertation committee.

I am very grateful to my senior colleague Dr. Xinan Liu for his invaluable help and suggestions during the course of this project. I would like to express my special thanks to Ms. Jessica R. Walters for helping in image and data processing. I also wish to thank my co-workers and colleagues in Hydrodynamics Laboratory Ms. Sonja Haux, Mr. Amir Pouyan Nejadhashemi, Ms. Nathalie Behn, Mr. Rainer Mintzlaff, Mr. Sven Goll, Ms. Mark Bystry, Mr. Raphael Murswieck, Mr. Mohammadreza Tavakolinejad, and Mr. Peter Kang. Their help is highly acknowledged.

Many thanks go out to my parents without whom I would never have been able to pursue this work.

Financial supports rendered by National Science Foundation and the Office of Naval Research through the grant and the University of Maryland are gratefully acknowledged.

TABLE OF CONTENTS

LIST OF FIGURES

NOMENCLATURE

b	Beam of a ship: width of the ship at mid-ship and the mean water line
d	Draft of a ship: vertical distance from the mean water level to the lowest point on the keel
F_r	Froude number
f_1, f_2	Focal distances of the camera
g	Gravitational acceleration
H	Water depth in the wave tank
L_m	Equivalent three-dimensional ship model length at the water contact line
P_g	Point in the grid reference frame
P_c	Point in the camera reference frame
P_u	Point on the image plane projected from the camera coordinate system
R	Rotation matrix in going from the grid reference frame to the camera reference frame
T	Coordinate vector of the origin of the camera reference frame in the grid coordinate frame
t	Time
t_0	Wave maker motion time
u	Fluid velocity in the transverse direction (y-direction)
v	Fluid velocity in the vertical direction (z-direction)
u_i	Horizontal component of the jet tip velocity at the time of impact on the free surface
u_m	Speed of a ship model
u_{max}	Maximum speed of the wave maker top channel
u_s	Speed of a full-scale ship
v_i	Vertical component of the jet tip velocity at the time of impact on the free surface
v_j	Jet tip impact speed on the free surface
x	Distance in the streamwise direction in an equivalent ship coordinate system centered at the point where stem meets the water level
y	Distance in the transverse direction in an equivalent ship coordinate system centered at the point where stem meets the water level
z	Distance in the upward direction in an equivalent ship coordinate system centered at the point where stem meets the water level
(x, y)	Hinge point coordinates of the four-bar linkage
(x_1, y_1)	Position of point 1 on the four-bar linkage

(x_2, y_2)	Position of point 2 on the four-bar linkage
(x_g, y_g, z_g)	Grid reference frame centered at O_g
(x_c, y_c, z_c)	Camera reference frame centered at O_c
(x_i, y_i, z_i)	Image reference frame centered at O_i
α	Jet tip impact angle relative to the undisturbed water surface
δ	Angle between the wave crest line and the equivalent ship model centerline
ΔT_m	Equivalent time of the passage of the stern of the ship model
ΔT_w	The time over which a wave traverses the length of the wave tank from the wave maker to the far end and return
$\delta_{bearing}$	Actual position of the wave board
δ_{model}	Desired position of the wave board
θ	Angle between link a and link b in the four-bar linkage

Chapter 1

Introduction

1.1 Definition and properties of breaking waves

The study of breaking water waves is of great practical and scientific interest. Wave breaking plays a number of important roles in air-sea interaction including limiting the height of the surface waves; generating ocean currents; enhancing mass, momentum, and energy transfer between the air and water; dissipating surface wave energy; generating vorticity and turbulence in the upper ocean; entraining air; and generating spray. Likewise, breaking waves have a significant influence on the response of remote sensing systems that attempt to monitor ocean conditions from satellites and aircraft. Large breaking waves constitute a tremendous threat to ships and engineering structures in the deep-ocean and coastal regions.

There are two major types of breakers: plunging and spilling. The most dramatic breakers are plunging breakers. In these waves, the breaking commences when a forward moving sheet of water (jet) plunges down from the crest onto the front face of the wave causing splashing, air entrainment, and turbulence. In spilling breakers, turbulence appears spontaneously at the crest due to poorly understood mechanisms. This turbulent fluid then spills down the front face of the wave, en-

training air and creating water drops as it spills. In waves with small wavelengths, surface tension tends to prevent drop and bubble formation.

Waves can break in deep water due to a variety of effects including inherent instabilities of deep water waves, wave-wave interaction, wave-current interaction, wind-wave interaction, or steepening due to external bodies such as ships. These latter breakers are somewhat simpler than wind waves since, in a calm sea, the forcing motion is well defined and there is no vorticity in the water except for that found in the breaking zone itself.

1.2 Importance of ship generated breaking waves

Strong breaking waves occur near the bow and stern of naval combatant ships moving in calm water. The character of the breakers depends on many factors including the speed of the ship, the shape of the hull, and the distribution of weight in the ship. Photographs of breaking wave fields around two naval combatant ships moving at high speed are shown in Figure 1.1 and 1.2. In both photographs, the breaking initiates in the form of a large plunging jet that originates as a sheet of water, climbing up the hull just aft of the stem. Breaking waves have a number of important consequences for combatant ships. First, the breakers convert energy from the mean flow into energy in the turbulent flow in the wakes left behind the breakers. This energy is supplied by the engine of the ship. Second, the breakers create underwater sound due to the bubbles that are entrained. Finally, the breakers create wakes that might be detectable by various above and below surface sensors,

thus making the ship vulnerable to attack.

Figure 1.1: A photograph of a US Navy Frigate showing a strong plunging breaker formed in either side of the bow.

1.3 The 2D+T concept

In the 2D+T technique, a two-dimensional wave board is deformed to mimic the time-varying intersection of a fixed vertical plane and one side of the ship hull as it moves at constant speed in a direction perpendicular to the plane. Wave maker profiles at various times (t) represent the hull profiles at various streamwise locations ($x = Ut$). The 2D+T approximation is useful for slender hulls, where streamwise gradients of relevant flow quantities are small compared with vertical and transverse gradients.

In this study, we used the 2D+T concept to simulate a 5415 ship model. Figure 1.3(a) shows a drawing of the 5415 ship model and 1.3(b) shows a photograph of

Figure 1.2: A photograph of a US Navy Frigate showing a plunging breaker forming from the bow.

the model. A series of profiles of one side of the model hull at different streamwise stations from stem to mid-ship are plotted in Figure 1.4. In the 2D+T technique, these profiles would represent the shape of the wave maker surface at various times. It should be mentioned that for this study the bulb of the model (see Figure 1.3(b) and 1.4) was not simulated since it is not well represented by slender ship approximation.

1.4 Objectives

This thesis is part of a larger project funded by the Office of Naval Research. The broad goal of this larger project is to improve our understanding of the dynamics of breaking bow waves including the relationship between the breaker and the hull shape and Froude number, the entrainment of air bubbles into the flow, and the

(a)

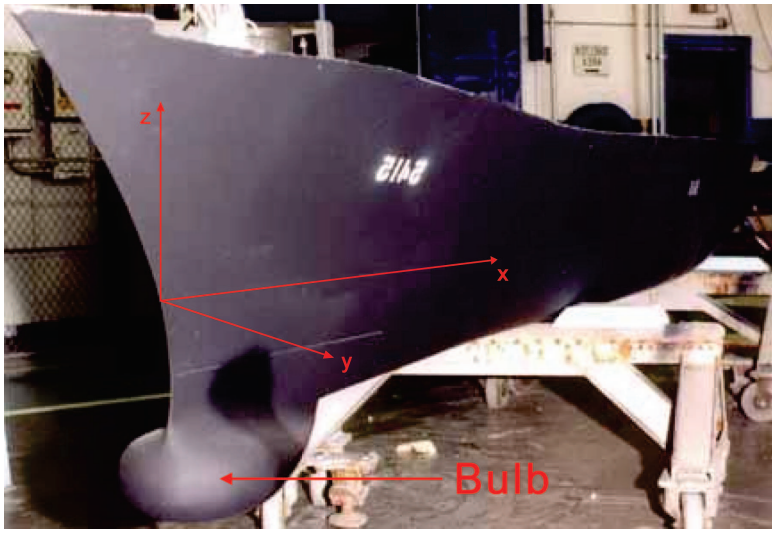

(b)

Figure 1.3: Ship model 5414: (a) drawing and (b) photograph.

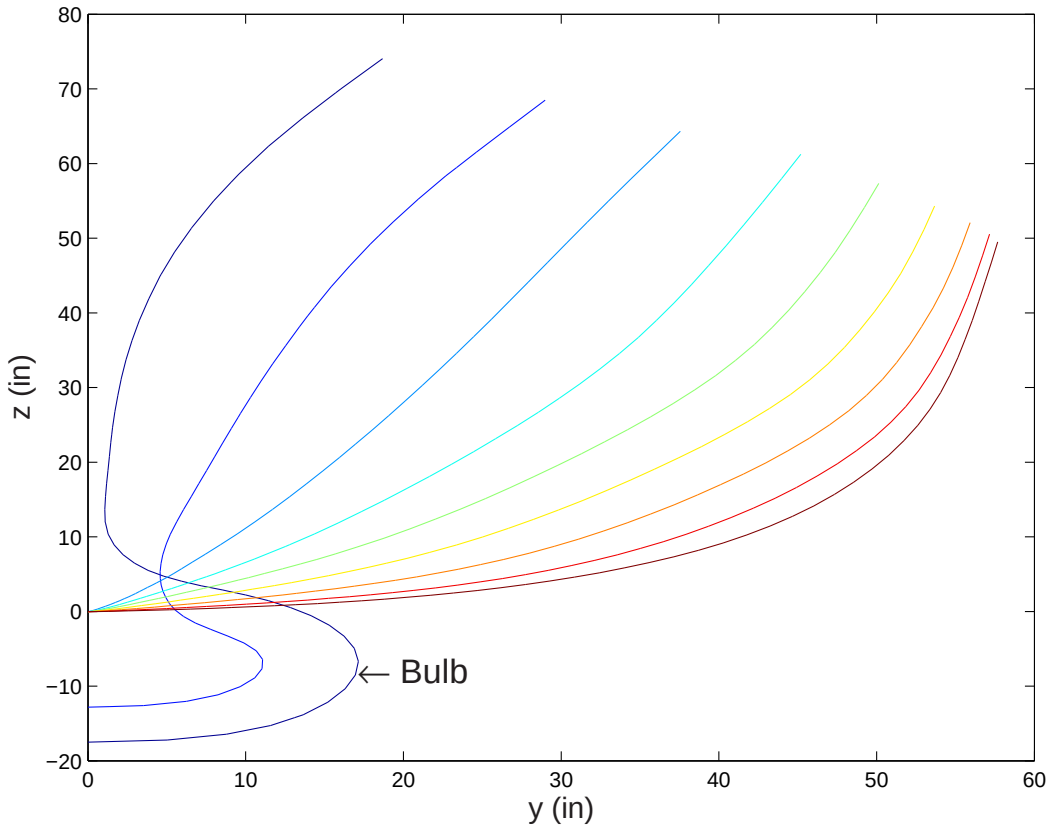

Figure 1.4: Profiles of the 5415 ship model at various stations from stem to mid-ship.

generation of turbulence and vorticity. For reasons discussed later, the bow waves studied in this project are generated with the 2D+T technique discussed above. The specific objectives for this thesis are to construct the wave tank, construct and test the 2D+T wave maker, adapt a laser induced fluorescence technique for measuring the wave profiles, develop a holographic technique for measurement of bubble size distributions and motions, and to measure and analyze the surface profile histories of the wave system as a function of equivalent forward speed of the ship model.

1.5 The dissertation outline

This dissertation is divided into six chapters. In Chapter 2, the literature on aspects of breaking waves relevant to the present work is reviewed. Five major areas are covered including three-dimensional steady breaking ship bow waves, two-dimensional steady and unsteady breaking waves, 2D+T approximations of breaking ship bow waves, and finally air entrainment due to the wave breaking. In Chapter 3, the test facilities, measurement techniques and procedures for the research are described. The development of a holographic particle image velocimetry (HPIV) system is presented in Chapter 4. This technique will be used in future work to measure the size distributions and motions of bubbles entrained in the flow. The results of the surface profile history measurements are presented and discussed in Chapter 5. Finally, the conclusions of the research are given in Chapter 6 along with a description of future plans for the 2D+T project.

Chapter 2

Related studies on breaking waves

2.1 Three-dimensional steady breaking ship bow waves

The wave pattern around the bow of a ship mainly depends on the shape of the ship, the distribution of weight inside it, and the Froude number, $F_r = U/\sqrt{gL}$ where U is the ship speed, g is the acceleration of gravity and L is the ship length along the calm water line. For blunt shapes, breaking occurs ahead of the bow, whereas for fine ships with a sharp stem, the free surface flow moves upward on each side of the hull and this water motion contributes to the formation of bow waves which break for high ship speeds.

Scientific observations of bow waves were first reported by Froude, who called them divergent waves (see Figure 2.1). Subsequently, Lord Kelvin, who knew about Froude's observations, calculated the wave pattern behind an infinitesimal disturbance. This wave pattern consists of sets of nested divergent and transverse waves, see Figure 2.2. After this publication, divergent waves have mostly been linked with the Kelvin wave pattern.

A great deal of research, mostly by Japanese scientists, has been done on bow waves. In their comprehensive article summarizing many years of their research,

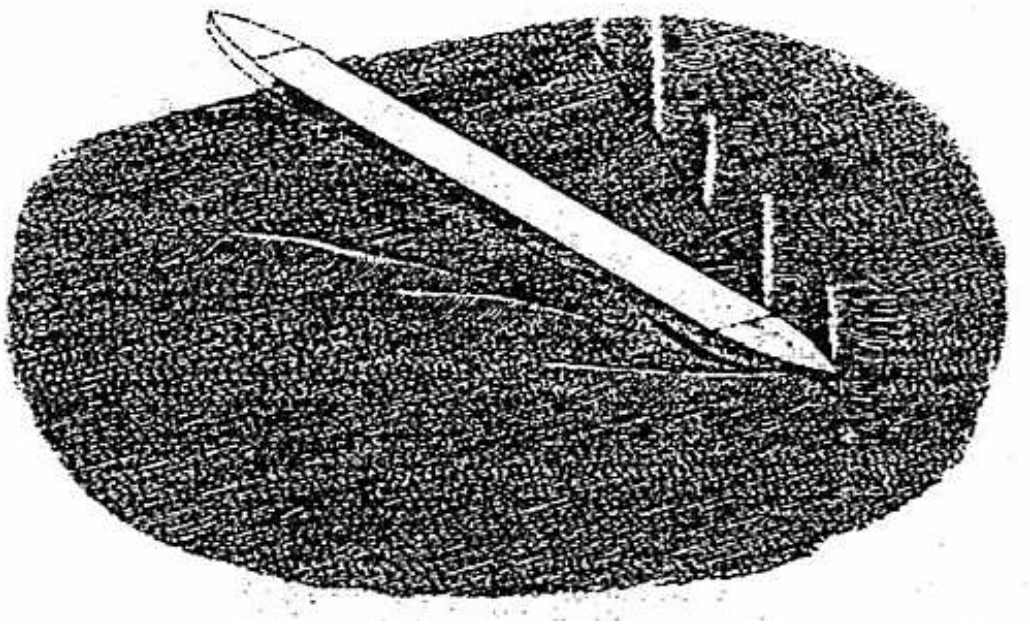

Figure 2.1: Divergent bow waves observed and drawn by Froude

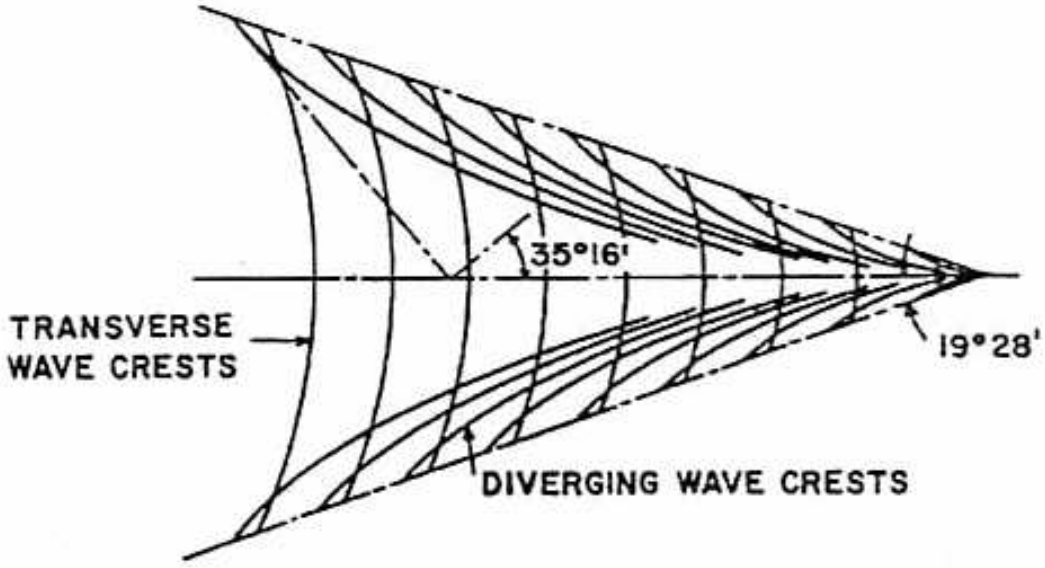

Figure 2.2: Kelvin divergent bow wave pattern.

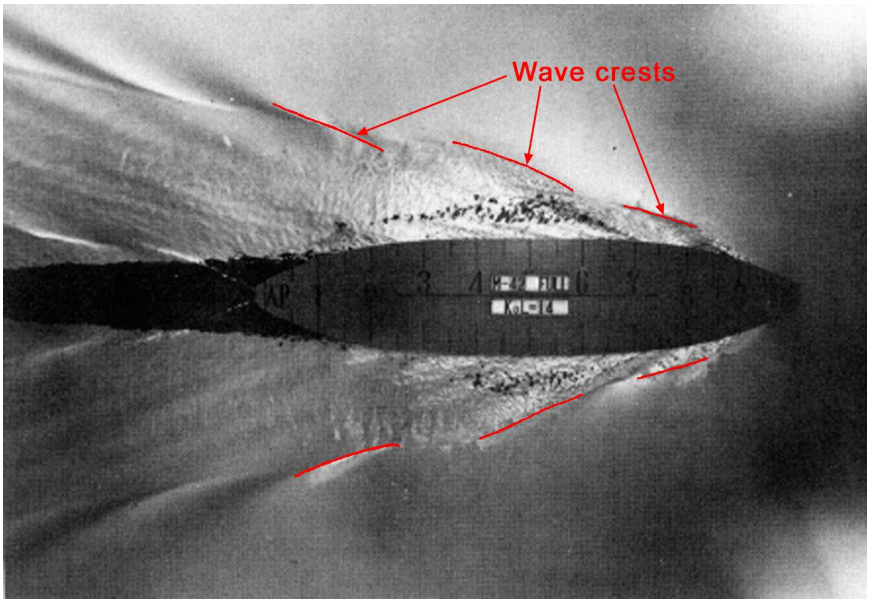

Figure 2.3: Wave patterns around a fine ship model with a draft of 0.105 advancing at $F_n = 0.267$. The aluminum powder film, which covers the free surface, is split on the sides and behind the model.

Miyata & Inui (1984) reported an extensive experimental and numerical study on the free-surface flow structure and wave pattern around several ship models. As part of this work, they spread aluminum powder on the water surface for visualization purposes and observed wave patterns around the models. A typical wave pattern of a fine ship model being towed in their tank is shown in Figure 2.3. The camera view emphasizes the divergent waves which have crests lines with nearly parabolic shape. Behind the first wave crest downstream of the stem, the powder is disrupted (seen as black regions in the photograph) indicating a turbulent free-surface flow. Directly behind the ship model, the aluminum powder is displaced laterally and bare (black) water surface is revealed. This black region seems to be due to boundary layer separation.

Miyata & Inui (1984) observed that the near-surface water velocity field and wave pattern at the bow strongly depend on the Froude number. Pictures of wave patterns around a model with a draft of 0.10 m and three different Froude numbers created with three different forward speeds are shown in Figure 2.4. As can be seen from the photographs, the angle between the wave crest lines and the model centerline decreases with speed.

Miyata & Inui (1984) also found that the near-surface flow becomes turbulent downstream of the first (breaking) wave crest. To study the structure of the flow beneath the free surface, they used multi-holed Pitot tubes to obtain mean velocity fields. Distributions of measured disturbance velocities (equal to the measured velocity minus the free stream velocity) are shown in Figures 2.5 and 2.6. The disturbance velocities behind the wave crest are large, and their direction is almost normal to the wave crest. Changes in velocities happen within a thin layer near the free surface just ahead of the wave crest. This layer is the turbulent breaking region that rides on the forward face of the wave. The velocity component normal to the wave crest decreases significantly across the leading edge of this breaking region, whereas the parallel component remains almost unchanged. From this study, Miyata & Inui noted an apparent analogy between bow waves and oblique shocks in compressible flow; however, there is some controversy over the analogy.

A detailed study of the structure of the flow field within the breaking waves generated by a ship model was done by Dong *et al.* (1997). The ship model (Naval Surface Warfare Center Model 4817) is 3.05 m long and has a draft of 10.4 cm. In these tests, the Reynolds number ($R_e = UL/\nu$ where ν is the kinematic viscosity

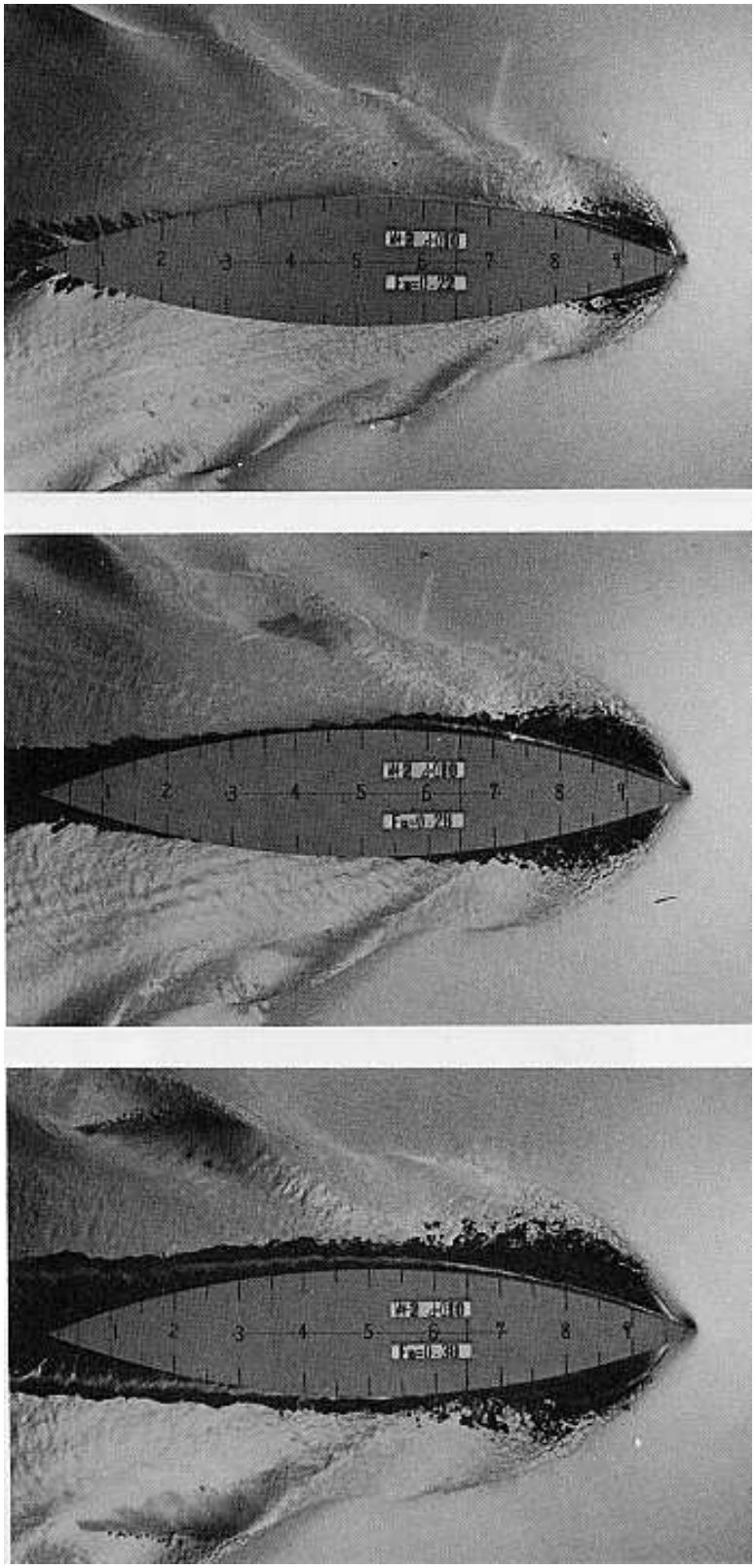

Figure 2.4: Wave patterns around a fine ship model with the draft of 0.10 advancing at three speeds: $F_n = 0.22$, 0.26, and 0.30 from top to bottom, respectively.

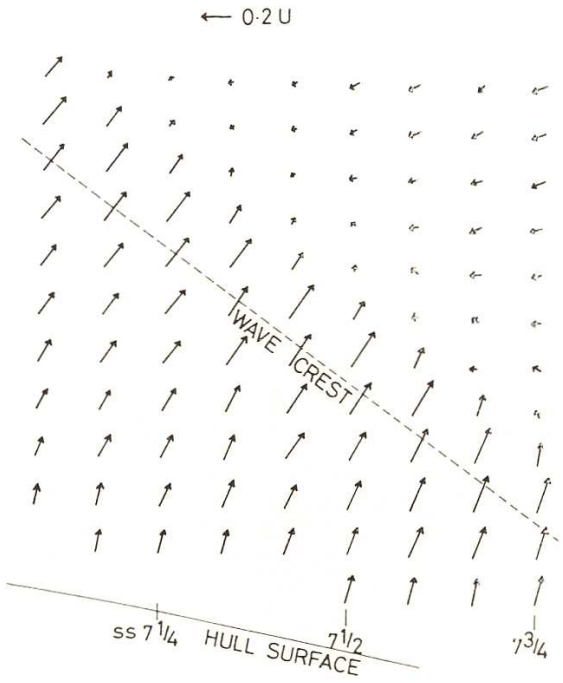

Figure 2.5: Distribution of disturbance velocity vectors on a horizontal plane, 10 mm below the disturbed free surface

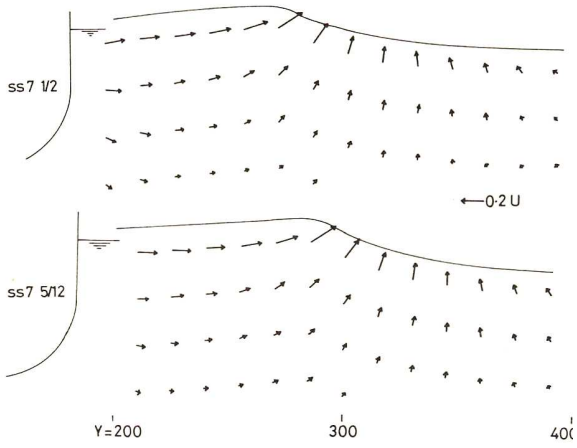

Figure 2.6: Distribution of disturbance velocity vectors on a vertical plane.

of water) ranges from 2.8×10^6 to 7.4×10^6 and results were presented for Froude numbers of 0.28 and 0.45, representing the characteristic structure of weak and strong breaking bow waves, respectively. In these experiments, a particle image velocimetry technique (PIV) was employed to obtain velocity distributions in the near field of a ship model. Dong et al. also distributed fine aluminum powder on the water surface to observe the wave pattern. They focused on the flow and wave structures near the bow of the ship model including the liquid sheet attached to the bow, the flow structure within the bow wave at different distances from the ship model, and the mechanisms of vorticity production.

Dong *et al.* noticed that the bow waves for all conditions had some common characteristics that became more pronounced and easier to identify with increasing Froude number. Photographic examinations of the flow revealed the formation of a thin liquid sheet on the hull upstream of the point where the bow wave separates from the model. This liquid sheet is very thin, unsteady, and fluctuating in elevation and thickness. Their results also show that the formation of a bow wave involves considerable production of vorticity originating from the toe of the breaker. Most of this vorticity remains close to the forward face of the wave and a small part of that extends into the liquid. The vorticiy generated at the wave crest is fed into the flow behind the crest in a series of distinct filaments that create a series of elongated bumps on the free surface.

In agreement with Miyata & Inui's (1984) results, Dong *et al.* show a considerable amount of energy loss in the forward face of the wave near the toe. Also, both studies indicate an abrupt change in the flow direction away from the ship on

the forward face of the wave.

Roth *et al.* (1999) also made an experimental investigation of the flow field around a ship model. Their measurements expanded upon the work by Dong *et al.* by examining the bow wave flow at a higher Reynolds number (1.6×10^7) and a Froude number of 0.30. They used a larger model with length, beam, and draft of 7.01, 0.89, and 0.31 m, respectively.

In the experiments of Roth *et al.* (1999) particle image velocimetry (PIV) was also used to obtain velocity distributions in the near field of the models. The PIV measurement planes were oriented normal to the wave crest line and tilted from the vertical in order to view the light sheet very close to the free surface in the three-dimensional surface wave field. Measurements were performed at successive stations along the crest line. It was found that the breaking wave behaves like an unsteady two-dimensional spilling breaker under surface-tension-dominated conditions. A toe develops and a vortical region appears downstream of the toe. This region spreads downstream close to the free surface as the distance from the hull increases.

The measurements in the experiments of Roth *et al.* (1999) were repeated 92 times at one measurement station and mean properties of the flow field were obtained. A plot of the vorticity of the mean flow from these measurements is given in Figure 2.7. As can be seen from the plot, there is a large main region of clockwise vorticity and smaller region of weak opposite sign vorticity near the free surface above the main vorticity region. Measurements of several terms in the energy equation that contribute to the turbulence production were also measured. According to the measurements, turbulence production is concentrated in the region

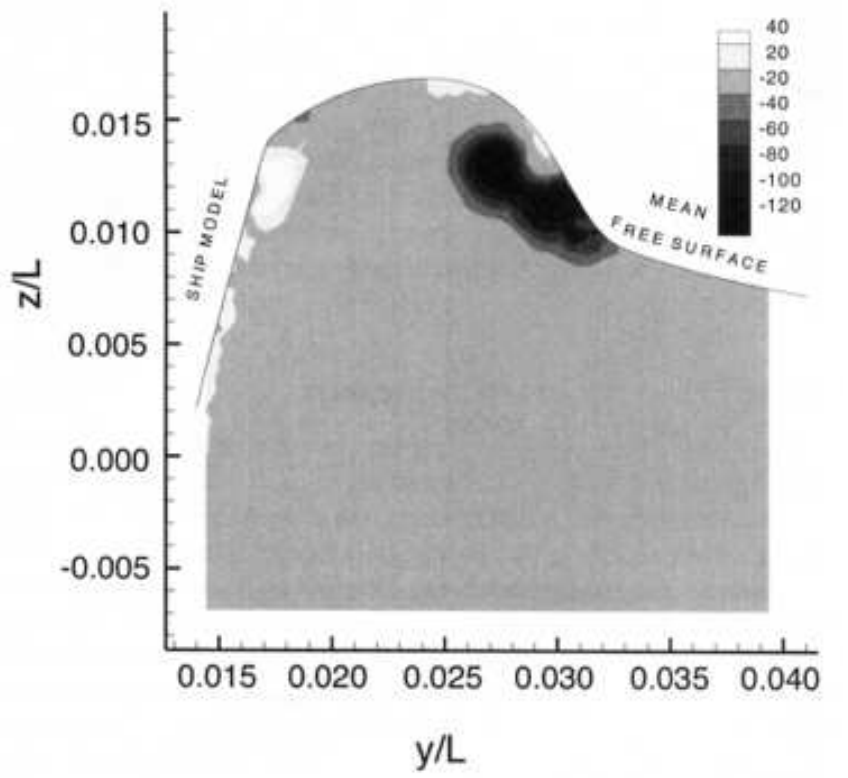

Figure 2.7: Contours of average vorticity in a tilted plane through the breaking bow wave of a ship model. Negative vorticity is directed into the page. $Fr = U/\sqrt{gL} = 0.3$, where $U = 2.51$ m/s is the model speed and $L = 7.01$ m is the model length. From Roth *et al.* (1999).

of highest shear downstream of the toe.

In both of the above described studies, breaking occurs without overturning (plunging) of the free surface or substantial air entrainment where as at full scale massive air entrainment and plunging breakers are found. These differences in the flow at the two scales are due to the effect of surface tension as determined by the Weber number, $W_e = \rho U^2 D/\sigma$, where σ is the surface tension of water, ρ is the density of water, and D is a characteristic dimension, say the model draft. Since σ and ρ have the same values at both model and full scales and since the model speed

must be chosen to keep the Froude number the same at both scales ($U \sqrt{D}$), the Weber number is proportional to D^2 and is much larger at full scale than at model scale. Thus, the kinetic energy of the flow is higher relative to the surface energy at full scale and the free surface deforms more readily resulting in the formation of jets, drops and bubbles.

2.2 Two-dimensional steady breaking waves

A number of investigators have concentrated on steady two-dimensional breaking waves. Quantitative investigation of the flow field in the breaker region of these waves has been helpful in improving our understanding of the dynamics of the flow in ship bow waves.

The mechanics of the steady breaking wave generated by a submerged hydrofoil moving at constant depth and speed was first experimentally studied by Duncan (1981,1983), who made systematic measurements of the breaker. A schematic of the experimental setup is shown in Figure 2.8. Duncan ran his experiments over a range of speeds, depths, and angles of attack. Wavelengths, used in his experiments, range from 0.22 m to 0.6 m. He observed the inception of breaking, and measured the wave crest shape, the lengths and amplitudes of the breaking and following waves, and the mean velocity distribution in the wake. Duncan found that waves with steepness close to 0.102 can exist in either a breaking or a nonbreaking state. When one of these steep waves is in the nonbreaking state, a surface drift current in the direction of the wave travel can induce the breaking state. At this incipient breaking state, the wave-induced drag on the hydrofoil reached approximately the maximum drag associated with the a limiting-amplitude Stokes wave.

Duncan also studied the turbulent wake behind the breaking region and then determined the resistance associated with the breaker. He performed horizontal and vertical momentum balances for the breaking region. From this analysis, he noticed that the weight of the water in the breaking region is supported by friction acting on

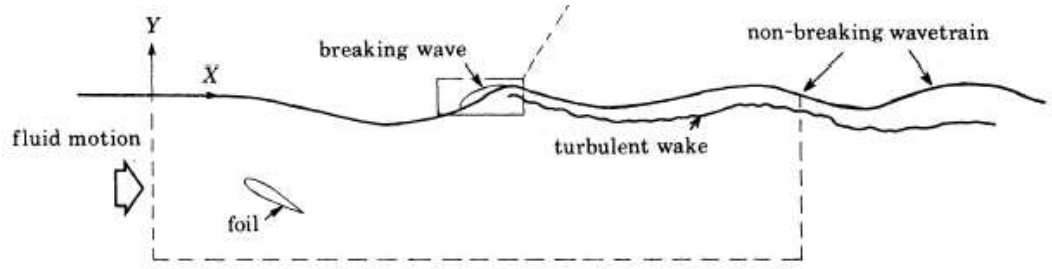

Figure 2.8: Sketch of the experimental setup. From Duncan (1981).

the dividing mean streamline between the turbulent breaking region and the laminar underlying flow. Therefore, he was able to relate the breaker weight to the wake momentum deficit, and thus estimate the density of aerated fluid in the breaker. The results show that upon the inception of breaking, a fully formed breaker appears and a strong repression of the following wave train occurs. According to his experiments, a large part of the pressure drag on the hydrofoil, due to the presence of the free surface, appears as a momentum loss in the turbulent surface wake.

Battjes & Sakai (1981) experimentally investigated the turbulence induced by a breaking wave generated by a submerged hydrofoil (see Figure 2.9) and compared their results to a model developed by Peregrine & Svendsen (1978). Peregrine & Svendsen (1978) observed that the turbulent flow following the breaking resembles a turbulent mixing layer. In their model, at some distance downstream, the upper region of the flow becomes affected by gravity, and for waves in shallow water, the lower region is affected by the bottom. Further downstream, there is a wake or decay region. Battjes & Sakai used laser Doppler velocimety to confirm the validity of the model. The wake trailing the breaker was the main focus of their experiments. They verified the model through the measurement and analysis of the mean flow, the

turbulent intensities, the turbulent shear layer stresses, and their decay with distance downstream. Two waves with wavelengths of 0.28 m and 0.75 m were investigated and all measurements were performed with a mean water depth of 0.58 m and a uniform flow upstream of the hydrofoil.

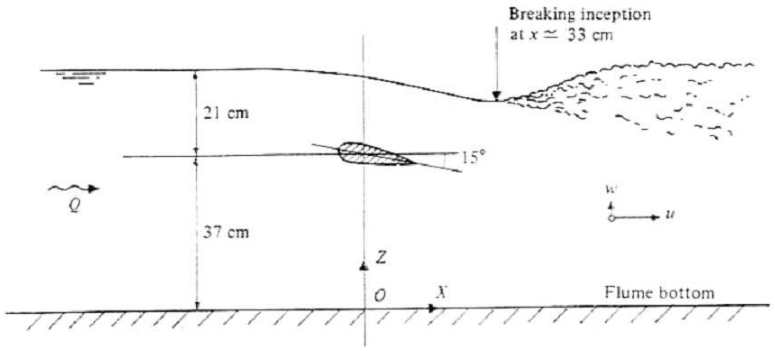

Figure 2.9: Sketch of the flow condition and definition of reference frame. From Battjes & Sakai (1981).

Plots from Battjes & Sakai's measurements of the mean velocity distributions at different distances downstream are shown in Figure 2.10. As can be seen from the plots, there is a strong velocity defect near the free surface. This defect penetrates into deeper regions of the flow and shows a reduction in magnitude with increasing distance downstream. At the most upstream positions, a slight velocity defect can be discerned at a height of about 0.3 m below the free surface. This defect is an indication of the wake generated behind the hydrofoil itself.

Turbulence intensity distributions at different distances from the hydrofoil were measured. Turbulence intensities have their maximum near the toe of the breaking region, from where they decay. The Reynolds stresses indicate significant

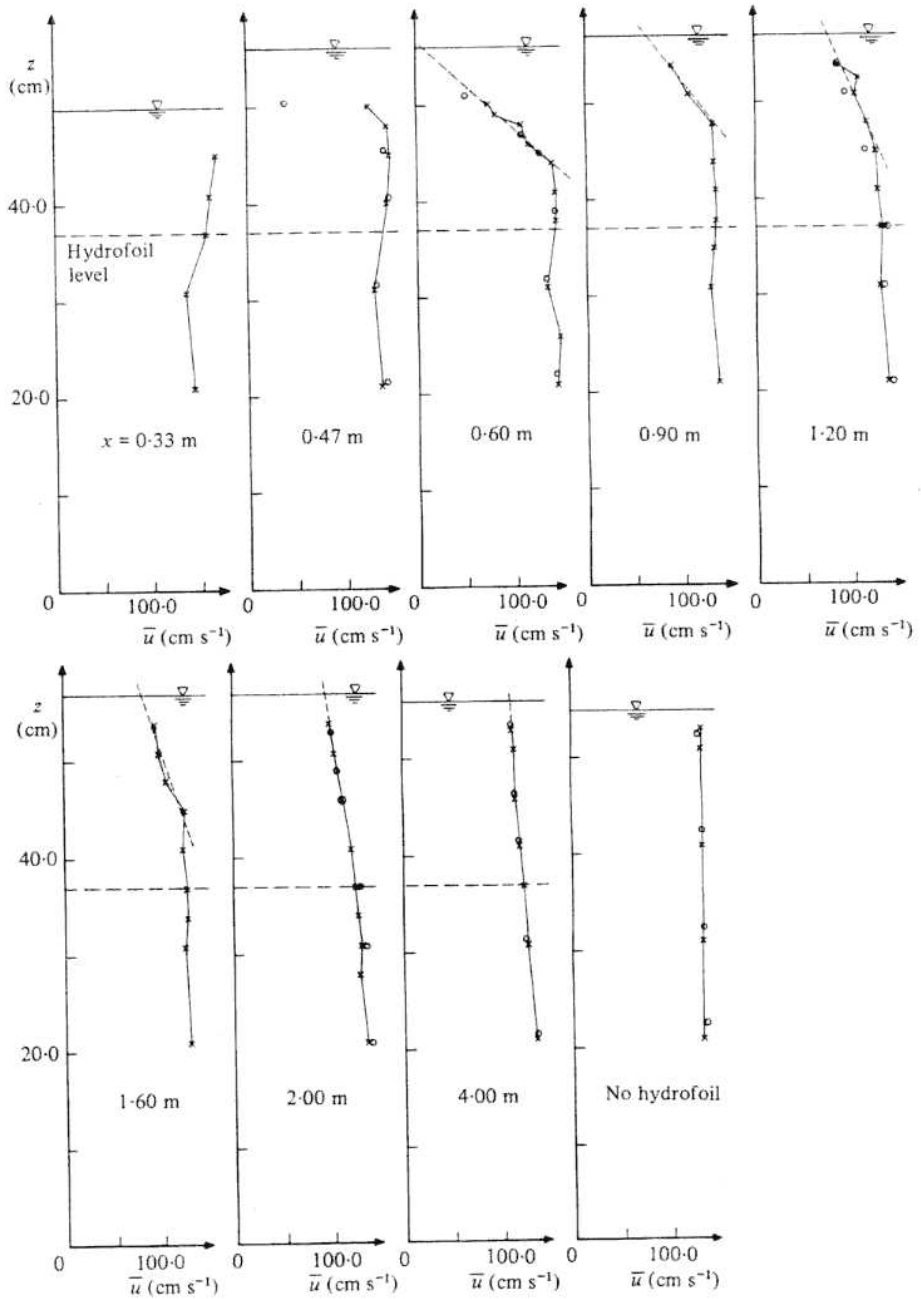

Figure 2.10: Vertical profiles of streamwise mean velocity in sections at distances downstream of the hydrofoil. The dashed lines in the upper part indicate linear extrapolations. The profile in the lower right hand corner is the flow in absence of the hydrofoil. $\times$, full scale experiment; $\circ$, half scale experiment. From Battjes & Sakai (1981).

non zero values only in the upper layer downstream of the toe of the breaker. From the experimental results, it was concluded that downstream of the initiation of breaking, the flow evolves as a free self-preserving turbulent wake. This fact was also confirmed by Duncan (1981) based on photographs of the evolution of dye placed in the wake of the breaker.

Cointe & Tulin (1994) presented a theory of steady breakers based on the experimental results of Duncan (1981,1983). They considered the breaking condition in terms of the total drag on the flow as found downstream as the sum of the momentum deficit in the turbulent wake of the breaker and the momentum in the residual non breaking wave train. It was shown that, for low drags, the system can only exist in a non breaking state. As the drag on the hydrofoil increases, there is a finite range of drags for which three possible flow states exist: (1) a nonbreaking state (2) a strong breaker and a small-amplitude residual wave train and (3) a state with a weak breaker and a large-amplitude residual wave train, which is unstable. The first two states are in good agreement with the results of Duncan (1983). Thus, experimental and theoretical results show that the incipient breaking steepness for steady waves is the lowest steepness for which a finite-size stable breaking region can exist in a steady state on the wave face.

In agreement with the analysis of Duncan (1981 and 1983), Cointe & Tulin modeled the breaking zone as a weak eddy held in place on the wave face by a balance of upslope shear stresses from the underlying flow and the down-slope component of gravity. They also used a mixing layer model, first suggested qualitatively by Peregrine & Svendsen (1978). In accord with Peregrine & Svendsen's model, the

dividing mean streamline between the eddy and the underlying flow undergoes an abrupt increase in flow speed at the toe (the leading edge of the breaking region) and after this point it maintains a constant head and eventually reaches a stagnation point at the wave crest. The pressure due to the weight of the breaking region generates a wave that cancels out part of the following wave train.

Lin & Rockwell (1994) studied the structure of stationary two-dimensional breakers generated by a stationary submerged hydrofoil in a recirculating water channel. They measured the free surface profiles and flow fields using particle image velocimetry (PIV) techniques for breaking wavelengths ranging from 7 cm to 15 cm. It was found that the discontinuous slope of the free surface at the toe of the breaking region and the presence of flow separation under it, serves as a source of vorticity and forms the leading edge of a mixing layer between the breaking region and the underlying flow. The level of vorticity above and below the mixing layer drops rapidly.

Later, Lin & Rockwell (1995)used PIV to study the evolution of a quasi-steady breaker as the flow speed is increased while keeping the hydrofoil depth and angle of attack fixed. Flow states from the onset of a capillary pattern to a fully developed breaking wave were examined. Just above the capillary wave onset, they found a flow state in which the forward face of the crest was covered by a train of large-amplitude capillary waves; for higher flow speeds the wave crest becomes turbulent. A flow field in the toe region for a turbulent case (wavelength of 0.15 m) is shown in Figure 2.11. In the figure, one can see that the toe of the breaking region is located near the minimum surface height in the trough, indicating that

this is a strong breaker for the given flow speed. Surface tension is dominant at this small scale and, as a result, the surface fluctuations are mild. As seen in the figure, the fluctuating flow in the breaking region is pushing its way down into the oncoming flow and causes a very large horizontal gradient in the streamwise flow. An intense instantaneous shear layer extending downstream from the toe can be seen in the figure. The adjacent vectors on opposite sides of the layer have different directions and magnitudes. Therefore, the thickness of the shear layer is much smaller than the vector spacing, which is 0.55 mm. Assuming a steady flow, Lin & Rockwell applied the vorticity flux equation to the measurements near the toe and consequently determined that the main contributor to the vorticity flux through the free surface is convective deceleration upstream of the toe.

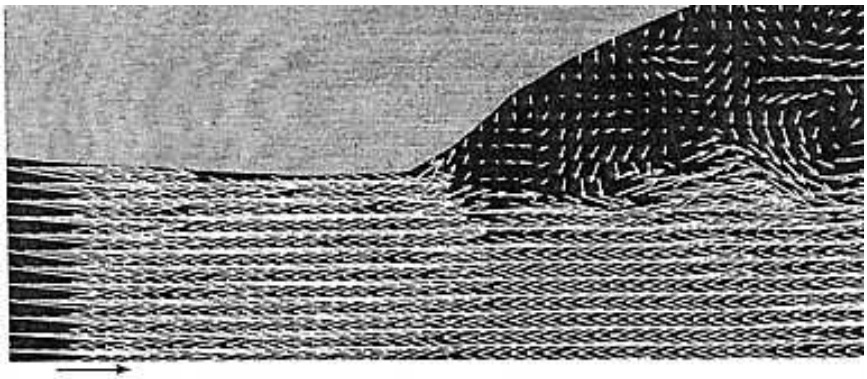

Figure 2.11: Toe region velocity field. The free stream velocity is shown by the black arrow below the image. From Lin & Rockwell (1995).

Dabiri & Gharib (1997) studied the structure of a weak hydraulic jump generated using a honey comb section with a screen, which was placed at the beginning of a test section in a closed-loop water tunnel facility. They used particle image velocimetry (PIV) to study the sources of vorticity flux in the spilling breaker zone of

the jump. In one case (Reynolds and Froude numbers 7370 and 2.04, respectively) they observed that the breaker was preceded by a train of capillary waves with wavelengths of 1 mm and a maximum amplitude-to-wavelength ratio of 0.18. In this flow, there was a thin high-velocity free-surface fluid layer that decelerated just prior to the toe of the breaking region, causing an injection of a large amount of vorticity into the fluid bulk. The vorticity injection due to the free-surface deceleration was seen to dominate over gravity-generated vorticity flux.

2.3 Two-dimensional unsteady breaking waves

2.3.1 Approach to breaking

The earliest theoretical consideration of water wave breaking was given by Stokes (1880) who showed that the there is a maximum amplitude for a steady, uniform, infinitely long, monochromatic wave train. At this limiting amplitude, there is a stagnation point at the crest and the crest profile is a sharp corner which is symmetric about a vertical plane and has an internal angle of 120°. This theory does not describe the development of the flow as the surface overturns, which involves a time dependent flow with asymmetric crest shapes. There are no analytical theories available for this breaking process and researchers have resorted to numerical methods to predict the flow.

A start in this direction was made by Chan & Street (1970), who employed the so-called marker-and-cell technique. In this method, the flow is assumed two dimensional and time dependent. A rectangular grid is employed and the velocity components are computed at fixed points within each cell. The development of the flow is followed in small time-steps, using difference equations to represent the conservation of mass and momentum, assuming the flow is incompressible and inviscid. For waves in water of finite uniform depth, this method achieved some success. The authors demonstrated the steeping of the forward face of the wave almost up to the instant when the free surface becomes vertical. A description of the overturning was not achieved and in spite of the inviscid character of the method some vorticity was generated during the calculation.

All types of finite difference calculations require a grid through out the computational domain with sufficient spatial resolution to capture the local scale of the flow or the radius of curvature of the free surface. Thus, in two-dimensional flows, the number of grid points increases as the inverse square of the smallest flow scale. Consequently, memory storage increases rapidly and eventually the CPU time, which is a criteria of cost, becomes prohibitive. Longuet-Higgins (1960) has showed that for oscillatory waves, diffusion of vorticity into the interior region of the flow is very slow compared to a typical wave period. Therefore, up to the breaking point, it should be a good approximation to neglect viscosity and assume the motion is irrotational.

Longuet-Higgins and Cokelet (1976) developed a boundary-element method to compute the unsteady breaker. A periodic wave train was examained and pressure forcing on the free surface was used to make the waves break. With this method, it was possible to continue the calculation through jet formation, overturning and plunging towards the forward face of the wave. The numerical method, which is described below, has been adopted by many researchers to study a variety of unsteady free surface flow. These incompressible irrotatitional flows are governed by Laplace's equation for the velocity potential, ϕ. Inside a simply connected domain, ϕ is uniquely determined by the values of ϕ or $\partial\phi/\partial n$ on the boundary of the domain (here n is the coordinate normal to the boundary). In the numerical technique, given the position of the free surface and the fluid velocity on the surface at one point in time, the kinematic boundary condition is integrated over a time step to yield the new position of the free surface and Bernoulli's equation is integrated assuming

constant pressure to get the values of ϕ on this surface. With the known values of ϕ, a boundary integral equation is solved to obtain $\partial\phi/\partial n$ on the free surface. At this point, the velocity on the free surface is known and the calculation proceeds to the next time step.

The advantage of the above method is that the independent variables are calculated only at the free surface. Therefore, the number of independent variables in the computation is of the order of the number of grid points only on the surface and for a given storage and machine time, greater accuracy can be obtained. This method works both for free waves and waves with any smooth distribution of pressure at the free surface. In the work of Longuet-Higgins and Cokelet, surface tension was neglected; however, it has been included in subsequent studies with boundary element calculations by a number of researchers.

A geometrical investigation of the jet shape for a variety of breakers was made by New *et al.* (1985). They used a potential flow boundary-element method to examine a set of plunging breakers in shallow and deep water. Periodic waves were induced to break by a sudden reduction in depth in shallow water and pressure forcing in deep water. They scaled the jets with the length of the jet at a point in the profile when the under side of the jet first becomes horizontal. They found that the scaled shape of the jets are very similar, although the size of the jet relative to the length of the wave varies widely. Therefore, they concluded that the spilling breaker might be initiated by a tiny jet at the wave crest.

Dommermuth *et al.* (1988) used boundary element calculations to study breaking waves generated mechanically in a wave tank. They simulated the entire wave

tank and wave maker. The results show excellent agreement with experimental measurements. Similar calculations were done by Grilli *et al.* (1989) and Cointe (1990). Computational limitations confined them to cases where the wave breaks close to the wave maker. To achieve this short breaking distance, a method know as dispersive focusing was used to generate the breakers. In this method, a packet of about ten waves is generated in a manner such that the wave frequency decreases in time. The speed of water waves increases with decreasing wave frequency. Thus, the waves in the back of the packet catch up to the waves in the front and the packet converges as it travels along the tank. Because of this spatial focusing of the wave packet energy, the wave amplitude grows and the waves break.

Wang *et al.* (1994) developed a boundary element method to overcome the limitation that the waves must break close to the wave maker. They divided the length of the wave tank into many sub-domains. Based on their method, it is possible to generate an unstable wavetrain consisting of a central frequency with small-amplitude sidebands and follow the wave train modulation to breaking events occurring further downstream. The method includes the effect of surface tension and the results show that a range of spilling and plunging breakers can be observed. Part of their results were directed at determining the incipient breaking criterion. It was found that if the fluid particle speed in the crest of any wave reaches the linear group velocity of the dominant wave component, then that wave crest evolves to breaking within a time of a quarter of a wave period. The criterion was verified for both deep and shallow-water waves.

Schultz *et al.* (1994) used boundary element method to investigate the breaking

process of periodic wave trains. In some cases, waves were induced to break by modifying the free surface dynamic boundary condition such that it simulates the effect of converging tank walls. They found that the wave evolution leads to plunging jets of different sizes relative to the wavelength. The plunging jet becomes smaller as the input energy rate is decreased.

The surface tension effect becomes crucial when the wavelength is short. Duncan *et al.* (1994,1999) performed an experimental study of spilling breakers that were mechanically generated by the dispersive focusing technique. The wavelengths range from 0.77 to 1.15 m. In their experiments only weak breakers were investigated. A high-speed camera with a framing rate of 500 Hz was mounted on a carriage that moved with the wave to record the breaking events. The water was mixed with a small amount of fluorescent dye and illuminated with a laser light sheet. The intersection of the free surface and the laser light sheet was extracted from each photograph in the movie to obtain the wave crest profile. In their experiments, a bulge-capillary wave system is formed on the forward face of the crest as it steepens even though the gravity wavelengths are fairly long. The profiles for the focused wave are qualitatively similar to the numerical predictions found in Longuet-Higgins (1992,1996,1997) and Tulin (1996). In the latter study, the breaker, generated by the sideband instability method, develops a bulge capillary wave system, but the details are different than in the focused wave, probably due to 3D effects in the experiments. Duncan *et al.* also showed that the crest profiles just before the onset of turbulent flow are independent of the wave frequency. This is similar to the crest flow when gravity and surface tension are dominant. These results are in good

agreement with the numerical simulations reported in Longuet-Higgins (1996).

2.3.2 The turbulent flow

Turbulence generation occurs through very different mechanisms in spilling and plunging breakers. In plunging breakers, turbulence is generated quickly when the jet impacts with the wave face and the cavity thus created collapses. In spilling breakers, a small zone of separated flow is formed on the forward face of the wave crest. Turbulence first appears at the leading edge (toe) of this separated region and quickly spreads horizontally through the top of the wave as the separated flow region falls down the front face of the wave. A strong shear is found between this downslope flow and the underlying upslope flow.

Theoretical analysis of the turbulent flow left after wave breaking is very difficult. Even Reynolds averaging is not easy since any given point in space and time might be in the water at one time and in the air at another. Theoretical models of breakers are rare and perhaps the theory proposed by Longuet-Higgins & Turner (1974) is the only one applicable to unsteady breakers. The spilling zone, in this model, is idealized as a steady plume extending from the crest with a circulating region at the advancing leading edge. The combined system entrains air from above and water from below. Gravity forces the air-water mixture in the plume in the downslope direction while entrainment of water from below produces a Reynolds stress that counteracts the gravitational force. The entrainment of fluid from below is taken to be proportional to the local velocity difference between the plume and

the underlying flow. The theory predicts that fluid particles in the plume and the leading edge of the wave move downslope with a constant acceleration. The thickness of the layer increases linearly with distance from the crest. The theory also predicts that the density of the mixture decreases with increasing slope of the wave face.

Chen *et al.* (1999) used two-dimensional direct numerical simulation of the Navier-Stokes equations to explore plunging breakers with short wavelengths. In their investigation, the surface tension and viscosity values are not consistent with water: the wavelength of the breaker based on the Bond number and the surface tension of water is 27 cm while the wavelength based on the Reynolds number and the viscosity of water is 9.8×10^{-4}. The results indicate that as the wave breaks, a large jet plunges onto the forward face of the wave and traps a cavity of air. As a result of the impact, a splash is generated which, in turn, generates a secondary forward moving jet, entrapping a second packet of air. The wave profiles are qualitatively similar to the experimental results of Bonmarin (1989) and Rapp & Melville (1990), even though the wavelength in the experiments were fairly large. The similarity of these two results indicates that surface tension is overcome by giving a very strong initial impulse to the wave in the numerical calculation. The circulation structure around the entrapped air cavities is qualitatively similar to that observed by Miller (1976), who tracked small bubbles created around the main air cavities in a plunging breaker event to estimate the water motion.

Rapp & Melville (1990) investigated details of the dynamics of turbulent breakers mechanically generated in deep water. They measured several effects of breaking

events such as the loss of excess momentum flux and the production of surface currents for wavelengths ranging from 0.95 to 2.02 m. The results show a loss of momentum flux of 10% for spilling breakers and 25% for plunging breakers.

Duncan *et al.* (1994,1999) studied the details of the crest shape and flow field during the turbulent phase of the flow in gentle spilling breakers, for wavelengths ranging from 0.77 to 1.18 m. They found that the turbulent phase of the breaking process starts when the toe begins to move down the wave face. The toe accelerates to a constant velocity whose vertical component is 0.135 times wave phase speed. This is not in agreement with the constant acceleration predicted by Longuet-Higgins & Turner (1974). This discrepancy might be due to the dominance of surface tension in the experimental studies which was not accounted for in the theoretical model. It may also arise from the fact that, in the experiments, the slope of the wave face changes with time while a constant slope is assumed in the theoretical model. In the experiments, the circulation shows a rapid increase as a vortical region spreads along the surface starting at the toe and extending back to the crest before the measurements cease.

2.4 2D+T ship breaking bow waves

2.4.1 Similarity of 2D+T to 3D ship bow waves: Calculations

The 2D+T approximation was first introduced in aerodynamics by M. Munk for the prediction of loads on slender bodies with low-aspect-ratio wings at small angles of attack. It has been extended to compressible flow and is known to be very useful for bodies of beam/length ratio of 0.1 or smaller. The flow around slender ships at high Froude numbers can also be approximated by the 2D+T method based on the idea that longitudinal gradients of relevant flow quantities are small compared with vertical and transverse gradients (Tulin & Wu 1996).

In the 2D+T ship wave approximation, the flow is two-dimensional and the streamwise distance (x) along the hull is converted to time via $t = x/U$, where U is the equivalent ship speed. Because the method is two-dimensional, only the divergent waves are computed; the transverse waves would travel in the direction out of the plane of motion and are therefore ignored (see 2.1 for the definitions of divergent and transverse waves). This is the principal deficiency of the 2D+T method. However, the transverse waves may be adequately described by other methods.

The 2D+T method exhibits the advantage of high resolution that is sufficient to capture breaking, and even to trace the breaker's overturning jets. At the same time, it neglects certain three dimensional effects which become increasingly important for low aspect ratio ships with blunt bows. For example 2D+T does not allow upstream influence, so it can not predict breaking before the bow.

Tulin & Wu (1996) used the 2D+T technique for calculations of a Wigley hull. They found that the waves produced with this method are quite similar to those calculated with a three-dimensional model. They compared the calculation with the 3D fully nonlinear calculation made at the MARIN model basin in Norway by Hoyte Daven using a computer code named RAPID. Figure 2.12 shows a comparison of the wave pattern computed by the 2D+T code and the three-dimensional code. In the three-dimensional code, the spatial resolution is insufficient to capture breaking events. The same individual divergent waves at the bow and stern can be seen in both calculations, and the origin and extent of these waves match well. A prominent rooster tail behind the stern and the resulting diverging waves are also found in both calculations. There are also differences between the two patterns. For instance, in the 2D+T results the transverse waves are absent and the crests are much sharper.

The 2D+T calculations for the Wigley hull show that the forward wave is always the steepest and most prominent and it seems to originate from the region of the bow where water first rises up the hull. Its crest is very sharp over extensive regions for F_r ($F_r = U/\sqrt{gL}$) up to 0.46, but it does not quite break. The wave becomes higher and moves toward the equivalent of the aft of the real ship with increasing speed. In all cases, the crest lines are much straighter than in the Kelvin pattern, and their angle to the flow decreases with increasing speed as noted by Miyata (1980) for their 3D model tests.

Tulan & Wu also studied the effect of draft and beam on the wave pattern. According to their results, for the largest draft ($L/d = 1$), the crest lines are continuously concave, as in the Kelvin pattern. On the other hand, for the shallowest

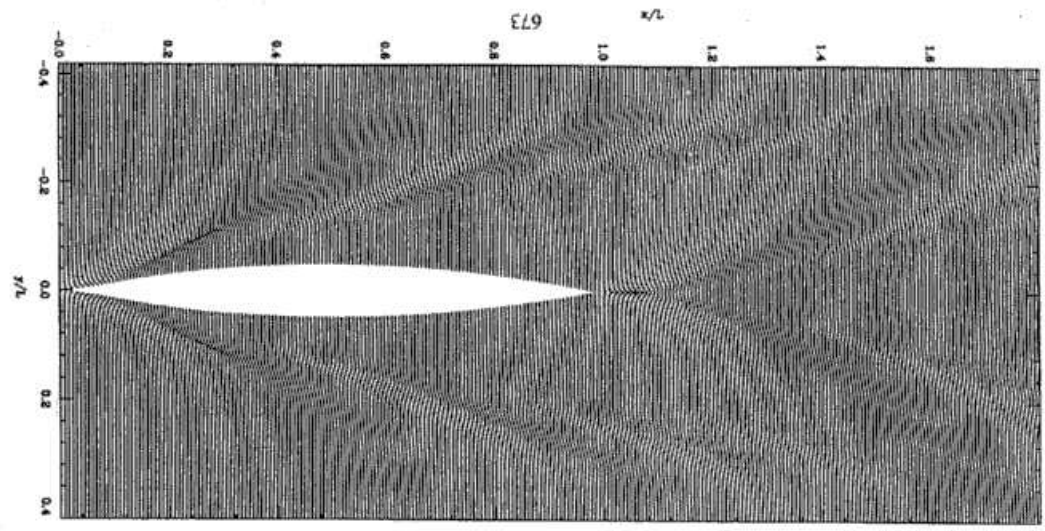

(a)

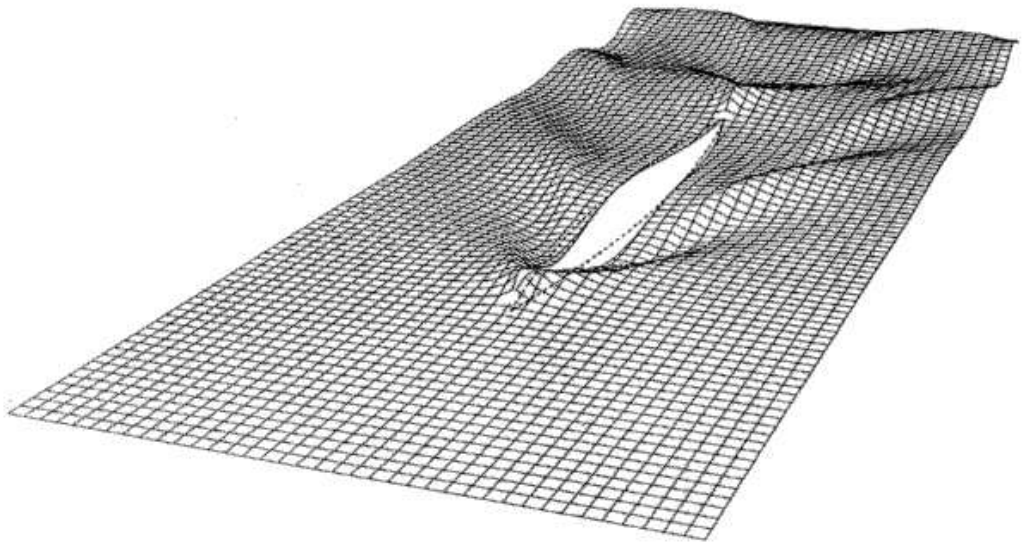

(b)

Figure 2.12: A comparison between (a) 2D+T: $L/B = L/d = 10$; $F_L = 0.30$, and (b) exact nonlinear (RAPID) wave prediction for a wigley hull. The RAPID calculation is by Hoyte Raven of MARIN. From Tulin & Wu (1996).

draft ($L/d = 20$), the wave crests are straight and very steep, i.e., close to breaking. As the beam increases, plunging breaking of the bow waves occurs. Thus, these calculations show that the hull shape is a dominant factor in determining the wave pattern and wave steepness. The 2D+T method seems to be a highly useful tool. Although it fails to produce transverse waves, it offers the high resolution necessary to study very steep and breaking waves.

2.4.2 Similarity of 2D+T to 3D ship bow waves: Experiments

Bow waves generated by the 2D+T technique are similar, in many ways, to the 3D ship bow waves. As mentioned above, Dong *et al.* (1997) made an experimental investigation of free surface flow around a ship model using a PIV technique. The model was 3.05 m long and model speed ranged from 0.914 m/s to 2.44 m/s. They spread fine aluminium powder on the water surface for visualization purposes and photographed the surface flow patterns using a camera that was mounted on the towing carriage. The photographic results show that the main features of the flow around the ship model such as the wave shape, the wave pattern and the location of breaking zones. The location of the breaking zones was steady, but in and downstream of the breaking crests the surface shape has a significant unsteady component. Figure 2.13 shows an extended exposure photograph of the bow wave system around the ship model with a Froude number of 0.334. Since the wavelength of the breaking bow wave is short, it is strongly affected by surface tension.

Duncan *et al.* (1999) studied short wavelength unsteady two-dimensional break-

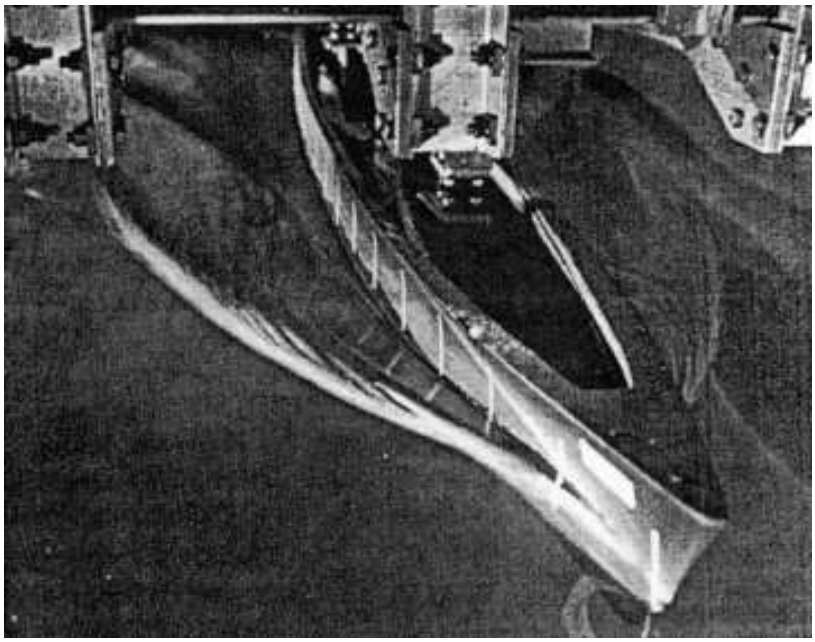

Figure 2.13: Bow wave pattern around a ship model with a length of 3.05 m. From Dong *et al.* (1997)

ers experimentally. The breaker was generated mechanically by a plunging wave maker that was set to produce a packet of ten waves. The phase and frequency distribution of the waves was such that the packet converged via the dispersive focusing method mentioned in the previous subsection to a single weak spilling breaker in the center of the wave tank. The wave profile images were recorded with a high-speed camera which was mounted on a carriage that followed the wave crest as it broke. The data was obtained from 330 successive images of a single wave as it broke. The total time for the 330 images is about equal to the wave profile period, $1/f_0$ where $f_0 = 1.42$ Hz. The crest profile history of this surface-tension-dominated breaking event is shown in Figure 2.14 in a 2D+T format. To obtain the plot equivalent of a 2D+T simulation of this breaker, each successive wave profile was shifted upward and to the left by fixed distances. The wave pattern thus obtained shows the wave

pattern on the starboard side of the ship as it moves vertically down on the figure. In spite of the fact that this wave was not created with any hull displacement in the vicinity of the breaker (as it would have been in a 2D+T simulation), many features in the surface pattern are qualitatively similar to those found in the photograph by Dong *et al.*(1997). In particular, the leading edge of the breaking zones have the same shape and the trajectories and number of the ripples in and downstream of the breaking zones are quite similar in the two cases. While not proving the accuracy of a 2D+T simulation, this comparison does support the idea that the two flows are similar.

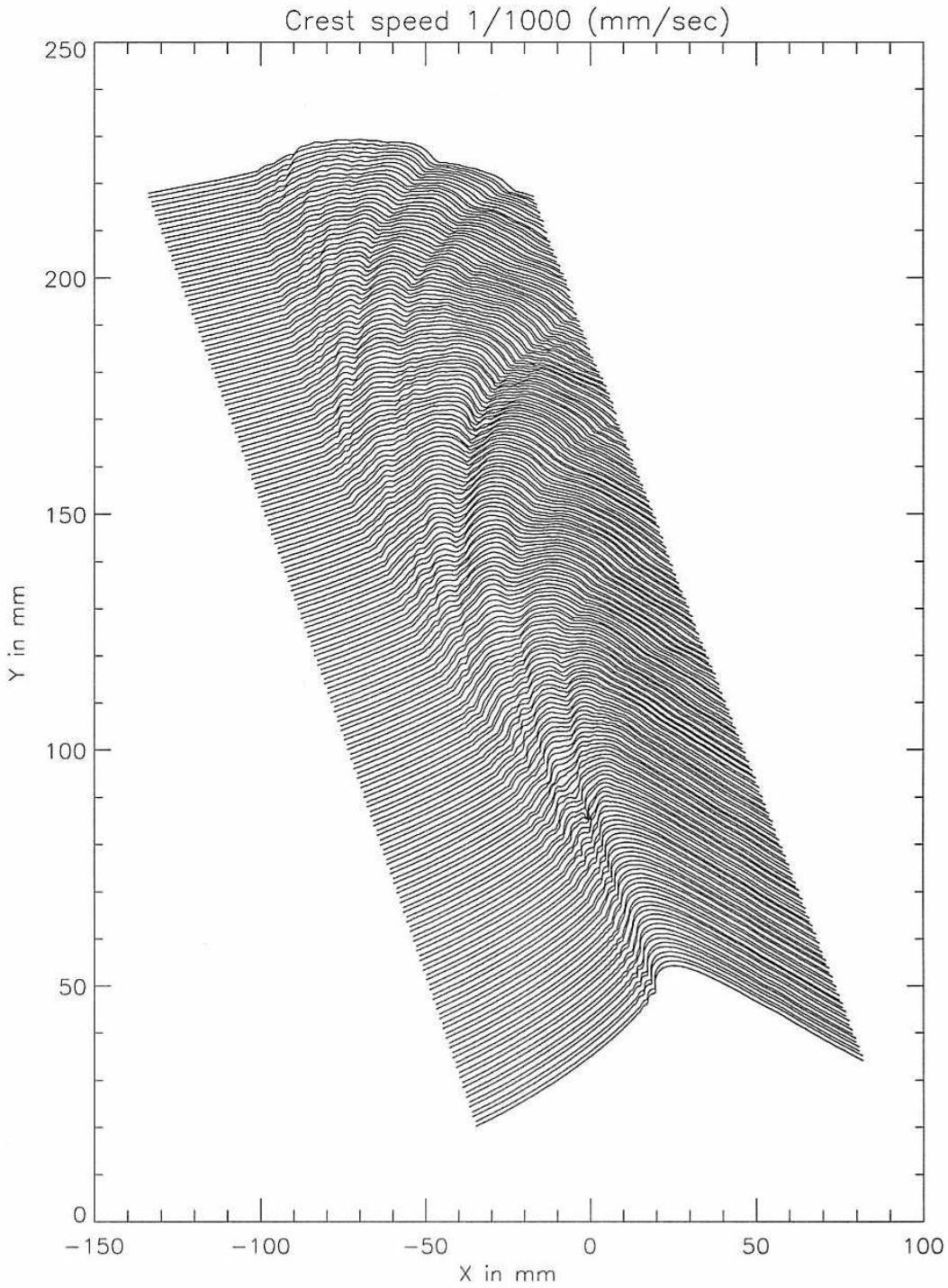

Figure 2.14: 2D+T representation of wave profiles of a two-dimensional spilling breaker generated by dispersive focusing. From Duncan *et al.* (1999)

2.5 Air entrainment and bubble production

Air entrainment by breaking waves has been an active area of research for many years due to its important roles in the enhancement of gas transport between the atmosphere and the ocean, the generation of underwater sound, and the absorption and scattering of ambient sound waves. These phenomena depend on the void fraction and size distribution of the bubbles which in turn depend on breaking characteristics and the local chemical and physical properties of the water, *e.g.*, salinity and temperature.

Air entrainment by bow waves is important in the field of naval hydrodynamics. Air bubbles, particularly the small ones (on the order of micrometers in diameter), are remarkably stable and can persist in the wake for long distances behind the ship. Bubble clouds are detectable by various sonar sensors and thus may make the ship vulnerable to attack. Due to the significance of the bubble presence around the ship, mechanisms of bubble formation need to be fully understood.

There are no reports in the literature of void fraction and bubble size distribution measurements beneath breaking bow waves, perhaps because this type of experiment is extremely difficult and costly. However, some investigators have focused on the basic processes of air bubble entrainment by other types of breaking waves.

A number of investigations have explored the effect of water properties on bubble distributions. There is little difference between the bulk physical properties of fresh water and seawater. The density, viscosity and surface tension in seawa-

ter are only 2.5%, 7%, and 2% higher, respectively, than in freshwater. However, bubbles rising to the surface in seawater tend to produce more foam than in fresh water and this effect accounts for the longer residence time of whitecaps in the ocean compared to those in lakes. Laboratory studies show that an order of magnitude greater number of bubbles are produced by breaking waves in seawater than in fresh water.

An early study in this subject is the one by Monahan & Zietlow (1969) in a set of simple pouring experiments. Their results show relatively more bubbles with radii below 500 μm for sea water than for fresh water. In recent experiments, Monahan (1994) and Wang & Monahan (1995) observed tipping bucket simulations of breaking waves in seawater, brackish water and fresh water. They used a video camera that was capable of measuring bubbles with diameters down to 5 mm. They found that the mean bubble radii in similar pouring events were 2480 μm, 1132 μm, and 320 μm for fresh water, water of salinity of 6%, and water of salinity of 20%, respectively.

Some investigators have tried to determine the reason for the differences in bubble distributions in seawater and freshwater based on the different physical and chemical properties of the two media. One idea is that breakers in seawater and freshwater initially produce the same distribution of bubbles but bubble coalescence is inhibited in seawater, resulting in a smaller average bubble size. Lessard & Zieminski (1971) found a critical concentration of salt, below which coalescence occurs easily and above which coalescence is significantly reduced. They concluded that inhibition of coalescence increases with ionic strength. They suggested that

the primary mechanisms controlling coalescence are enhanced structuring of water as is evident by the increased surface tension and viscosity of salt solutions.

Another idea for the cause of the differences in bubble populations produced in seawater and freshwater was advanced by Slauenwhite & Johnson (1999). They hypothesized that the initial bubble populations (before coalescence) are different in seawater and fresh water. They conducted a series of experiments in which bubbles with a volume of 5 μL were forced through a 43 μm orifice in a test cell. The rapid expansion of the bubble as it passes through the orifice causes it to shatter into smaller bubbles. They reported that the number and size distribution of resulting bubble populations depend on the physical and chemical characteristics of the water sample. Bubbles were found to break into $4-5$ times more small bubbles in seawater than in fresh water. The number of bubbles produced in shattering was found to be a function of salt concentration but was especially sensitive to the types of ions present. In addition, seawater samples with the marine diatom Phaeodactylum tricornutum were found to further double production numbers, and a decrease in temperature from 20°C to 3°C was found to increase bubble production in seawater by nearly 50%. The authors concluded that these effects are separate from coalescence inhibition.

Lamarre & Melville (1991,1992,1994) have made bubble measurements beneath two-dimensional plunging breakers, whitecaps and three-dimensional plunging breakers using an impedance-based void fraction meter. They observed that immediately after the breaking event a bubble cloud is created that can reach a void fraction of as high as $30-40\%$. This cloud initially is comprised of large bub-

bles on the order of milimeters in diameter. This cloud rises and degasses rapidly, leaving behind a plume of microbubbles. Lamarre & Melville (1991) also found that 40% of the total pre-breaking wave energy can be lost in the breaking process, and up to 50% of this energy loss is expended in the air entrainment process.

The air entrainment process and the oscillations of both the individual bubbles and the clouds of bubbles created by breaking waves are a source of underwater sound and also affect the propagation of underwater sound waves. A good summary of much of early work on underwater sound wave propagation was given by Kerman (1988).

Chapter 3

Test facilities and experiments

In this chapter, test facilities, measurement techniques and procedures for the research are described. This description includes the wave tank, the wave maker, the instrument carriage, water treatment methods, and measurement approaches. In all cases, the apparatus, experimental procedure, and data processing techniques are described.

3.1 The wave tank

In order to carry out the 2D+T wave measurements, a wave tank which is 14.80 m long, 1.15 m wide, and 2.20 m deep (water depth 1.83 m) was built. The steel structure of the wave tank was built by personnel from the University of Maryland's Physics Machine Shop. The installation of the wall panels, the floor panels, the 2D+T wave maker and the instrument carriage (see the following two subsections for descriptions of these latter two devices) was then completed by students in the Hydrodynamics Laboratory. A schematic of the wave tank is shown in Figure 3.1. The steel frame of the tank includes a network of steel tubes on the floor and a double row of steel columns with H-shaped cross sections along each of the long side walls. The columns have a 1.2 m spacing along the side walls. Steel beams oriented

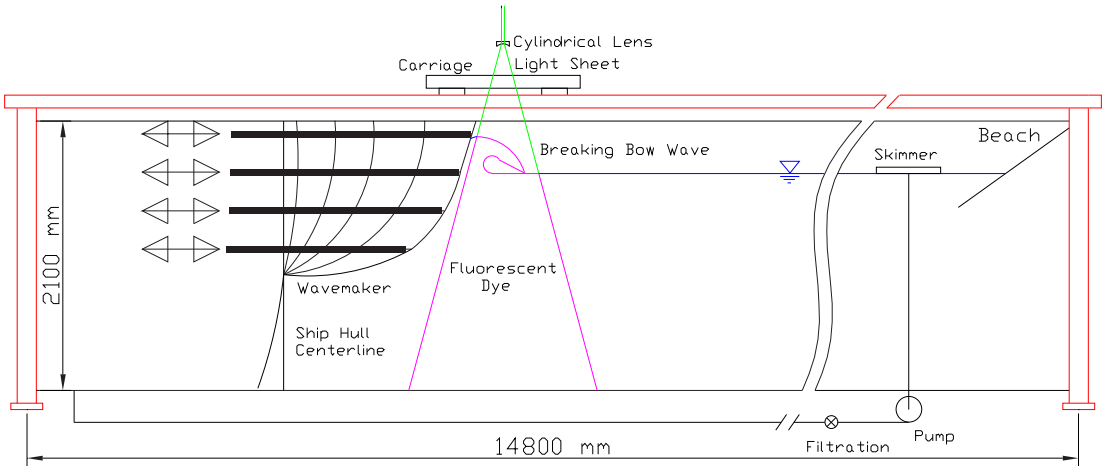

Figure 3.1: A schematic showing the tank and the wave maker.

horizontally are welded to adjacent columns at the top and bottom of the tank and at several heights in between. This steel frame supports the floor and wall panels that hold the water inside the tank. The floor panels and the wall panels at the two ends of the tank are made of 0.635-cm-thick stainless steel plates while the panels on the long side walls of the tank are made of 3.5-cm-thick clear acrylic. The vertical edges of each acrylic plate are supported by the steel columns. During installation of the panels, a special silicone adhesive that adheres to both acrylic and stainless steel was applied to prevent water leaks. Figure 3.2 and 3.3 contain photographs of the wave tank at various stages in the construction.

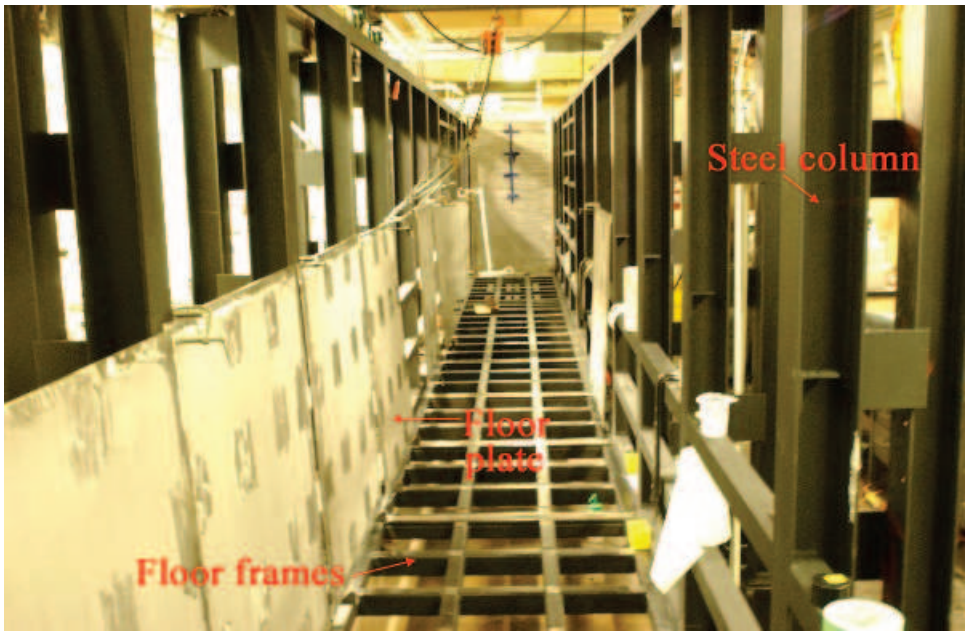

(a)

(b)

Figure 3.2: Heavy structure of the tank (a) before placing the floor plates (b) after placing the floor plates loaded with weights

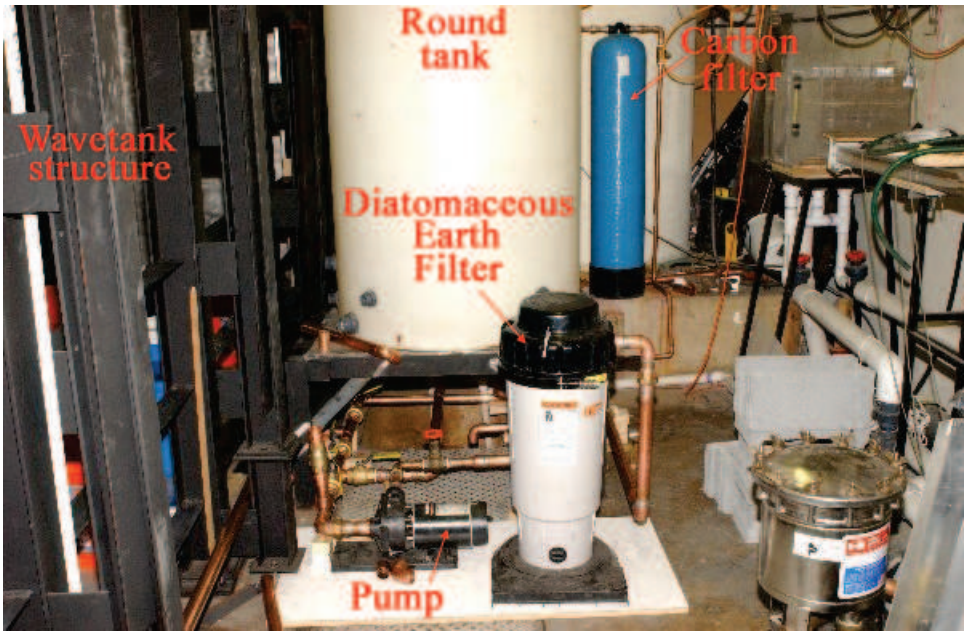

(a)

(b)

Figure 3.3: Different phases of wave tank construction (a) piping system (b) a view of the tank

The 2D+T wave maker occupies about 2.8 m of the tank length at one end. This leaves about 12 m from the retracted position of the wave board (the midplane of the equivalent ship) to the far end of the tank. The travel time for waves generated by the wave maker to reach the far end of the tank and return to the measurement site limits the length of time for which uncontaminated measurements can be made. In the following, this wave reflection time is calculated and compared to the time of the passage of the stern of the equivalent ship model.

The equivalent time of the passage of the stern of the ship model (ΔT_m) is given by

$$\Delta T_m = \frac{L_m}{u_m} = \frac{1}{F_r}\sqrt{\frac{L_m}{g}} \tag{3.1}$$

where g is gravity, L_m is the equivalent 3D ship model length, u_m is the equivalent 3D ship model forward speed, and $F_r = u_m/\sqrt{gL_m}$ is the Froude number. Using the above equation at an equivalent full-scale speed of $u_s = 27$ knots (the fastest equivalent ship speed for the tests described herein, $F_r = 0.3720$), we find $\Delta T_m = 3.936$ s. Also with $u_s = 16.5$ knots(the slowest ship speed for the experiments described herein, $F_r = 0.2273$) we find $\Delta T_m = 6.442$ s. The dominant wave component generated by the 2D+T wave maker is about 2 m long. Using the linear dispersion relationship for deep water gravity waves, the energy (group) velocity of these waves is

$$c = \frac{1}{2}\sqrt{\frac{g}{k}} = \frac{1}{2}\sqrt{\frac{g\lambda}{2\pi}} = 0.88\text{m/s}. \tag{3.2}$$

At this speed, a wave can traverse the 12-m-long distance from the wave maker to the end of the tank and the 12-m-long return in a time of $\Delta T_w = 27$ s. This

is about four times the model time scale, T_m, even at the slowest equivalent ship speed studied herein. Thus, these reflected waves are not expected to affect the measurements before the equivalent time of the passage of the stern.

The highest possible surface wave speed in a tank of water of depth H is $\sqrt{gH}$ or 4.24 m/s for the present case with $H = 1.83$ m. This is both the energy and phase speed of a wave whose length is many times greater than the water depth. At this speed, a wave can traverse the 12-m-long distance from the wave maker to the end of the tank and the 12-m-long return in a time of $\Delta T_w = 5.66$ s. This is a little less than ΔT_m for the slowest equivalent ship speed. However, observations of the waves generated by the wave maker indicate that these long waves are of very small amplitude and are not expected to influence the experimental results. Thus, for the range of Froude numbers used for the experiments described herein, waves reflected from the far end of the tank are not expected to influence the measurements before the equivalent time of passage of the stern of the ship.

3.2 The 2D+T wave generation system

3.2.1 Description of the wave maker

A schematic drawing of the wave maker is shown in Figure 3.4. The wave maker is powered by four servomotors (Figure 3.5), which through gear reducers, drive four vertically oriented shafts. Each shaft drives a toothed pulley, which drives a piston through a rack and pinion system. The pistons, in turn, drive horizontally oriented drive plates that are as wide as the tank (1.14 m) and are guided along

the tank walls by tracks. Position sensors and motor-shaft optical encoders are used in a computer-based feed back control system to achieve the desired motion of each piston. The frame of the device is bolted to the bottom and sidewalls of the tank. Most of the device is submerged and is made of appropriate materials to resist corrosion.

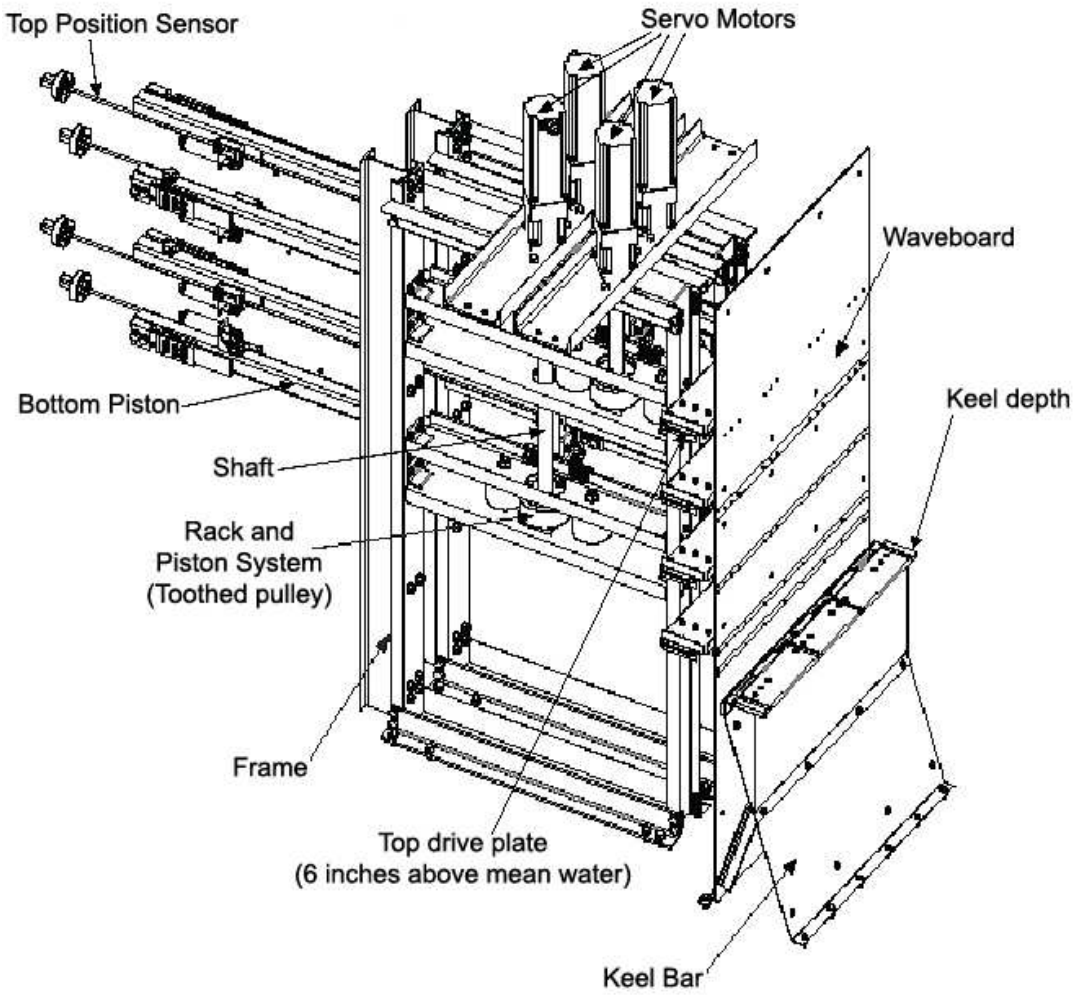

Figure 3.4: A schematic drawing of the wave maker designed and manufactured by MTS system corporation

The main component of the 2D+T wave maker is the flexible wave board which is attached to the four drive plates via hinges. The wave board, which spans

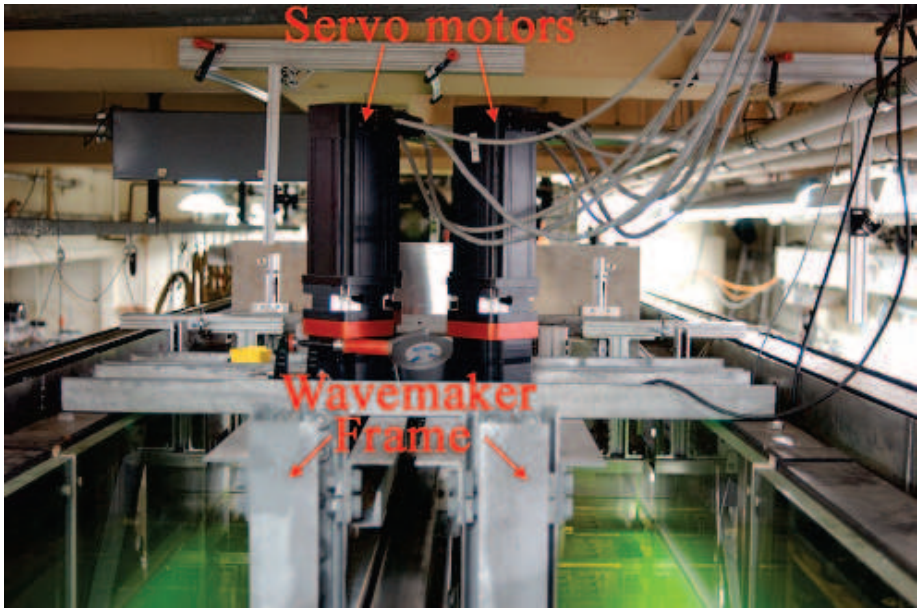

Figure 3.5: A view of the wave maker and the tank, showing the four servomotors used to drive the wave maker

the width of the wave tank, is constructed from interleaved 1/16"-thick stainless steel plates of various lengths, see Figure 3.6 and 3.7. The plates are slotted and riveted together in such a way that does not allow any flow of water through the wave board via a straight path. The stainless steel plates are thin enough to bend elastically under the differential action of the pistons. Each piston is attached to a different layer of stainless steel so that as the pistons move out at different speeds, the changing distance between the hinge points is accommodated by the stainless steel plates sliding relative to each other. Figures 3.8 shows four photographs of the wave maker in operation in the wave tank.

As mentioned before, in this series of experiments, we simulate half of a ship model (say the starboard side) from stem to mid-ship. The keel depths of the 2D+T wave maker and the imaginary 3D ship model that it simulates are 0.91 m. The

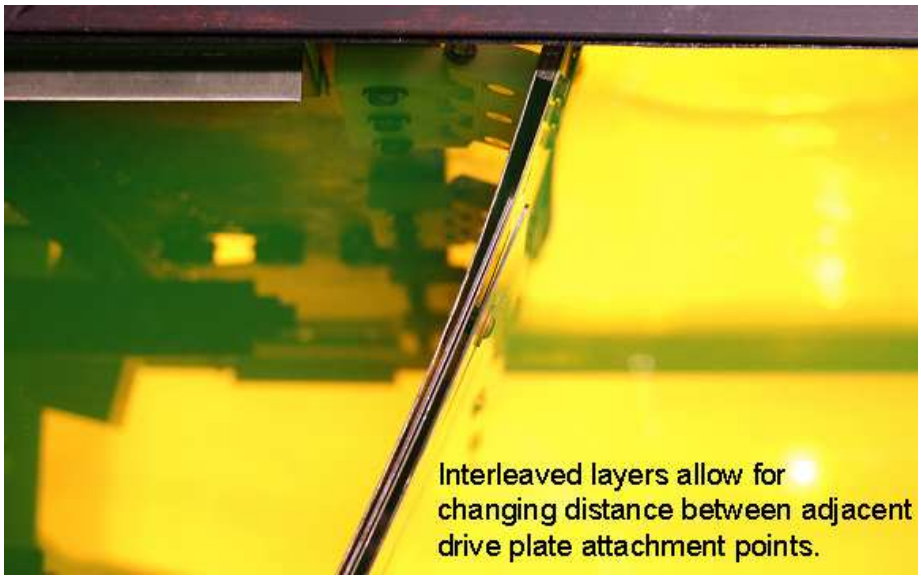

Figure 3.6: A side view of the wave board in operation, showing the interleaved stainless plates

keel depth of the 2D+T wave maker is created by bending the wave board over a fixed horizontal surface, called the keel bar, that spans the width of the tank at 0.91 m above the floor of the tank, see Figure 3.4. The mean water depth is fixed at 0.91 m above the top surface of the keel bar thus creating the desired keel depth for the wave maker. The keel bar is supported by a steel structure which is bolted to the floor of the tank. A delrine block forms the top surface of the keel bar where it comes in contact with the wave board. This block is used to prevent the wave board from being scratched or otherwise damaged as it slides over the keel bar.

As mentioned above, the 2D+T wave maker is used to simulate the 5415 ship model built at the Naval Surface Warfare Center, Carderock. The beam to draft ratio of the 5415 model is 3.11 and the length to draft ratio is 23.11. Thus, with a draft of 0.91 m, the half-beam of the 2D+T model and the equivalent 3D model is

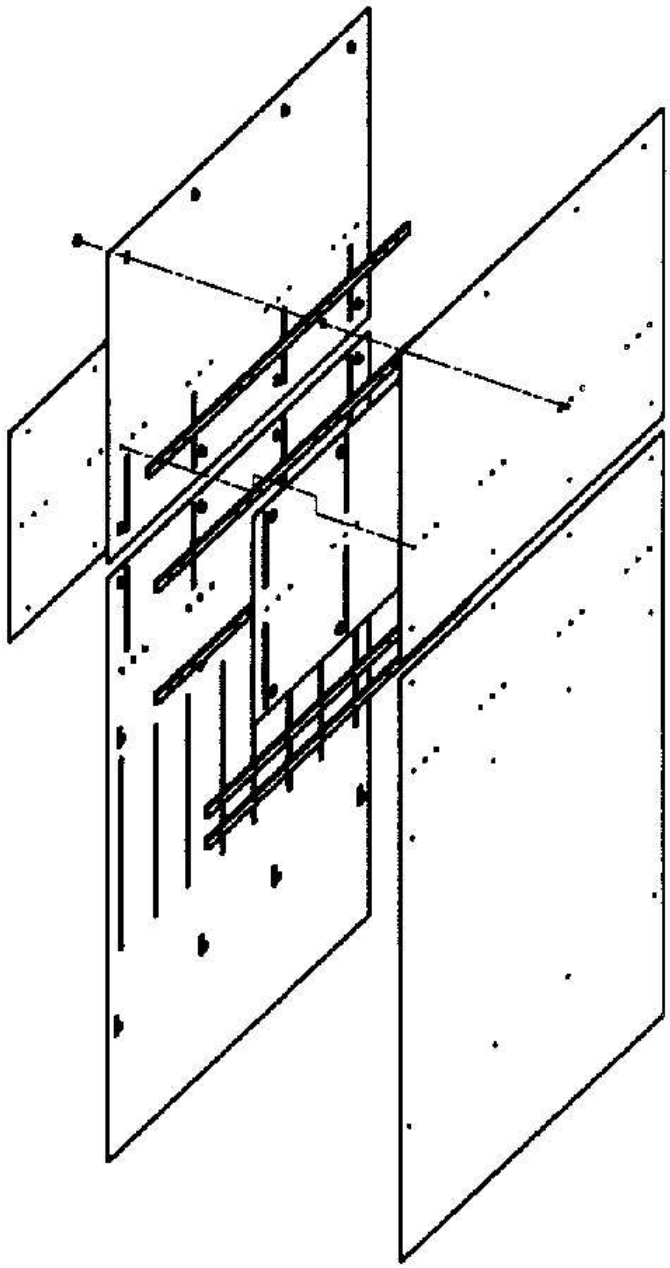

Figure 3.7: An exploded schematic of the wave board

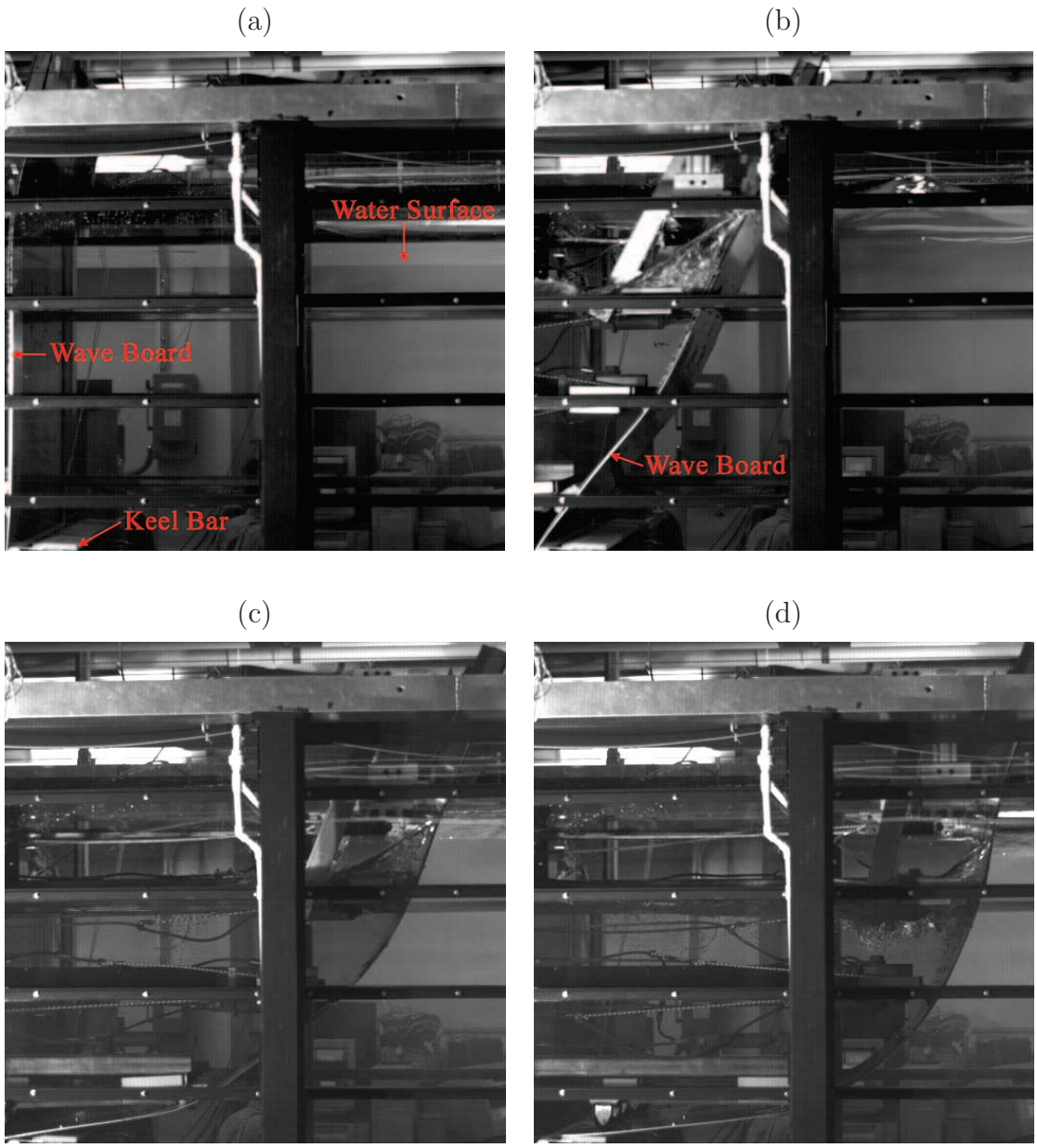

Figure 3.8: The 2D+T wave maker in operation frozen at four different times for equivalent ship speed of 16.5 knots. Time is (a) 0, (b) 0.59, (c) 1.17, (d) 1.76 s.

1.41 m and the equivalent 3D model length is 21.03 m.

3.2.2 Wave maker installation

The 2D+T wave maker was designed and manufactured by MTS Systems Corporation. The wave maker mass is about 2000 kg and it occupies a volume of about $1.2 \times 2.4 \times 3.0$ m^3. The wave maker was assembled at the factory, tested in air and then shipped to the University nearly fully assembled. Figure 3.9 shows a photograph of the wave maker without the wave board as received from MTS.

Figure 3.9: The 2D+T wave maker without the wave board

Before installation, the wave maker was disassembled for two reasons. First, the fully assembled wave maker was heavy and there was no crane system in the Hydrodynamics Laboratory to move it around. Second, it would not be possible to take such a huge device into the tank through one of the narrow openings in

the steel tank structure. During the disassembly each part of the wave maker was labeled. All pieces were then moved into the tank separately and the wave maker was reassembled. The wave maker was bolted to the floor and sides of the wave tank. Joints to the floor were sealed with silicon adhesive to prevent any water leakage from the tank. The last step in the assembly was to attach the wave board to the four drive plates. The wave board was then adjusted to have a uniform gap of approximately 1/8 inch between its edges and the tank walls. Figure 3.10 shows two views of the wave maker after installation. Figure 3.11 also shows the wave maker in operation.

3.2.3 Modifications to the wave maker structure

The first tests of the 2D+T wave maker in water revealed several problems. These problems are explained in the following sections. In each case, the causes of the problem and the solution to overcome the problem are described.

System to control leakage under the keel

As the wave maker is run in water, the mean water height drops behind the wave board (the wave maker side of the board) and rises slightly in front of the wave board. This difference in water height creates a pressure difference between the two sides of the board. During the initial testing of the wave maker it was found that the part of the wave board between the bottom drive channel and the keel bar lifted off the surface of the keel bar as result of this pressure difference. The gap between the

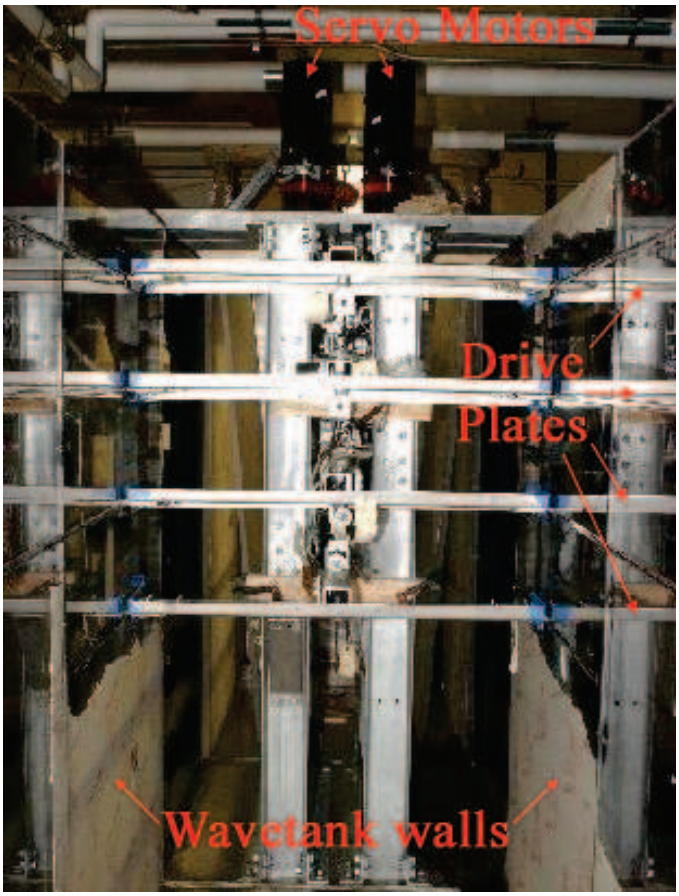

(a)

(b)

Figure 3.10: Two views of the wave maker after installation: (a) A front view before attaching the wave board and (b) a side view

Figure 3.11: The 2D+T wave maker in a stationary fully extended state

keel bar and the wave board allowed water to leak into the wave maker, effectively crossing the vertical midplane of the equivalent ship.

To fix this problem, a passive mechanical system that was attached to the bottom drive plate was used. This system was composed of three stainless steel cantilevered bars (20" × 4" × 3/4") that were attached to the drive plate at one end and to 1.5-inch-diameter wheels in stainless steel frames at the other end. The length of the bars and the height of the wheels were chosen so that wheels pressed the waveboard against the keel bar at the end of the wave maker motion, thus preventing the above described leaking mechanism. A picture of the system is given in Figure 3.12.

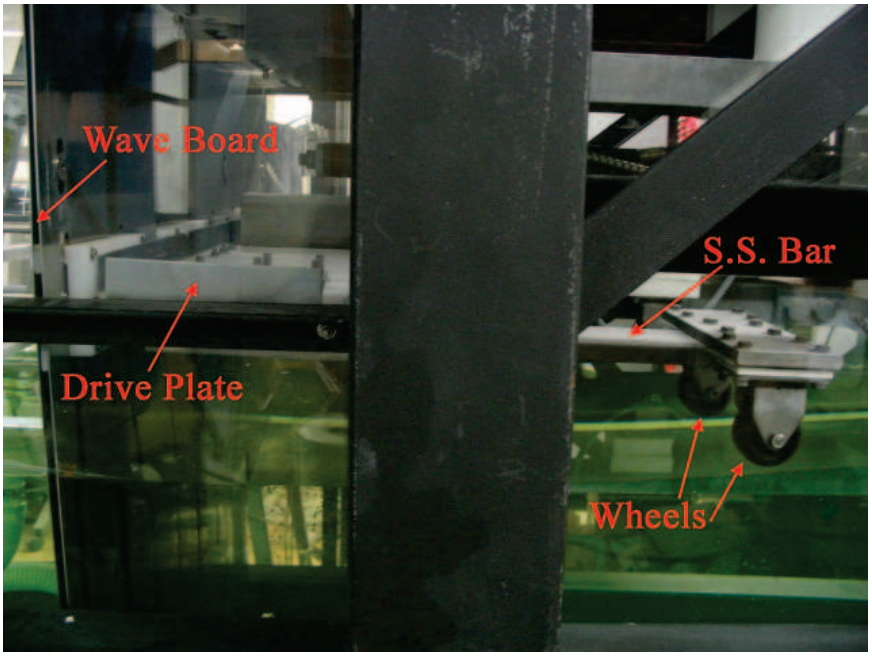

Figure 3.12: A picture of the system for controlling the leakage under the keel

System to control wave board motion above the top channel

When the wave maker was received from MTS Systems, Inc. the top part of the wave board (above the top drive plate) was unconstrained. As a result, it moved back and forth in an uncontrolled manner during the wave maker motion. The top channel of the wave maker is located 6 inches above the undisturbed water free surface. High-speed movies revealed that during the wave maker motion the water surface typically rose above the first channel height onto the free part of the wave board. The oscillatory motion of the top of the wave board created additional water waves that could be seen in movies of the wave generation process. The maximum water height on the wave board rises with the equivalent ship speed so the problem was more severe in the higher speed cases. The above findings indicated that it was necessary to make the part of the wave board above the top drive channel mimic

the ship hull surface as well.

Two possible solutions were proposed to fix the above-described problem. In the first solution, an active control channel would added on above four existing ones while in the second solution, a passive control mechanism would be constructed. The first solution would require a major modification to the wave maker including the addition of some major mechanical parts, a fifth servo motor, and computer software. This solution was deemed too expensive and time consuming. Thus, the second solution was implemented in the form of a passive control channel powered by the top two existing channels of the wave maker. A schematic of the system built for controlling the wave board motion above the top drive channel as well as a photograph of the system are shown in Figure 3.13 and Figure 3.14, respectively. The only drawback of this solution is that the wave board motion is not as accurate as it would have been with the active system. However, analysis showed that the error was small over the parts of the wave board that are submerged at any instant in time. These submerged portions are the only contributors to the wave pattern.

The mechanism chosen to create the passive control channel was a four-bar linkage. A four-bar linkage consists of one fixed (link a) and three movable links (links b,c,and d). Figure 3.15 shows a schematic of a simplified version of the linkage used in the wave maker. In this system, one of the links (link b) drives the system. Knowing the geometry of the system and the driving motion profile, the position of any point on the linkage can be calculated. In this particular example, the position of point (x_2, y_2) can be obtained using the following set of geometric equations:

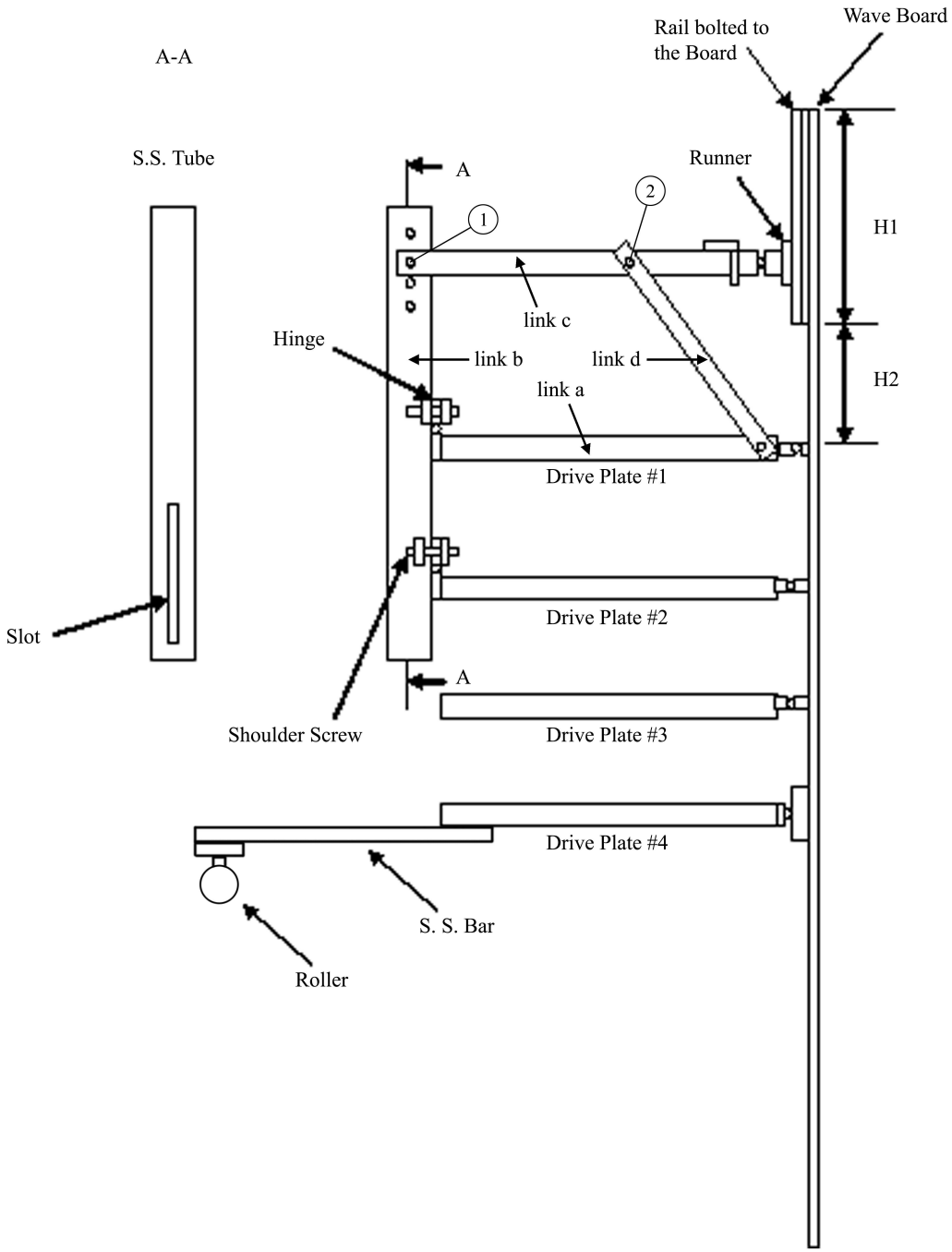

Figure 3.13: A schematic of the system for controlling wave board motion above the top channel and the system for controlling the leakage under the keel

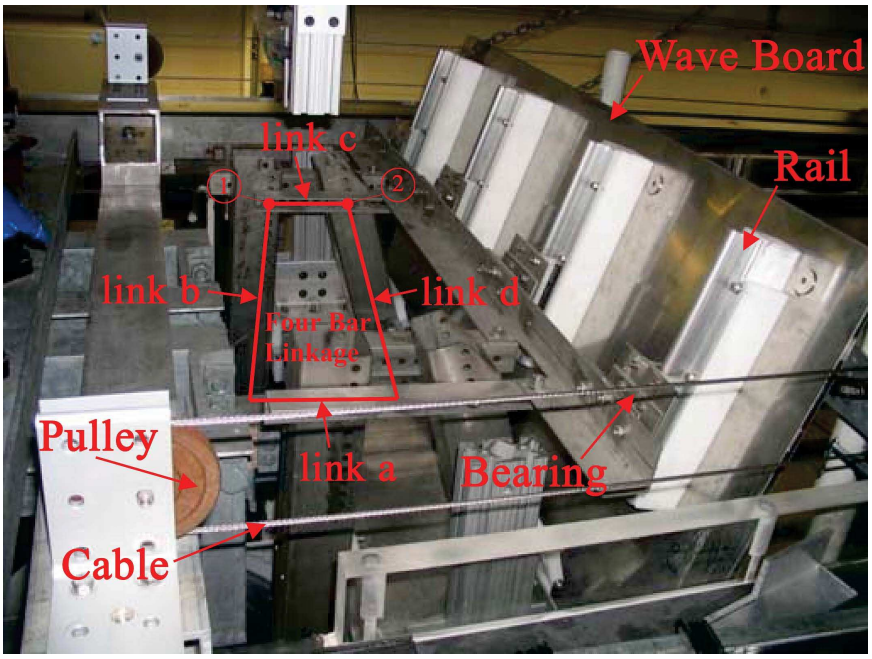

Figure 3.14: The system for controlling wave board motion above the top channel

$$(x_2 - x_1)^2 + (y_2 - y_1)^2 = c^2, \tag{3.3}$$

$$(x_2 - a)^2 + y_2^2 = d^2. \tag{3.4}$$

Eliminating x_2 from the above equations yields a quadratic equation for y_2. Solving for y_2 and substituting in one of the above equations, x_2 can be calculated for any given θ. In this manner, x_2 and y_2 can be calculated for a wide range of θ.

The four-bar linkage system used in the 2D+T wave maker is shown schematically in Figure 3.13 and the bars are labeled with letters corresponding to the generic four-bar link system in Figure 3.15. Two parallel four-bar linkages were used, each one located about 6 inches from one of the long sidewalls of the tank. In the 2D+T wave maker, the top two drive channels were used to drive the four-bar linkages.

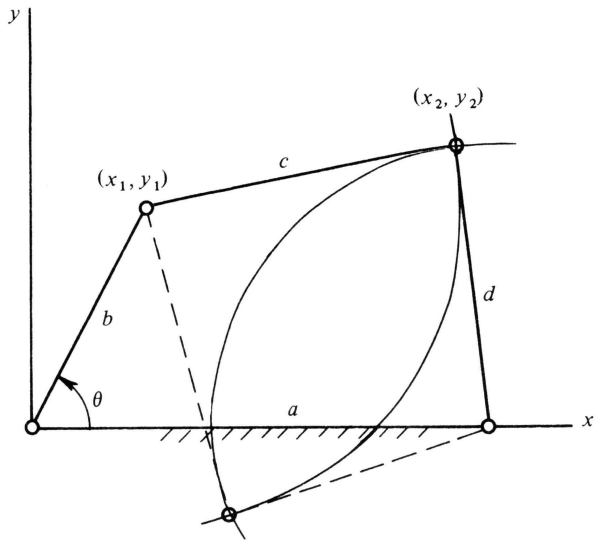

Figure 3.15: A schematic of a simple four-bar linkage

Each linkage uses a square stainless steel tube that was cut to length and bolted to a hinge that was, in turn, bolted to the drive plate of the top channel. The bottom part of the tubes were attached to the second drive plate through sliders. As the wave board extends out, the top channel moves further than the one below and this differential motion creates a moment about the hinge points connecting the top channel to the stainless steel tubes. The tubes are equivalent to link b in Figure 3.15 with the hinge point corresponding to $(x, y) = (0, 0)$ in the figure. This link moves links c and d while the fixed link, a, is the top drive plate. The connecting point of links c and d (point 2) spans a travel of about 6 inches along the wave board as the wave board expands. The two linkages are connected to a single stainless steel angle located at the free end of link c as shown in Figure 3.13. The motion of this angle is then translated to the wave board via four hinges that are attached to runners which in turn move along four tracks that are bolted to the back of the wave board, see Figure 3.13. The four sets of runners and rails were used to get a

more uniform wave board surface and thus a better representation of the ship model hull. The motion of the runners and thus the top of the wave board can be adjusted by moving the pin points marked as 1 and 2 in the schematic in Figure 3.13. A computer code was developed to provide information about the trajectory of the runners. The desired positions of the runners if they were to remain on the 5415 ship model were also extracted from the model coordinates. The difference between the desired and actual positions is the error at each instant in time. Figure 3.16 shows the error as a function of the instantaneous position of the top drive channel of the wave maker. This error plot was created with pins 1 and 2 located in the positions that resulted in the minimum error.

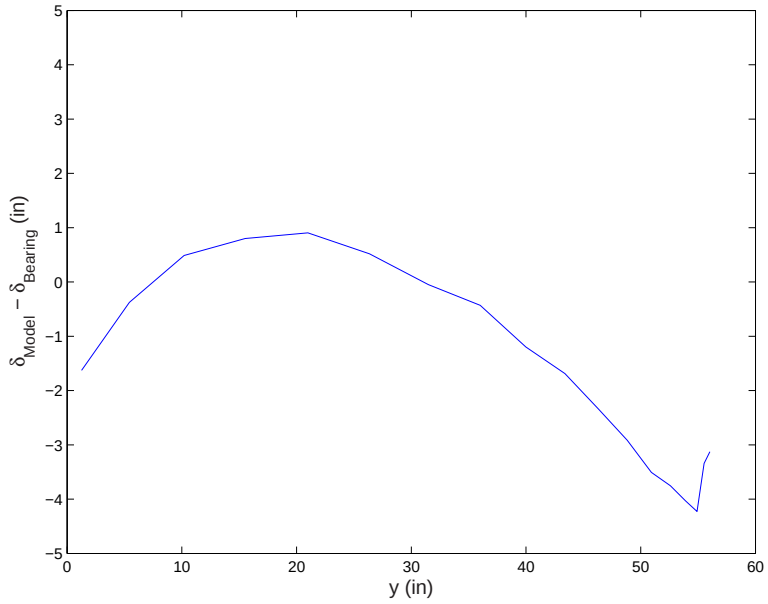

Figure 3.16: Distribution of the difference between the desired and real positions of the wave board. δ_{model}: desired position of the wave board; $\delta_{bearing}$: actual position of the wave board; y: position of the top channel

As seen in Figure 3.16, at the beginning of the motion, the position of the wave

board at the location of the runner is further back than desired (negative error). As time goes on, the error decreases. At some point it becomes zero and then starts to increase. The largest errors are about -4 inches and occur at the end of the wave maker motion. From the movies, of the wave board during runs at various speeds, it was found that the water surface only reached the higher parts of the wave board during the positions with the smallest error in Figure 3.16, between $y = 5$ and 25 inches.

3.2.4 Wave maker control system

Figure 3.17 shows a schematic of the system used to control the wave maker motion. As a mechanical system, the wave maker has its own mechanical properties including mass, damping coefficient, and spring constant. Depending on the effective values of these properties, the system reacts differently to a given external force. As a result, when a move command is given to the motors, the resulting wave maker motion may be different than the input motion. In an effort to minimize these errors, the wave maker was built with a feedback control system. This control system includes both an inner and an outer loop. The inner loop is within the factory-installed control system that comes with the servo-motor and power amplifier system for each drive channel. Feed back is supplied by an optical encoder on the shaft of each motor and the power amplifiers contain computers and software that runs the control algorithms. This control system was not modified during the present investigation. Feedback for the outer control loop is supplied by four linear position

sensors that measure the horizontal position of each of the four drive channels at each instant in time. The output of these sensors is used in a PC-based closed-loop control system with Proportional, Integral, Derivative, and Feedforward (PIDF) components as shown in Figure 3.17.

The basic idea of the PIDF controller is to measure the errors between the desired and measured characteristics of the motion of each channel and to used these errors to compute a correction to the command signal to the motors such that the errors are reduced at subsequent points in time. The four main parameters that control the feedback calculation in the PIDF controller are the proportional gain, the integral coefficient, the differential coefficient and the feed-forward coefficient. The numerical values of these parameters are chosen through a trial and error process. The effect of each parameter on the wave maker motion is explained in the following four subsections.

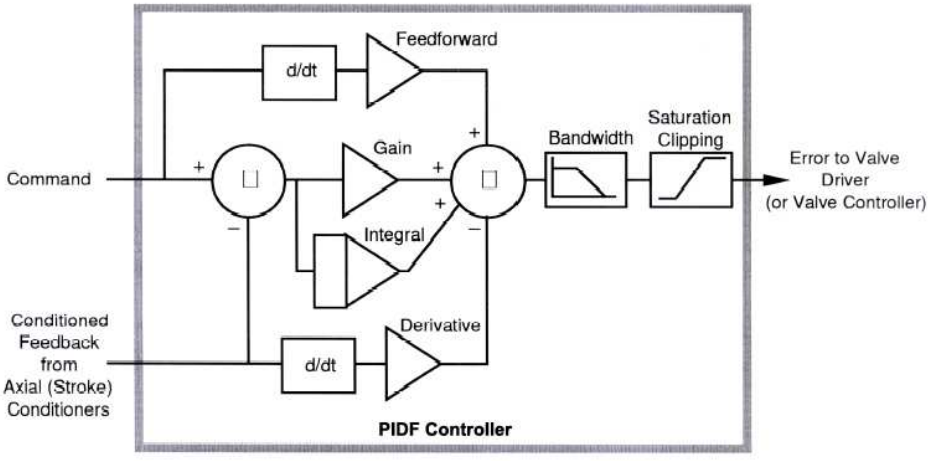

Figure 3.17: The wave maker servo control process

Proportional gain

The proportional gain coefficient multiplies the difference between the desired and actual position of the drive channel. As proportional gain is increased, the error decreases. Figure 3.18 shows the desired and feedback signals with a small proportional gain. In the case shown, the response time and position errors are relatively large. As the proportional gain is increased, the response time decreases.

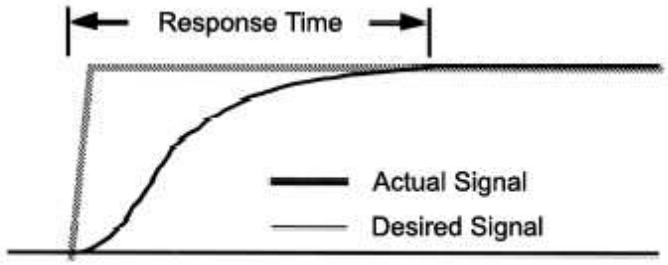

Figure 3.18: The desired and feedback signals with a small proportional gain

However, if the proportional gain is too high, overshooting occurs, and an oscillation (ringing) appears, see Figure 3.19. A high value of proportional gain can result in an unstable system operation. This instability may damage the wave board. Considering the above effects, proportional gain is usually set as high as possible while maintaining stable system operation. If the proportional gain is well chosen, the time the system takes to reach a new position will be as short as possible with the minimum overshoot (or undershoot) and oscillation. Unfortunately, the proportional gain does not reduce the errors to zero in all control applications.

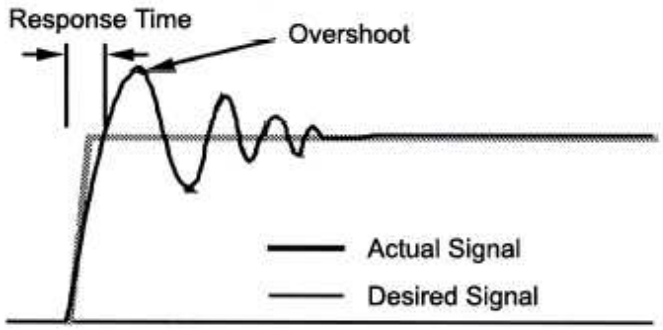

Figure 3.19: The effect of an increase in the proportional gain on the feedback

Derivative coefficient

Once the gain has been set to a value that minimizes the error but avoids overshoot and instability, the derivative coefficient is typically adjusted. The derivative coefficient, as its name implies, is multiplied times the difference in the rate of change (or change in value from the previous sample) of the desired and actual position of the drive channel. The result of this calculation is then added to the drive signal along with the proportional gain correction. In practice, proportional-derivative (PD) controllers work well. The net effect is a slower response time but with far less overshoot and ripple than a proportional controller alone. Figure 3.20 shows the effect of adding derivative to a feedback signal that has already been adjusted for proportional gain.

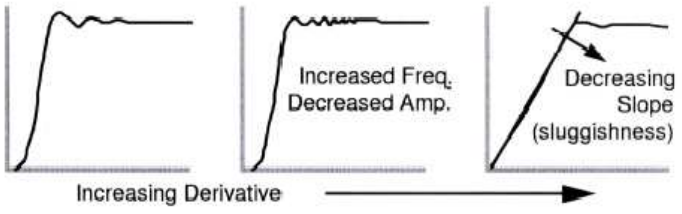

Figure 3.20: The effect of adding derivative to a feedback signal for a previously adjusted proportional gain

Integral coefficient

The problem with a PD control is that it may not settle exactly to the desired position. In fact, depending on the proportional gain, it is possible that a PD controller ultimately settles to an output value that is far from that desired. The problem manifests itself when each individual error remains below the threshold for action by the proportional term. The integral term can help to drive the system toward the exact position. This term represents the sum of all the past errors between the desired and actual positions of the drive channel. Even though the integral gain factor is typically small, a persistent error can eventually cause the sum to grow and the integral term to force a change in the drive signal. Increasing the integral coefficient reduces this error. Figure 3.21 shows the effect of the integral coefficient on the drive signal.

Figure 3.21: The effect of the integral coefficient on the signals

Feedforward coefficient

The feedforward correction to the drive signal is obtained by multiplying the feedforward coefficient times the derivative of the input signal (desired motion); this correction to the drive signal is not based on a measurement of the drive channel position. The main effect of the feedforward correction is the reduction of following

errors, i.e., it essentially changes the phase of the response. It is especially useful, since it does not affect the stability of the control loop. As shown in Figure 3.22, an increase in the feedforward coefficient reduces the following error during a ramp command. Further increase produces a leading error.

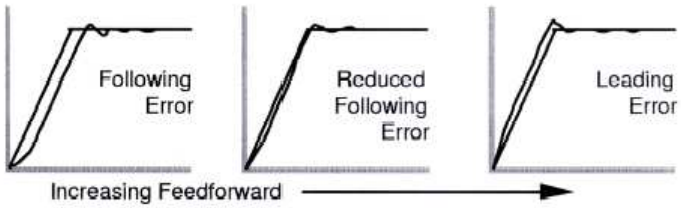

Figure 3.22: The effect of feedforward coefficient addition to the control system

Overall accuracy

After setting up the control parameters for each channel of the 2D+T wave maker, experimental runs were carried out to evaluate the accuracy of the system. The wave maker controlling software can record both the desired and the actual position of each channel. Plotting the actual and desired positions of each wave maker channel shows the error inherent in each motion. In order to have a quantitative value for the error, the average values of the RMS of the errors are calculated for each channel and for each ship equivalent speeds. Figure 3.23 shows a sample plot of actual and desired positions of four channels of the wave maker versus time for the equivalent ship speed of 20 knots. Likewise, RMS values of the errors are plotted in Figure 3.24 for all equivalent ship speeds and all channels. The RMS results show that the errors increase with the equivalent ship speed and that the highest errors occur for the bottom drive channel (4). The RMS errors for the top

two channels, those most important for the wave generation process are on the order of only 0.1 inches.

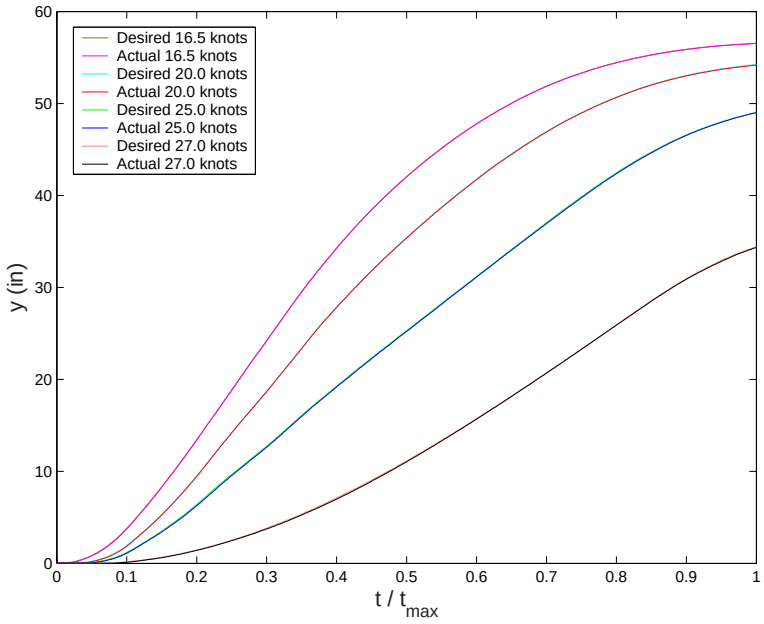

Figure 3.23: Actual and desired positions of the channels of the wave maker versus time for the equivalent ship speed of 20 knots

3.2.5 Modifications to the wave maker motion

Figure 3.25 shows profiles of the intersection of the starboard side of the 3D model hull with horizontal planes located at 6, −6, −18, and −30 inches relative to the mean water level, the same heights as the four drive channels. Note that distances along the y-axis have been scaled up by a factor of five relative to the x-axis to better show the profiles. The top part of the bulb (sonar dome) can be seen in the profile at $z = -30$ inches near the bow. For the 2D+T experiments, the bulb of the ship model is not simulated so this feature is removed from the bottom drive channel motion input profile. All four profiles have a finite slope where they

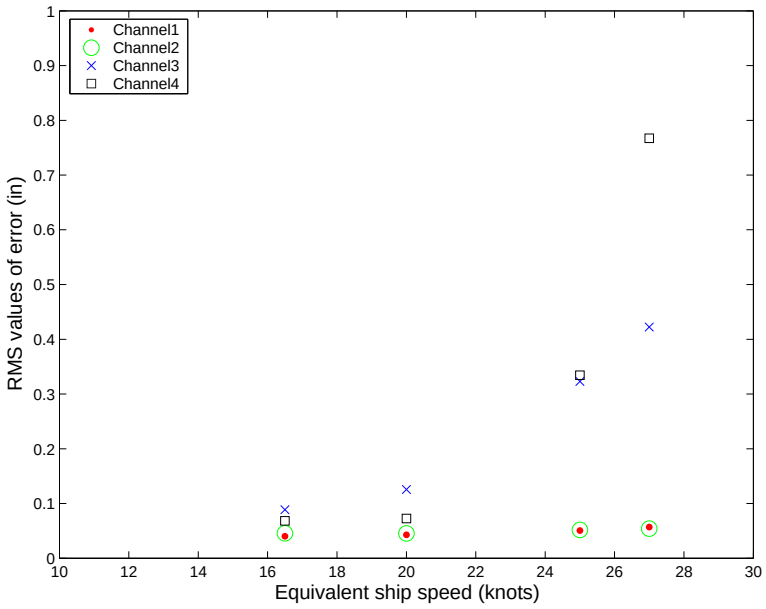

Figure 3.24: RMS values of the error of the wave maker actual motion relative to the desired motion

intersect the $y = 0$ axis, the beginning of each profile. For the 2D+T wave maker, this finite initial slope implies an instantaneous jump in speed from zero to a finite value. It is, of course, impossible to supply sufficient force for a mechanical device to undergo an instantaneous jump in speed so it was necessary to modify the input motion for the four drive channels.

In order to solve this problem, the wave maker motion profiles were modified by extending the stem of the ship forward slightly and reducing the initial profile slopes. This modification increased the length of the ship model by a factor of 190/180. The shape of the added initial part of the profile was chosen as a second order polynomial with zero initial slope and the same value and slope as the ship profile at the intersection of the two curves. Figure 3.26 shows the modified profile of the ship model as well as the real 5415 ship model; closeups of the bow region are

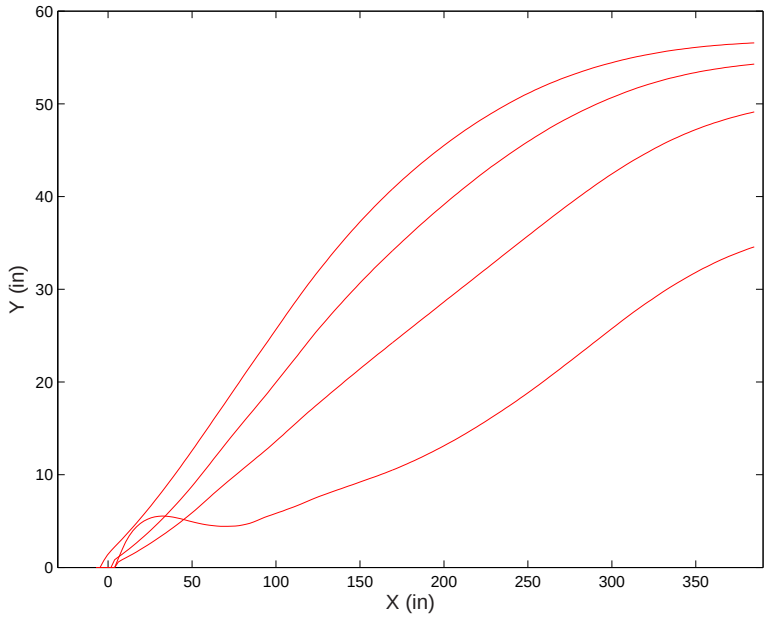

Figure 3.25: Top view of the 5415 ship model hull cut at four levels: 6, −6, −18, and −30 inches from the ship water line.

shown in Figure 3.27. The process of smoothing removed all mechanical problems associated with the initial wave maker motion by reducing the abrupt change in the slope of the input profile.

3.2.6 Wave board shape error analysis

After setting up the control parameters, profiles of the wave board at various times during an experiment were measured and compared to the corresponding 5415 model profiles. To obtain these measurements, a high-speed camera was set to view the wave board from the side, through the clear plastic wall of the tank. Then, the wave maker was made to run. The camera was stationary and temporally synchronized to the wave maker top drive channel. Several images of the wave board were taken from each movie for analysis. Each selected image was displayed

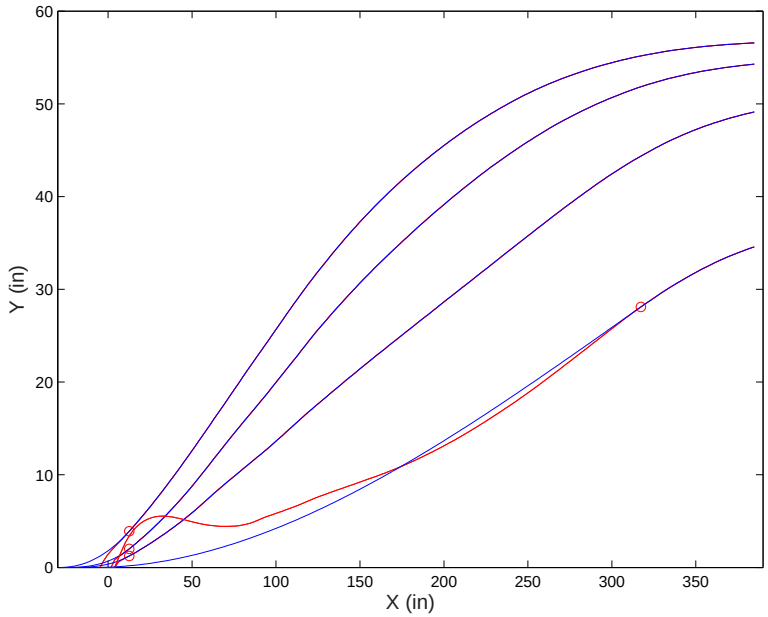

Figure 3.26: Modified profiles of the ship model as well as the real 5415 ship model. Red: actual profiles; Blue: modified profiles to be simulated by 2D+T wave maker. ○: cut-off points.

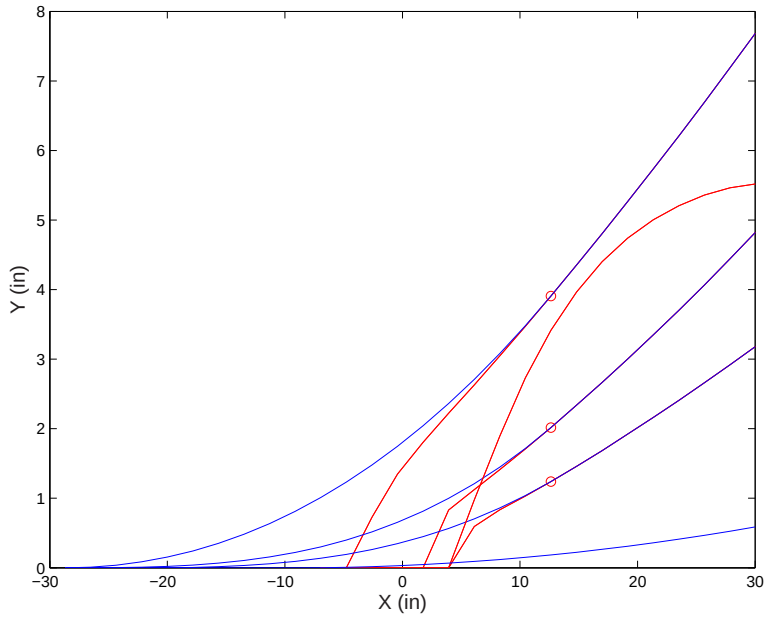

Figure 3.27: A close-up of the profiles to show the slope of the profiles at the very beginning section. ○: intersections of the polynomial representing the modified bow and the actual ship profiles.

on a computer screen and the profile was extracted manually by clicking with the mouse on points on the edge of the wave board. Spatial calibration of the images was accomplished by photographing a large grid with one-inch spacing that was placed on the wall of the tank before the runs with the wave maker. Figure 3.28 shows a picture of the grid used for calibration of the camera. For details on camera calibration the reader is referred to § 3.6.2

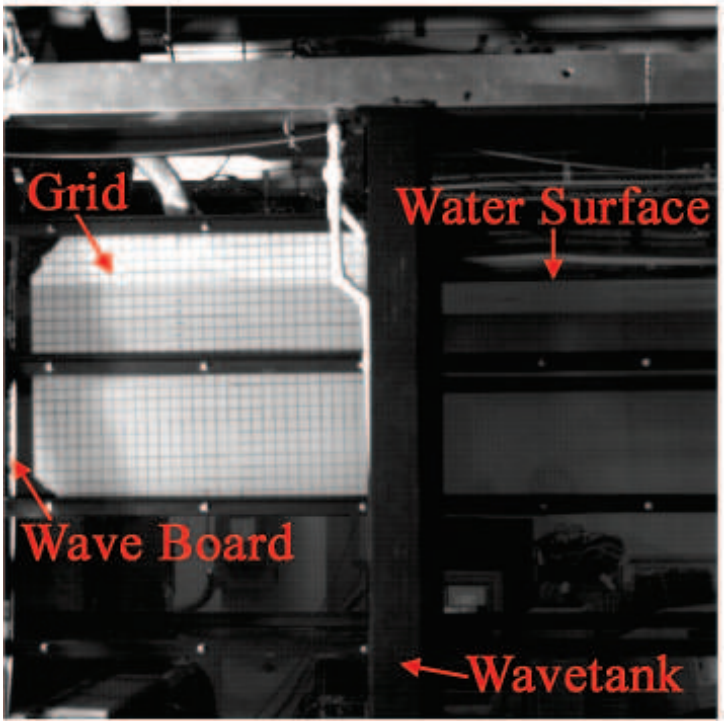

Figure 3.28: An image of the grid

Finally, the wave board profiles and the corresponding profiles of the ship model hull (model 5415) were plotted for comparison. Figures 3.29, 3.30, 3.31, and 3.32 show wave board profiles at different times at equivalent ship speeds of 16.5, 20, 25, and 27 knots.

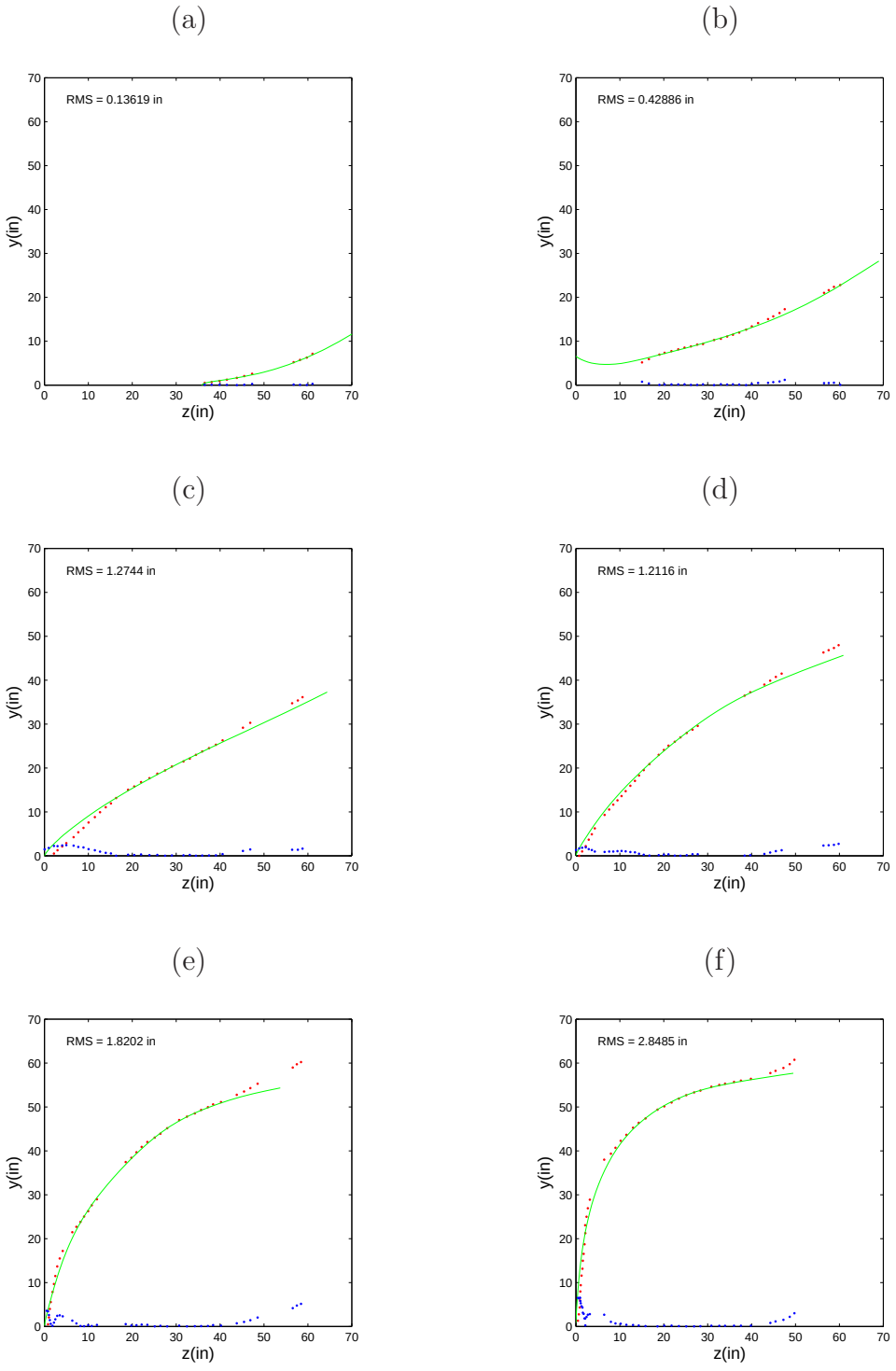

Figure 3.29: Actual and desired profiles of the wave board along with the error distribution for ship speed of 16.5 knots. Red points: measured profiles of the 2D+T wave board at selected times; Solid green lines: profiles of the 5415 model hull; Blue points: errors. Time is (a) 0.278 s, (b) 0.728 s, (c) 1.124 s, (d) 1.541 s, (e) 2.355 s, (f) 3.393 s.

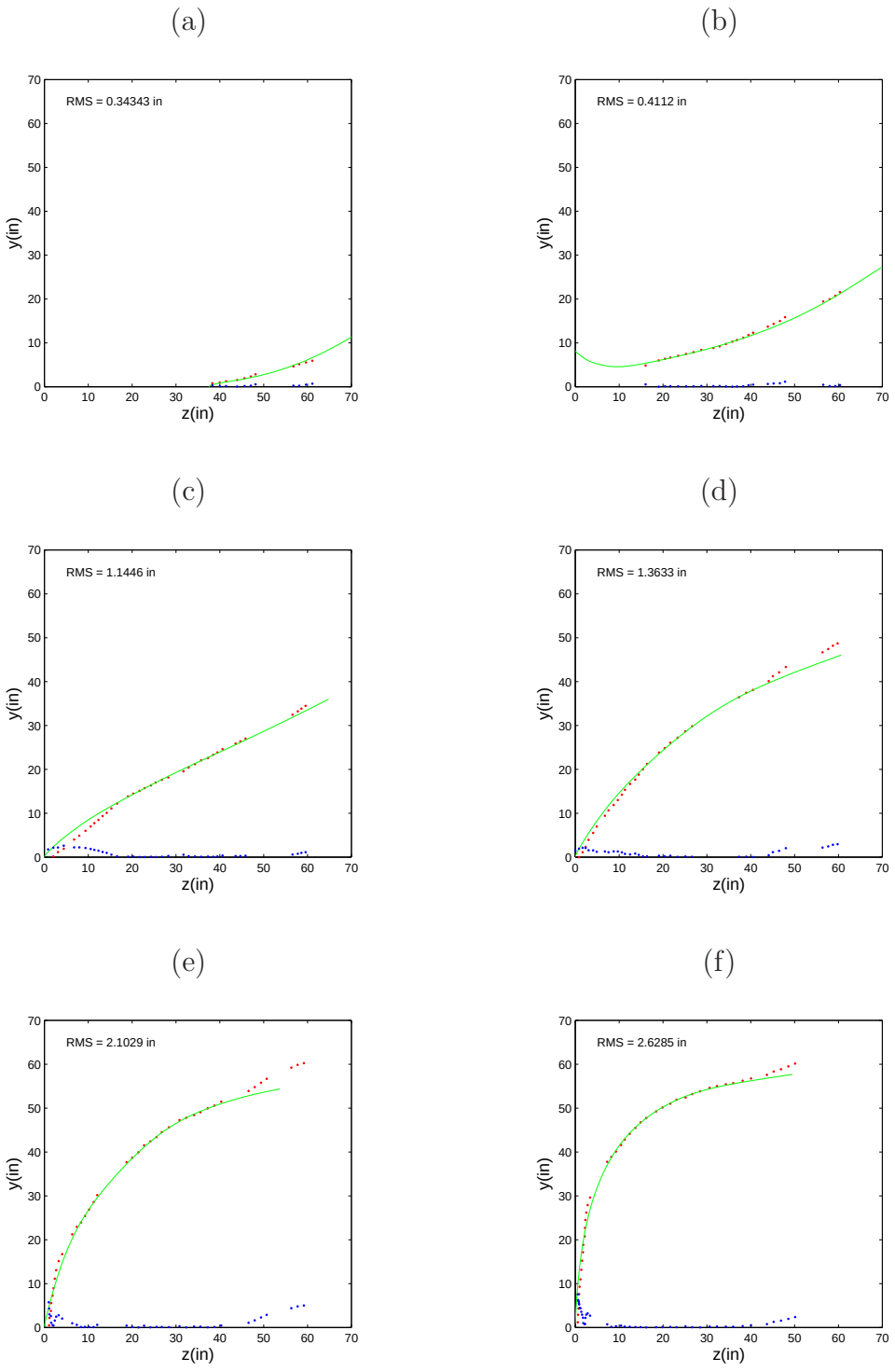

Figure 3.30: Actual and desired profiles of the wave board along with the error distribution for ship speed of 20 knots. Red points: measured profiles of the 2D+T wave board at selected times; Solid green lines: profiles of the 5415 model hull; Blue points: errors. Time is (a) 0.224 s, (b) 0.562 s, (c) 0.884 s, (d) 1.294 s, (e) 1.949 s, (f) 2.800 s.

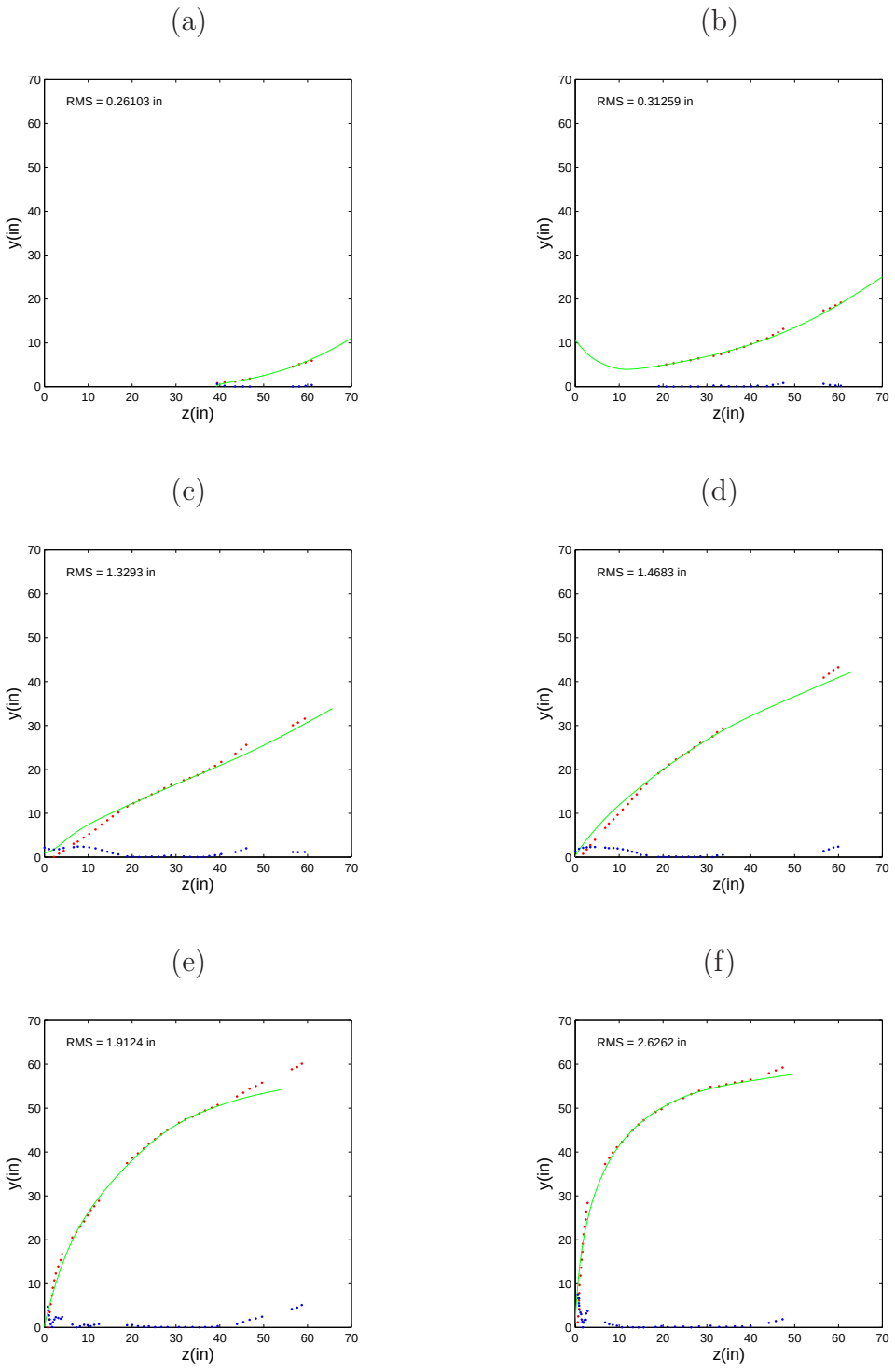

Figure 3.31: Actual and desired profiles of the wave board along with the error distribution for ship speed of 25 knots. Red points: measured profiles of the 2D+T wave board at selected times; Solid green lines: profiles of the 5415 model hull; Blue points: errors. Time is (a) 0.175 s, (b) 0.406 s, (c) 0.642 s, (d) 0.886 s, (e) 1.541 s, (f) 2.240 s.

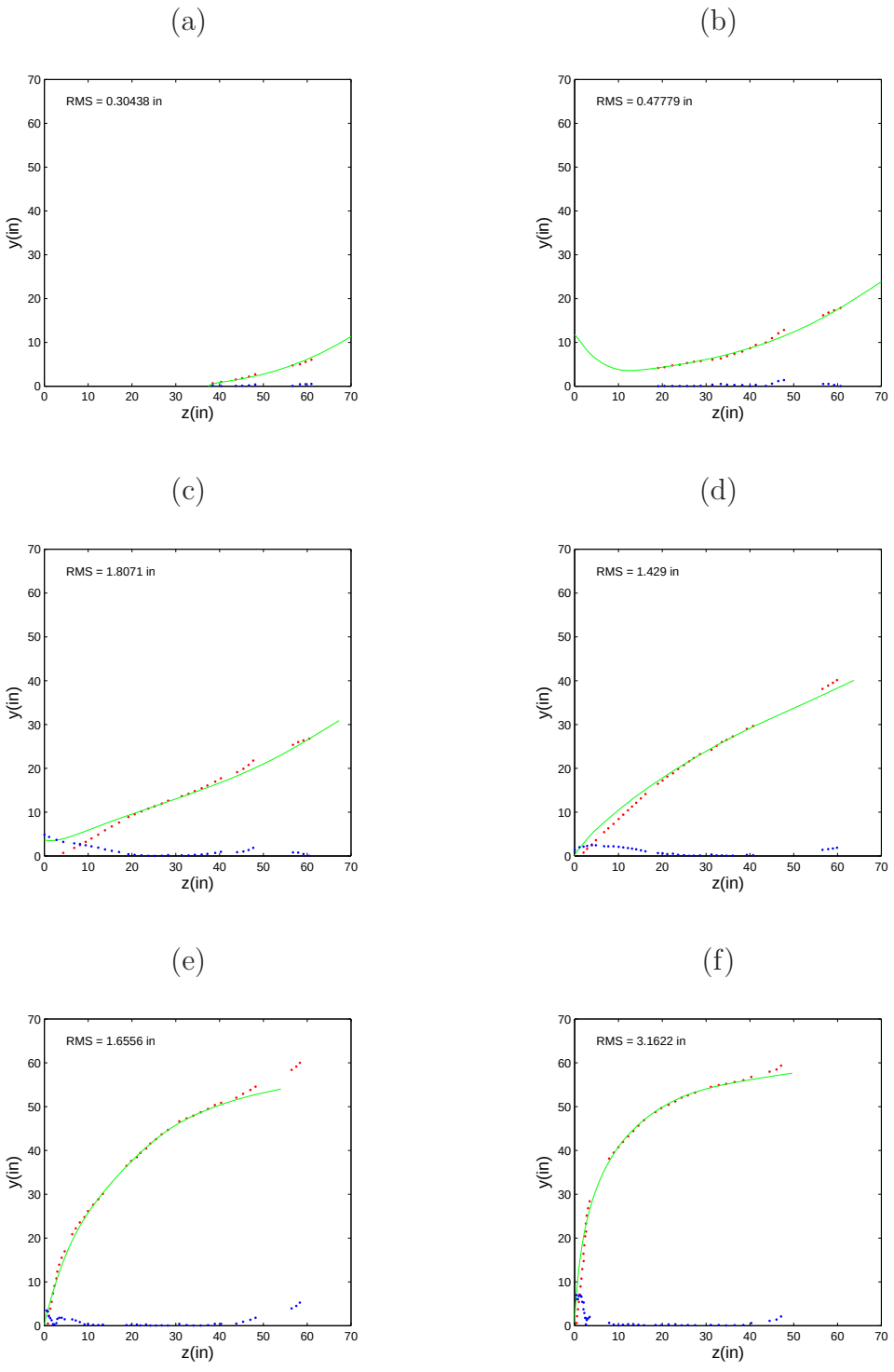

Figure 3.32: Actual and desired profiles of the wave board along with the error distribution for ship speed of 27 knots. Red points: measured profiles of the 2D+T wave board at selected times; Solid green lines: profiles of the 5415 model hull; Blue points: errors. Time is (a) 0.166 s, (b) 0.356 s, (c) 0.513 s, (d) 0.756 s, (e) 1.411 s, (f) 2.030 s.

3.3 Instrument carriage and its towing system

In order to be able to make measurements in a reference frame moving with the top drive channel of the wave maker, an instrument carriage and towing system was designed and constructed. Figure 3.1 shows a schematic of the carriage as well as the wave tank. Figure 3.33 and 3.34 show different views of the towing system. This system consists of the drive assembly, cables, tracks, instrument carriage, and position sensor. The carriage is controlled by the same computer and software that controls the wave maker.

The carriage is powered by a servomotor (3.3 Hp with maximum rpm of 4200 manufactured by MTS Systems Corporation) which through a speed reducer (helical true planetary gear system with a 10 : 1 speed reduction manufactured by Thompson Micron Redimount) drives a horizontally oriented shaft. The motor and drive shaft are mounted on top of the tank about 8 m from the retracted position of the wave board. Two Aluminum drums (6 inches in diameter and 6 inches long) are mounted with a key system on the drive shaft; one drum is positioned near each of the long side walls of the tank. Each drum has a helical groove machined into its surface and has two stainless steel wire ropes (1/8-inch diameter) wound around it; one end of each rope is attached to the drum at opposite ends of the drum. The other end of one of the cables on each drum is attached to a turn buckle which is in turn attached to the front of the carriage (the side farthest from the wave maker). The other end of the second cable on each drum goes through a pulley mounted on top of the tank behind the wave maker and is then attached to a turnbuckle which is

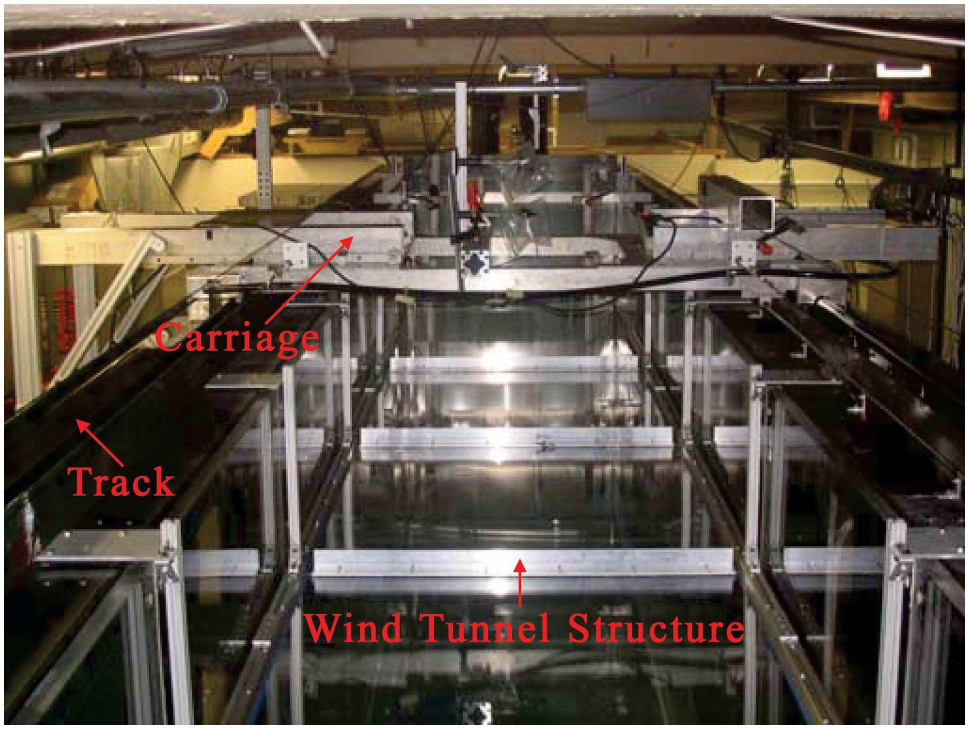

(a)

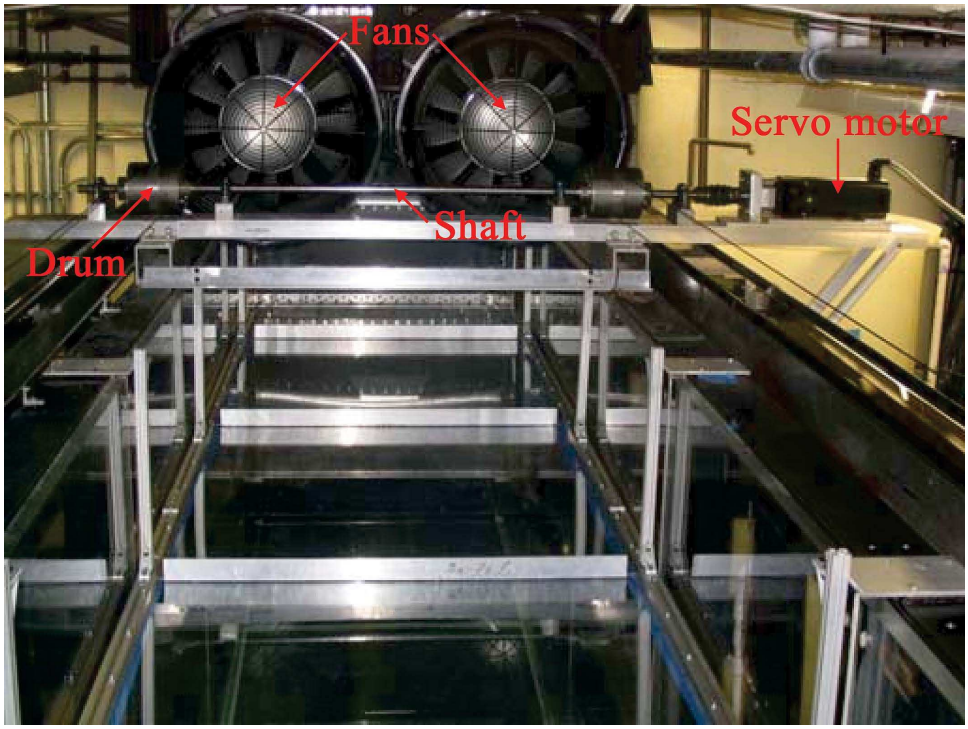

(b)

Figure 3.33: Different sections of the instrument carriage and towing system, (a) the carriage (b) the towing system

(a)

(b)

Figure 3.34: Different sections of the instrument carriage and towing system, (a) guiding bar (b) track

in turn attached to the back of the carriage. The turn buckles are used for fine adjustment of the tension of the cable. As the drum turns, one of the cables on each drum is wound onto the drum while the other is unwound. Thus, the drive system can supply force to the carriage in both forward and backward directions.

The carriage is supported by four hydrostatic oil bearings that ride on precision rails, one on either side of the tank. When high-pressure oil is supplied to the bearings, a thin film of oil is forced between the bearings and the tracks. This oil layer dramatically reduces vibration and friction levels when the carriage is in motion. Precise motion profiles for the carriage are obtained by the same means used for the drive channels of the wave maker. Position feedback is provided by a precision position sensor that is attached to the tank and extends over the length of travel of the carriage. The position sensor readings are used by the PIDF software to obtain precise repeatable carriage motions. In most cases, the carriage motion was set to follow the top channel of the wave maker; however, for a few experimental runs, the motion was adjusted to follow the wave crests. The maximum speed and acceleration of the carriage towing system are 3.1 m/s and 6 m/s^2, respectively.

The variation of the height of the carriage above the undisturbed water surface in the measurement area was recorded since this variation will create an error in any optical measurements of the water surface height done using instruments attached to the carriage. To perform this measurement, a height gauge consisting of long rod with a sharp conically shaped end and mounted on a vertically oriented traverser was attached to the carriage. The sharp tip of the rod was brought down to touch the water surface. The carriage was then moved slowly and the relationship of the

tip of the rod and the water surface was observed. It was found that the variation in height of the carriage was about 2 mm over the measurement region.

3.4 Water treatment

Water treatment is crucial in these experiments because surfactants can strongly affect the wave breaking process. The following procedures were followed to keep the water clean.

At the beginning of each measurement series, the tank is filled with tap water through two cartridge filters and a diatomaceous earth filter. Hypochlorite is then added to the water (10 ppm) to neutralize organic materials. A recirculating skimmer/filtration system is used. In this system, the surface water is removed through a surface skimmer, see Figures 3.1 and 3.35. The skimmer has a cylindrical shape and is mounted horizontally on the side wall of the tank at the same height as the undisturbed water surface at the far end of the tank from the wave maker. Water enters the skimmer through a 2 cm high by 1.2 m long slot with a smooth lower edge. The flow circulation rate is controlled such that a very thin layer of water near the surface enters the skimmer. Water from the round tank is pumped through a diatomaceous earth filter and sent back into the wave tank at a point near the wave maker. The water is treated in this manner for two days before measurements are made. Just before a measurement, the chlorine level is reduced to about 2 ppm by addition of hydrogen peroxide. Low chlorine level is required to maintain the fluorescent dye that is added to the water for the surface profile measurements.

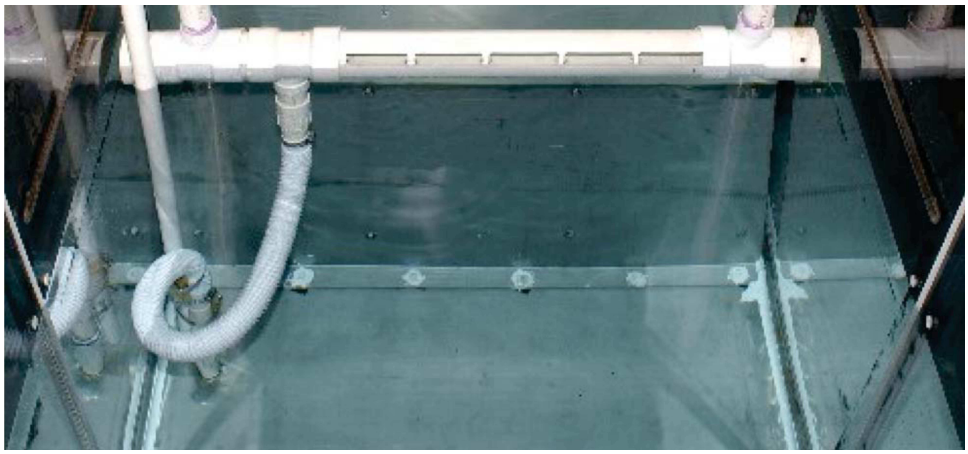

Figure 3.35: A picture of the skimmer system

3.5 Wave measurements

The histories of the surface profiles of 2D+T wave system are measured with a photographic technique as described below.

3.5.1 Measurement equipment and setup

A schematic layout of the setup for the wave profile measurements is shown in Figure 3.36. The purpose of the system is to record the surface profile at the center of plane of the tank in a moving reference frame. The measurement system has three main components: a light source, optics, and a high-speed digital camera. Each component is discussed below.

The light source for the imaging system is an Argon Ion laser (Coherent) operating in all lines mode at a continuous power level of 3.7 Watts. The laser is positioned about 1 m off the floor on a table next to the wave tank at the end with the wave maker. As it exits the laser, the beam is pointing horizontally in a direction toward the far end of the tank and roughly parallel to the long side wall.

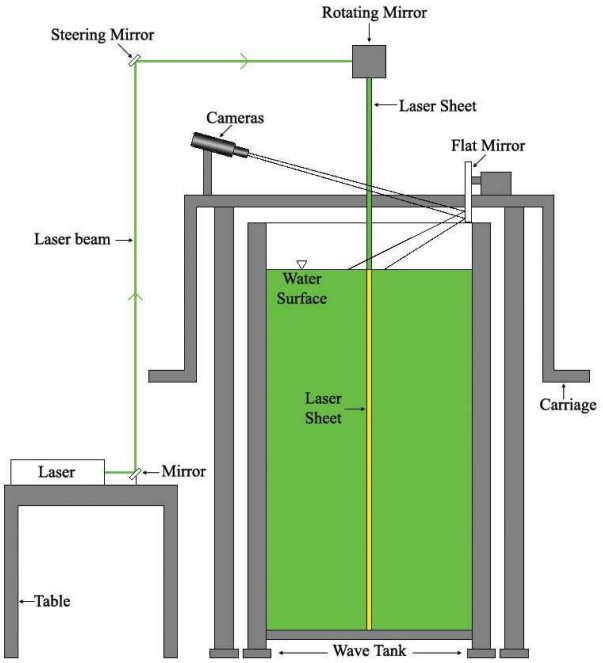

Figure 3.36: A schematic of the imaging setup

Figure 3.37: A picture of the light source: a 5 Watts Coherent laser.

A number of optical components are used to manipulate the laser beam between the light source and the water surface. These optical components serve to redirect the beam, focus the beam on the water surface and spread the beam into a sheet. The redirection of the beam is necessary to take it from the exit of the laser to a position over top of the wave maker and give it a direction that is parallel to the motion of the instrument carriage so that it hits the same spot on the optics mounted on the instrument carriage as it moves along the tank. A system of three mirrors is used for this purpose. The adjustment to make the laser beam hit the optics on the carriage in the same spot regardless of the carriage position is done with the last two of these mirrors along the optical path. In this adjustment, a target is placed in front of the optics on the carriage and the carriage is placed in its starting position. At this time, the position of the laser beam on the target is marked. Then, the carriage is moved to the other end of the tank. If the laser beam is properly aligned, it will still hit the same spot on the target. If not, one of the mirrors is used to move the beam toward the spot. This process is repeated several times until the beam does not move on the target at which point the beam is properly aligned to the motion of the carriage.

The beam is focused onto the water surface with two spherical lenses that are placed along the light path between two of the mirrors. Figure 3.38 shows the configuration of the two lenses mounted on a rail attached to a vertical Aluminum bar. These two lenses have an equivalent focal length which is dependent on the focal length of each individual lens as well as the distance between the two of them. Since the focal lengths of the two spherical lenses are already fixed, the distance

between the two of them is used to adjust the focal distance to occur at the water surface. According to paraxial ray approximation analysis, the minimum thickness of the laser beam at the water surface, is 2 mm, which is quite acceptable. It should be noted that as the carriage moves, the distance between the laser and water surface changes and so does the thickness of the beam at the water surface. Thus, the focal point of the system was set to be about half way between where the carriage starts and ends its motion.

In order to convert the circular laser beam into a laser sheet, a rotating 12-sided polygon with mirrored surfaces was used. Figure 3.39 shows a photograph of the mirror mounted on the carriage. At the point where the laser beam reaches the carriage, it is reflected toward the rotating mirror by a single fixed mirror. As the polygonal mirror rotates, the reflected beam translates over an angle of 30° (360/12). The mirror rotates at about 25,000 rpm so during a typical exposure of 4 ms for each image of the high-speed camera (see discussion below), the laser scans the field of view about 20 times and appears to the camera as a light sheet. There are two parameters that let us control the width of the laser sheet at the water surface and the angle at which it hits the water surface. The width of the laser sheet at the water surface is controlled by the height of the mirror from the water surface. It should be noted that the power of the light at the edges of the laser sheet diminishes as the laser beam rolls over from one facet of the rotating mirror to the other. Therefore, we make sure that the laser sheet is sufficiently bigger than the camera view at the water surface to eliminate these low intensity regions from the images. The angle of incidence of the laser sheet is controlled by the angle of the

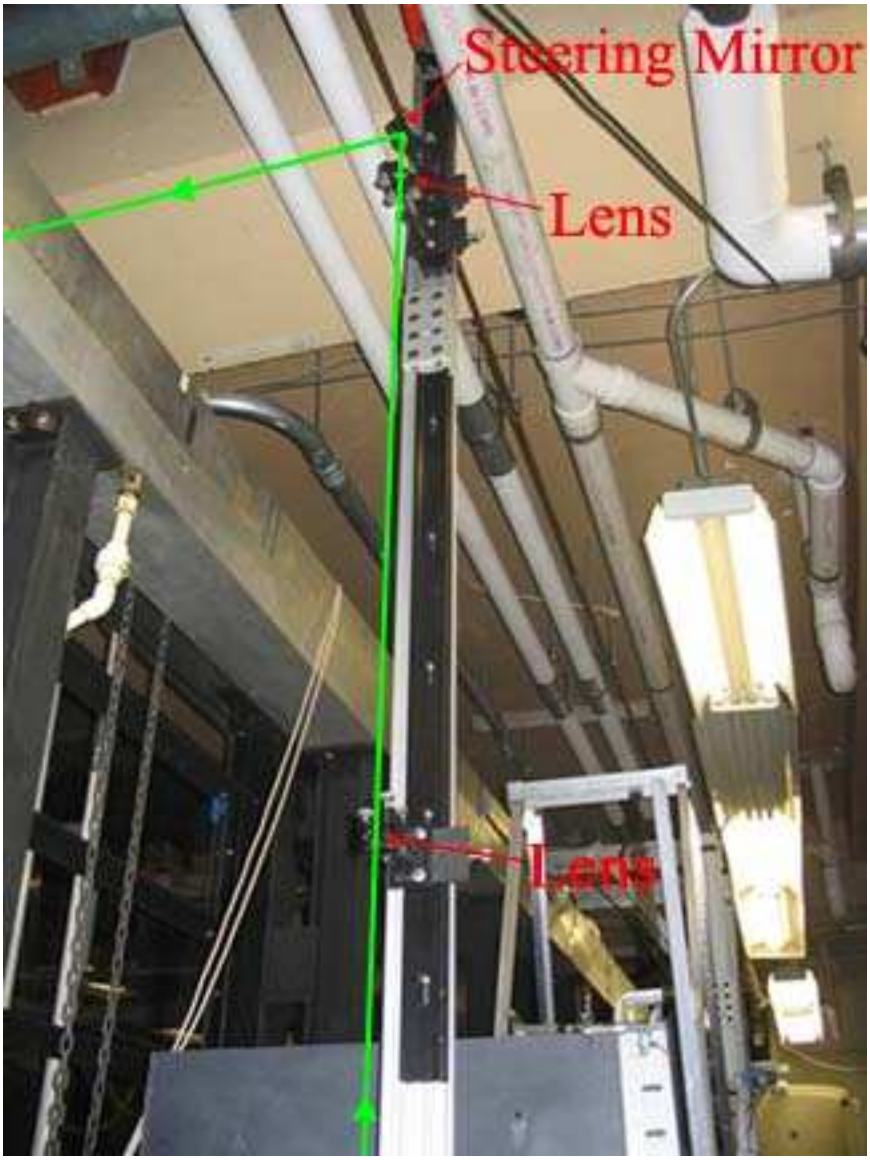

Figure 3.38: Configuration of the two lenses used for focal length and laser thickness adjustment

beam input to the rotating mirror. In this series of experiments, we set the laser sheet to hit the water surface at an angle of about 45° from vertical directed back toward the wave maker from in front of the wave so that the front face of the wave was properly illuminated.

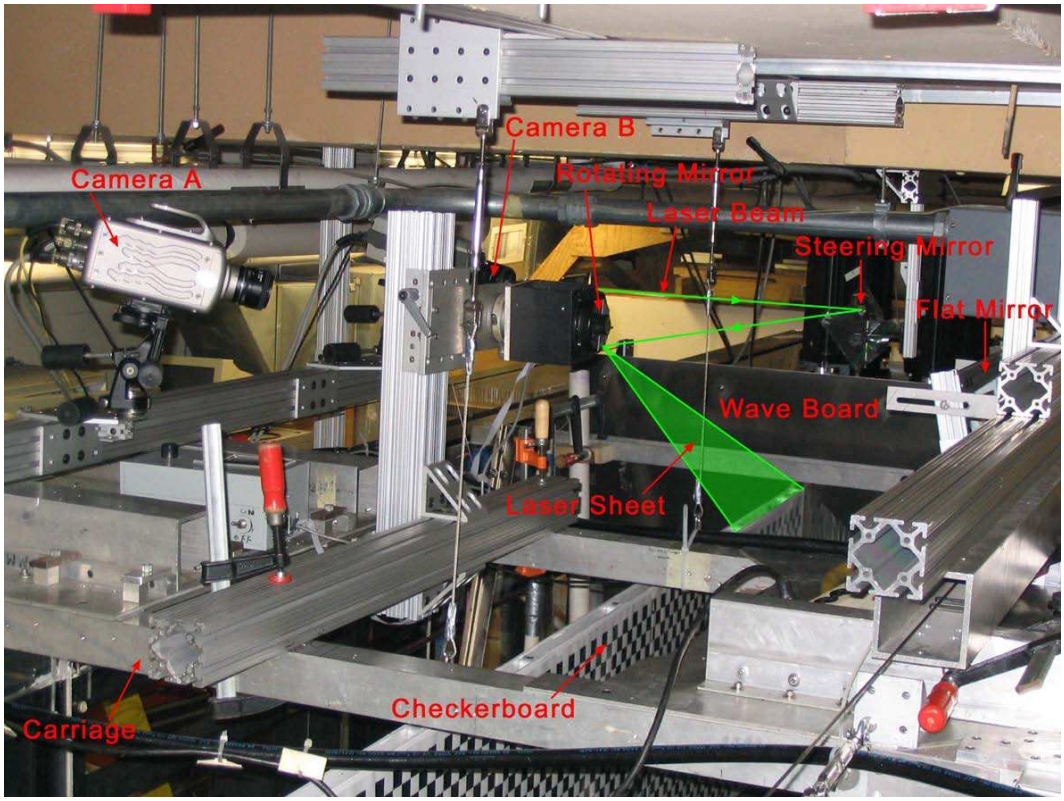

Figure 3.39: The two mirrors for steering the laser beam as well as the rotating mirror used for converting the laser beam to a laser sheet.

The intersection of the light sheet and the water surface is photographed with two high-speed digital cameras (Phantom IV, Photographic Analysis Company) which are mounted on the instrument carriage. The water is mixed with Fluorescein dye and a long-wavelength-pass color filter is placed in front of the lens of each camera. These filters block any specular reflections of laser light, which can create large white blobs in the images, from reaching the cameras. The cameras record

512-by-512-pixel images with 8-bit gray levels at a frame rate of 256 Hz. The image capture sequences are synchronized between the two cameras. The cameras view the water surface through a long flat mirror which is also mounted on the carriage. This mirror is used to provide greater adjustment to the viewing angle of the cameras relative to the water surface. Figure 3.40 shows a top view schematic of the cameras and the flat mirror mounted on the carriage. The viewing direction of the two cameras is arranged to create side-by-side images of the water surface with an overlap zone of about 20% of the image width. The total width of the two camera view is about 30 inches. Since the wave pattern created by the wave maker can reach a width of about 110 inches at the time of passage of the stern of the equivalent 3D ship, multiple runs with the carriage motion starting a different distances from the wave maker are required to measure the entire wave pattern for a single equivalent ship speed.

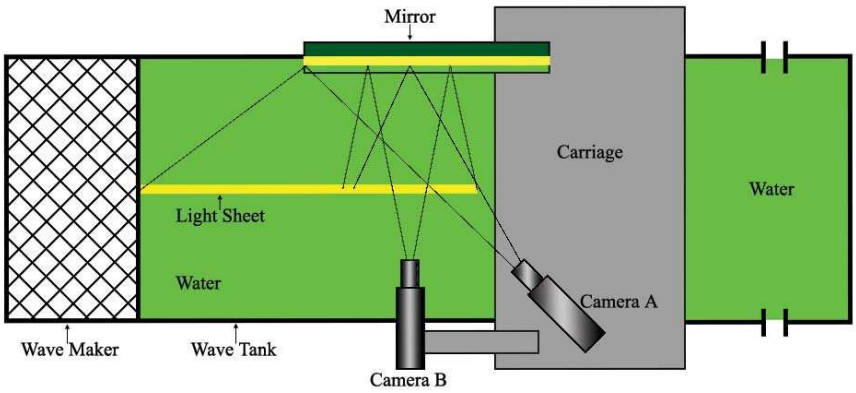

Figure 3.40: A top view schematic of the cameras configuration

3.6 Digital image processing

3.6.1 Wave profile extraction

Movies taken by the high-speed camera are transferred to a desk top computer for processing. The data is later written on DVDs for storage and future use. Each movie carries about 4 s of the wave generation process, containing 1017 images. The images are extracted from the movies and stored in the form of 'bmp' files for further manipulations.

The images record the wave profiles at the center plane of the tank where the light sheet intersects the water surface. Gradient-based image processing techniques are used to extract the profile of the wave from each image.

3.6.2 Camera calibration

The wave profiles movies are taken by two cameras that view the intersection of the light sheet and the water surface from the side. They are oriented at oblique angles to the plane of the light sheet. As a result of this oblique viewing direction the images show a distorted view of the wave profiles and must be transformed before any further processing. In order to transform a point in the image plane into the physical plane (plane of the light sheet), parameters associated with the transformation must be obtained. There are three reference frames used in the transformation process (see Figure 3.41): the grid reference frame ((x_g, y_g, z_g) centered at O_g), which represents coordinates on the physical plane, the camera frame ((x_c, y_c, z_c) centered at O_c), which defines coordinates of points on the space relative to the focal center of the

camera, and the image reference frame ((x_i, y_i, z_i) centered at O_i), that defines the coordinates of points on the image plane. In this last frame, the third coordinate is always zero.

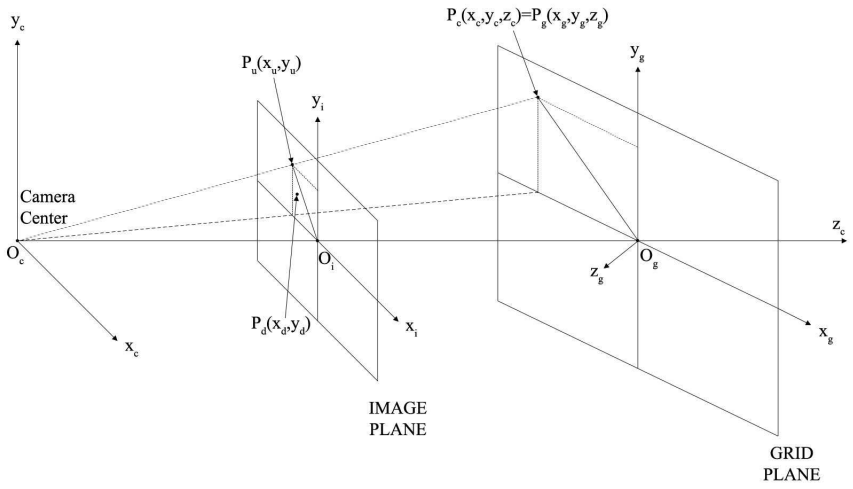

Figure 3.41: A schematic of the coordinates in the camera model

In order to go from grid frame coordinates to camera coordinates, extrinsic parameters are used. Extrinsic parameters account for the relative position and orientation of the camera reference frame to the grid reference frame. Having known the extrinsic parameters, a point given in physical domain coordinates can be transformed to the camera coordinates. As shown in Figure 3.41, let P_g be a point (x_g, y_g, z_g) in the grid reference frame and (x_c, y_c, z_c) be the coordinate vector of this point in the camera reference frame(designated by P_c). These two points are related through the following rigid motion equation:

$$\begin{bmatrix} x_c \\ y_c \\ z_c \end{bmatrix} = R \begin{bmatrix} x_g \\ y_g \\ z_g \end{bmatrix} + T \tag{3.5}$$

where T is the coordinate vector of the origin of the grid pattern in the camera reference frame and R is the rotation matrix in going from the grid reference frame to the camera reference frame. T and R are defined as follows:

$$T = \begin{bmatrix} T_x \\ T_y \\ T_z \end{bmatrix} \tag{3.6}$$

and

$$R = \begin{bmatrix} r_{11} & r_{12} & r_{13} \\ r_{21} & r_{22} & r_{23} \\ r_{31} & r_{32} & r_{33} \end{bmatrix} \tag{3.7}$$

where,

$$r_{11} = \cos\beta\cos\gamma$$

$$r_{12} = \cos\gamma\sin\alpha\sin\beta - \cos\alpha\sin\gamma$$

$$r_{13} = \sin\alpha\sin\gamma + \cos\alpha\cos\gamma\sin\beta$$

$$r_{21} = \cos\beta\sin\gamma$$

$$r_{22} = \sin\alpha\sin\beta\sin\gamma + \cos\alpha\cos\gamma$$

$$r_{23} = \cos\alpha\sin\beta\sin\gamma - \cos\gamma\sin\alpha$$

$$r_{31} = -\sin\beta$$

$$r_{32} = \cos\beta\sin\alpha$$

$$r_{33} = \cos\alpha\cos\beta$$

where α, β, and γ are the angles of the rotation around the x, y, and z axes, respectively.

Once the coordinates of a point are expressed in the camera reference frame, it can be projected on the image plane using the intrinsic camera parameters. In going from the camera coordinates to the image plane coordinates, a camera model is used. In the present work, a pin-hole camera model modified to include lens distortion was used. The simple, undistorted, pinhole camera model uses the idea of perspective projection, see Figure 3.42. Perspective projection is the process of mapping three dimensions onto two. In perspective projection, light rays are constrained to pass through a small hole before they reach the image plane (film plane). This way, each ray connects a point on the physical domain to a single point on the image plane. To simplify the mathematics, the camera is usually modeled by placing the image plane between the focal point of the camera and the object so that the image is not inverted. In Figure 3.41, let P_c be a point in space of coordinate vector (x_c, y_c, z_c) in

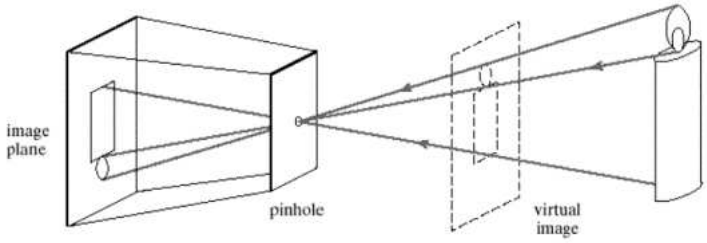

Figure 3.42: A schematic of the camera pinhole model

the camera reference frame and (x_u, y_u) be the projection of the point on the image plane (called P_u). These two points are related through the following geometrical equation:

$$\begin{bmatrix} x_u \\ y_u \end{bmatrix} = \begin{bmatrix} x_c/z_c \\ y_c/z_c \end{bmatrix} \tag{3.8}$$

In the above equation, (x_u, y_u) was obtained for a unit length of the camera focal distance. The effective focal distance of the camera will be added later in the derivation.

Due to lens distortion, the point on the image plane is actually at x_d which is defined as follows:

$$\begin{bmatrix} x_d \\ y_d \end{bmatrix} = \left(1 + k_1 r^2 + k_2 r^4 + k_5 r^6\right) \begin{bmatrix} x_u \\ y_u \end{bmatrix} + \begin{bmatrix} dx \\ dy \end{bmatrix} \tag{3.9}$$

where $r^2 = x^2 + y^2$ and (dx, dy) is the tangential distortion vector.

$$\begin{bmatrix} dx \\ dy \end{bmatrix} = \begin{bmatrix} 2k_3 xy + k_4 \left(r^2 + 2x^2\right) \\ k_3 \left(r^2 + 2y^2\right) + 2k_4 xy \end{bmatrix} \tag{3.10}$$

The above distortion model was first introduced by Brown (1966) and called "Plumb Bob" model. The tangential distortion is due to decentering or imperfect centering of the lens components and manufacturing defects in a compound lens. Once distortion is applied, the final pixel coordinates (x_p, y_p) of the projection of P_p on the image plane can be obtained.

$$\begin{aligned} x_p &= f_1 \left(x_d + \alpha y_d\right) + c_x \\ y_p &= f_2 \ y_d + c_y \end{aligned} \tag{3.11}$$

Therefore, the pixel coordinate vector is related to the distorted coordinate vector through the following equation:

$$\begin{bmatrix} x_p \\ y_p \\ 1 \end{bmatrix} = K \begin{bmatrix} x_d \\ y_d \\ 1 \end{bmatrix} \tag{3.12}$$

where K is the camera matrix and is defined as:

$$K = \begin{bmatrix} f_1 & \alpha f_1 & c_x \\ 0 & f_2 & c_y \\ 0 & 0 & 1 \end{bmatrix} \tag{3.13}$$

The focal distance f_1 and f_2 are very similar. The ratio f_2/f_1 is called "aspect ratio". If the CCD arrays have unequal vertical and horizontal spacing, this ratio is a number other than 1. According to this model (0,0) is the center of the upper left pixel of the image. As a result, (nx-1,0) is the center of the upper right corner pixel, (0,ny-1) is the center of the lower left corner pixel, and (nx-1,ny-1) is the center of the lower right corner pixel, where nx and ny are the width and height of the image.

For camera calibration an inverse mapping needs to be done. There exists a toolbox in MATLAB that does camera calibration (Bouguet(2004)). In order to calibrate a camera, a print of a checker board is needed. Several pictures of the checker board are taken to be used to recover the camera intrinsic parameters. Figure 3.43 shows an example of the image of the checker board with its reference frame used in the present work. Using the calibration toolbox, camera intrinsic parameters as well as the extrinsic parameters associated with each image are extracted. Now that the camera parameters are obtained, we use the grid image, taken during our experiments, to get its extrinsic parameters.

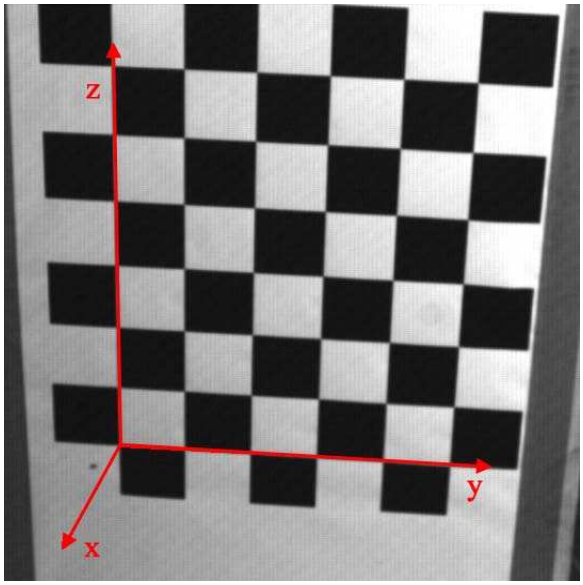

Figure 3.43: A picture of the grid showing the grid reference frame

3.6.3 Camera-wavemaker synchronization

After obtaining the camera parameters and using an inverse mapping, every point on the image is transformed to its corresponding point on the physical plane. As mentioned before, the camera sits on the carriage which moves with the wave maker top channel. In order to get the relative position of each profile with respect to the wave board, the displacement of the carriage and consequently the camera needs to be added to the horizontal coordinates of each wave profile.

The computer that controls the wave maker and the carriage was programmed to send a trigger signal to the camera to start recording at the same time it sends a signal to the carriage to start moving. However, it was found that there is a repeatable time lag of 0.43 s (110 frames in the movies) between the time the camera starts taking pictures and the time that the carriage starts moving. This time lag is likely to be due to the springiness of the long steel carriage drive cables. In order to

relate the frame number in the high-speed movies to the wave maker and carriage position readings recorded by the computer, this time lag was used.

3.6.4 Test procedure

The series of tests to measure the water surface profiles for one equivalent ship speed takes about one day of laboratory time. The steps taken each day to obtain these measurements are given below. It is important to keep the water level fixed during the entire experiment to ensure that the depth-based Froude number is the same and, therefore, the wave generation conditions are constant. This is particularly important since, for a single ship speed the surface profile is patched together from images taken in separate experimental runs. Therefore, the water level is checked and, if needed, adjusted by adding fresh water or draining the existing water in the tank before each individual test. In addition, the dye concentration in the water is frequently examined. Having the optimum amount of dye ensures that the wave images are sharp and bright enough for the subsequent image processing. Also, the water surface in the tank needs to be clean over the entire course of the measurements as dirt and surfactants can alter the dynamics properties of the free surface and also degrade the images of the wave. Therefore, the water surface skimming system is run for about one hour in the morning, one hour at midday, and whenever there is a break during the experiments.

The optical system consisting of the laser, cameras, and the laser sheet is checked before any set of measurements. First, the laser needs to be run for about

30 minutes at the beginning of the day. Then laser sheet is checked to be in the center plane of the tank over the travel distance of the instrument carriage. Finally, the camera orientations are adjusted so that the field of view of each camera overlaps the other and the combined field of view covers the location where the the laser sheet intersects the water.

Before any set of experiments, the calibration grid is placed at the same plane as the laser sheet and an image is taken which is used later to determine the external parameters for each camera, see above. In order to make sure that the measurements are made correctly, a new picture of the calibration grid is also taken at the end of each day of experiments. Finally, a movie is taken with the wave maker stationary and the carriage undergoing its normal motion. These movies of the flat water surface are required to determine $z = 0$ and the horizontal plane at each location in the tank during the image processing.

Once the above steps are completed, the wave maker is set to run along with the instrument carriage and the series of wave profile measurements begins. Each run takes about 30 minutes, which includes the time needed to retract the wave maker and allow the water to come to rest. During this waiting period, the data files and the movies are saved to be used later for image processing. Movies for each carriage position (zones 1, 2, 3, and 4) are repeated three times in order to make statistical studies of fluctuating free surface features caused by turbulence.

Chapter 4

Development of a Holographic PIV system for velocity and bubble measurements

4.1 Introduction

The basic ideas of holography was originated by Dennis Gabor (1948). With the advent of the laser, it caught the excitement and imagination of the scientific community and has become an active field of applied research around the world.

The most striking feature of any hologram is the three-dimensional image that it forms. The light arriving from the hologram into the eyes of the viewer is physically the same as light emitted from the original object. Thus, the viewer can see the object in the hologram from many viewing directions. This means that if a hologram is broken into small pieces, the entire image can be seen through any small piece, that is the image is not clipped. Depending upon the location of the piece viewed, the perspective is different. This resembles precisely the act of looking through a hole in a covered window. Depending on the location of the hole, the outside scene is perceived in its entirely, but from a different perspective. Holograms offer both real and virtual images. An image is said to be real if it can be projected and focused onto a screen. Otherwise, it is called a virtual image.

In general, the definitions are parallel to those used for classical optics concerning lenses and mirrors.

There are two types of holograms: transmission holograms, and reflection holograms. Transmission holograms are always viewed by having the illumination behind the hologram on the side opposite from the viewer. The light transmits through the film to form the image that the viewer sees. On the other hand, a reflection hologram is a type in which the illuminating source is on the same side as the viewer. Light is reflected off the hologram to form the image observed.

Holographic particle image velocimetry (HPIV) has been recently employed to measure the velocity field of a 3D flow. Advances in laser technology provide the possibility of using the holographic recording technique in large volumetric flow field measurements. Moreover, improved digital image acquisition and processing hardware along with complex software tools make evaluation of 3D data sets feasible within useful time scales. Conceptually, holographic PIV is an extension of planar particle image velocimetry (PIV). This technique is based on recording double exposure holograms of a flow field with microscopic interrogation objects such as small particles or bubbles. Reconstruction makes it possible to scan a 3D frozen image of a sample volume. By measuring the displacement of the particle traces, using correlation technique, and knowing the time separation between the two exposures, local velocities are determined (Adrian 1991). The apparent advantage of HPIV over PIV is that it measures the instantaneous 3D velocity field over a deep sample volume, while maintaining high measurement accuracy.

There are two basic optical schemes in holographic particle image velocimetry:

in-line holography and off-axis holography. In in-line holography, a collimated laser beam illuminates the sample interrogation volume located along its optical axis. A holographic film is placed normal to the optical axis and records the interference pattern created by the forward scattered light from the objects and the undisturbed part of the light beam. Despite its simple implementation, it suffers from two main disadvantages. First, the reconstructed images are subject to substantial amount of speckle noise, mostly due to the overlap of the reference beam, real and virtual images (Collier 1971). Second, the objects must have a fairly low population in the sample volume, since the reference beam, whose coherence must be preserved, passes through the sample volume. The quality of the reference beam deteriorates, due to large particle population. On the other hand, the second basic HPIV technique, off-axis holography, employs a separate reference beam. In this technique, the overlapping problem is easily eliminated and, as a result, the speckle noise in the reconstructed images is substantially removed. It also allows for higher spatial resolution. A typical off-axis holographic scheme utilizes side scattered light from the objects, which is 2 or 3 orders of magnitude lower in intensity than forward scattering, depending on the particle size and the scattering angle. Low scattering efficiency requires use of more powerful lasers and larger seeding objects, which is problematic for velocity measurements.

A variety of optical configurations have been proposed and implemented to overcome the drawbacks of these two basic schemes, which usually require more sophisticated optical setup. Many successful attempts have been made to measure instantaneous, 3D velocity fields within a sample volume with high spatial reso-

lutions. Barnhart *et al.* (1994) developed a phase-conjugate, off-axis holographic system to measure the air flow in a turbulent pipe. In their studies, a stereoscopic, dual subject and reference beam, near-forward scattering setup was used. Meng & Hussain (1995) used an in-line recording, off-axis viewing system to study the instantaneous flow field in a vortex ring. By off-axis viewing, the image overlap in the view field of the camera is successfully removed. However, particle population must be low to maintain the coherence of the beam. Gray & Greated (1993) developed a forward scattering, off-axis system to map the 3D velocity field of a particle suspension sample volume with limited spatial resolution. Zhang & Katz (1994) proposed a hybrid setup. Later, Zhang *et al.* (1997) developed a dual hybrid scheme for measuring 3D velocity fields in a moderately high Reynolds number turbulent duct flow.

4.2 The holographic PIV approach developed in the present study

Figure 4.1 shows a schematic of the optical setup which was developed in the present study and will be used in future work on the measurement of the bubbles generated by breaking waves. This setup is similar to that used by Zhang & Katz (1994). In this approach, the subject beam illuminates the sample volume along the optical axis. The current optical setup is very similar to in-line holography, except that the undisturbed part of the subject beam is blocked out. Instead, a separate beam is used as the reference, resembling an off-axis scheme. A holographic plate records the interference pattern created by forward scattered light from the objects

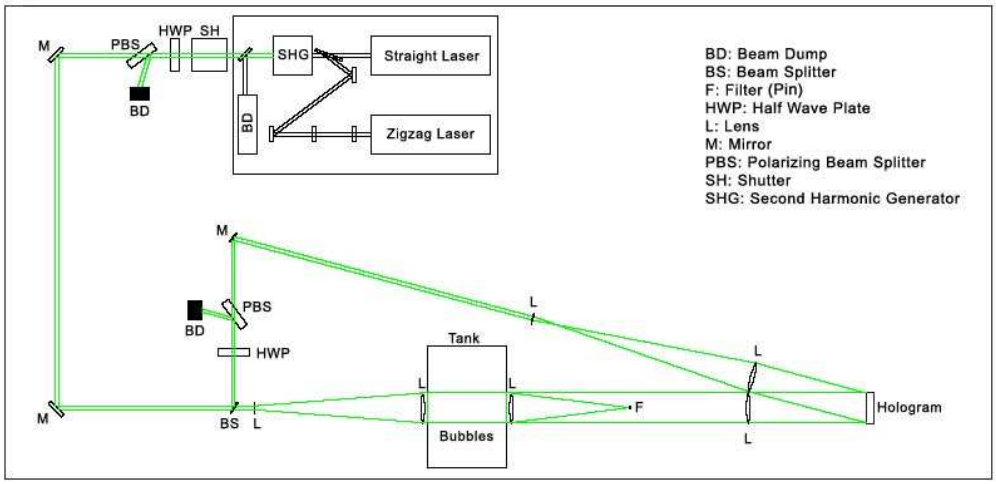

Figure 4.1: A schematic of the HPIV setup used in this study.

and the reference beam.

In order to remove the undisturbed part of the subject beam, two identical achromatic lenses are used between the sample volume and the recording plate. These relay lenses are separated by a distance of twice their focal length and a spatial, high-pass filter (a pin) is inserted between the two lenses. This pin is installed at the focus of the first lens. The undisturbed part of the subject beam, which is parallel to the optical axis, is focused by the first relay lens to its focal point and blocked out by the pin. However, the light scattered from bubbles, except the zero-degree forward scattering, reaches the film with minimum obstruction. It should be noted that the finite diameter of the relay lenses imposes an upper limit on the spatial frequencies and serves as an aperture (field) stop. As a result, larger relay lenses are preferred to collect as much light as possible and to improve the efficiency of the optical system.

The depth of focus of the image (elongation of the objects in depth in the

image) is an important consideration in these holograms. The depth of focus can be defined in the present images as the range of depth within which the intensity level of a spherical image is distinctively higher than its background. The present setup is expected to have less elongation in the depth direction than in a typical in-line system where the undisturbed subject beam is used for the reference beam. The reason for this smaller elongation is the removal of the zero-degree, forward scattered light by the high-pass filter. In a typical in-line holographic system, this zero-degree, forward scattering light is dominant, which may result in greater elongation.

In the present setup, both the wavelength and the angle of the reconstruction beam are different from the recording reference beam. When different wavelengths and reference angles are used during the recording and reconstruction processes, spatial distortions in the reconstructed images occur, which include both lateral (in-plane) and axial (in-depth) distortions. These distortions are a function of the recording and reconstruction reference angles, as well as the reconstruction to recording wavelength ratio. The lateral distortion can be removed by choosing proper reconstruction and recording reference angles. However, since the reconstruction and recording wavelengths are different in this case, the axial distortion can not be eliminated, but be compensated during the data analysis. Fortunately, the axial distortion is just a linear shrinkage (Collier 1971). In the present case, there is a shrinkage of 37%.

In addition to measuring the bubble diameters using this approach, it is possible to determine the two velocity components perpendicular to the optical axis. The reconstructed bubbles have elongated shape in the depth direction. This phe-

nomenon is known as the depth of focus effect (Barnhart *et al.* 1999, Blackshire *et al.* 1994). Since this elongation reduces the spatial resolution in the depth direction, the velocity along the optical axis can not be determined with the same accuracy as the two other in-plane components.

4.3 Optical setup for hologram recording

Like any optical system, the present setup (see Figure 4.1) consists of three main components: a light source, optics, and an optical detector. Figure 4.2 and 4.3 show photographs of the optical configuration for hologram recording. In order to provide velocity measurements, the system should be capable of double exposure. As in regular PIV, the double exposure separation will be adjusted in accord with the estimated flow speed.

The light source is an injection seeded dual Nd:YAG laser (Spectra Physics) with a wavelength and pulse energy of 532 nm and 170 mJ, respectively. It gives temporally separated pairs of laser pulses, each of 8 ns duration, at a repetition rate of 15 Hz. The laser should be fired at its maximum power in order to maintain the beam divergence at the minimum level. The laser system consists of two laser cavities, which are fired using a multi-channel digital pulse generator (Stanford Research Systems), see Figure 4.1. The interval between two pulses from the laser can be adjusted from 1 ns to 66 ms. The laser is equipped with an injection seeder to guarantee sufficient coherence length. The increased coherence length provides high quality holographic recording of a large volume, while allowing mismatched

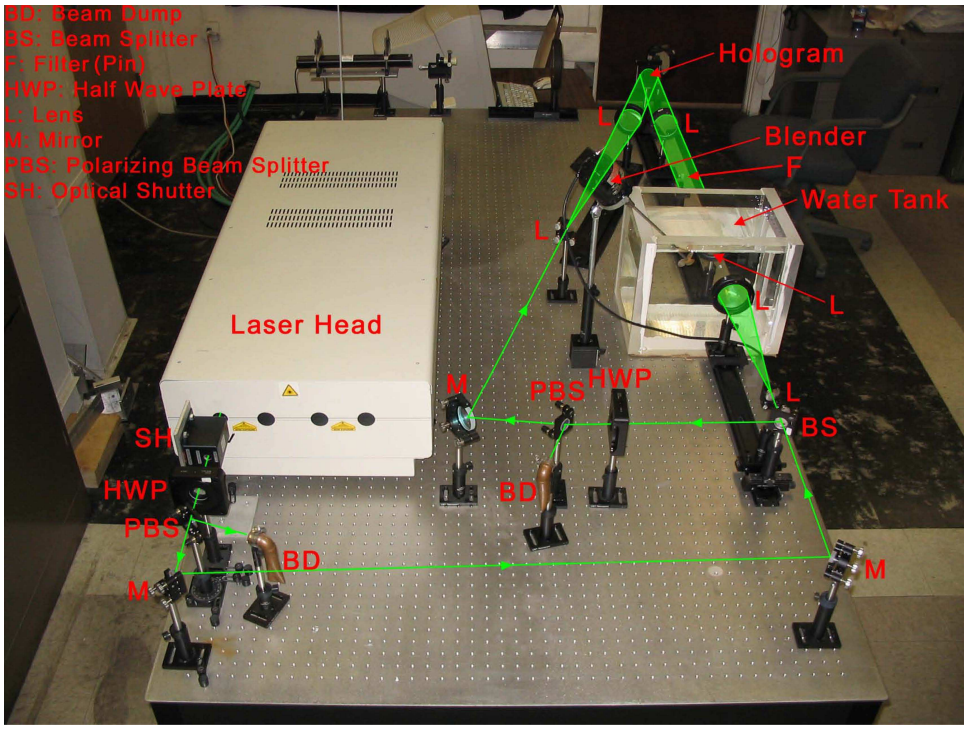

(a)

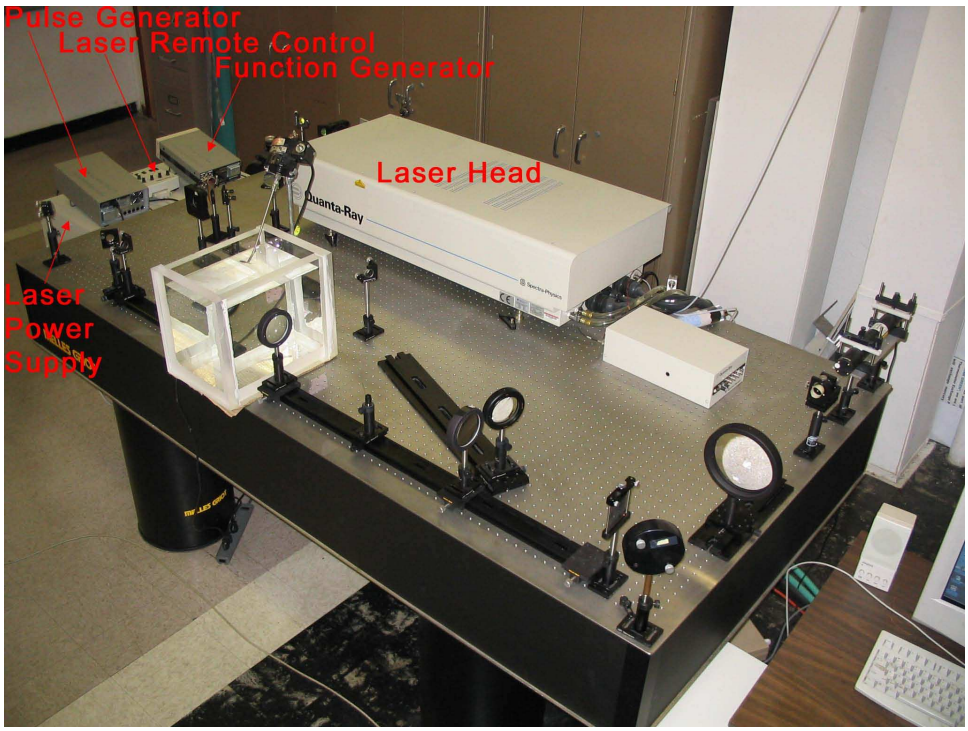

(b)

Figure 4.2: Two views of the holographic PIV setup showing the hologram recording line and the water tank.

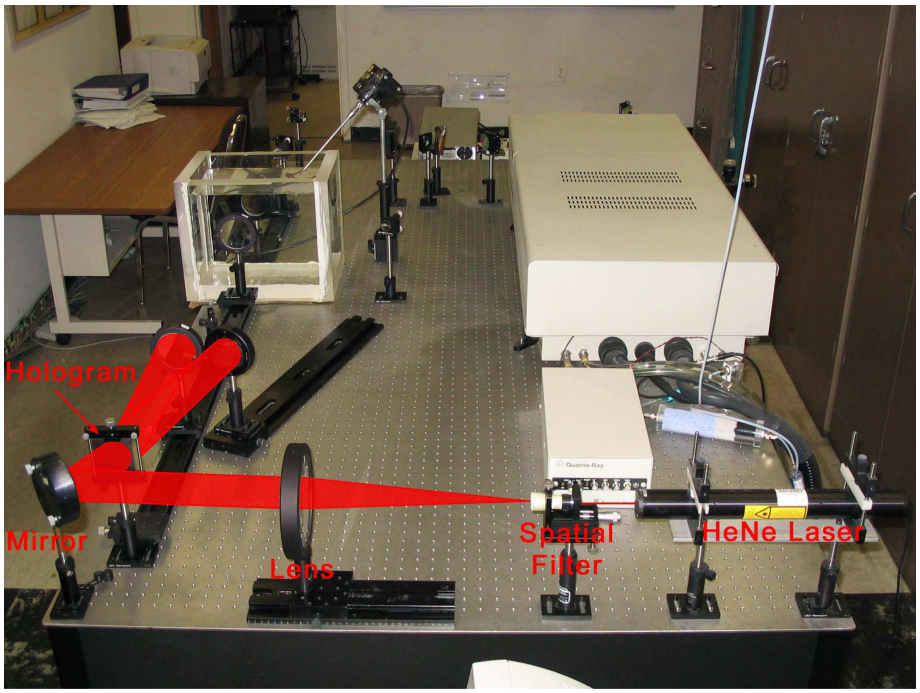

(a)

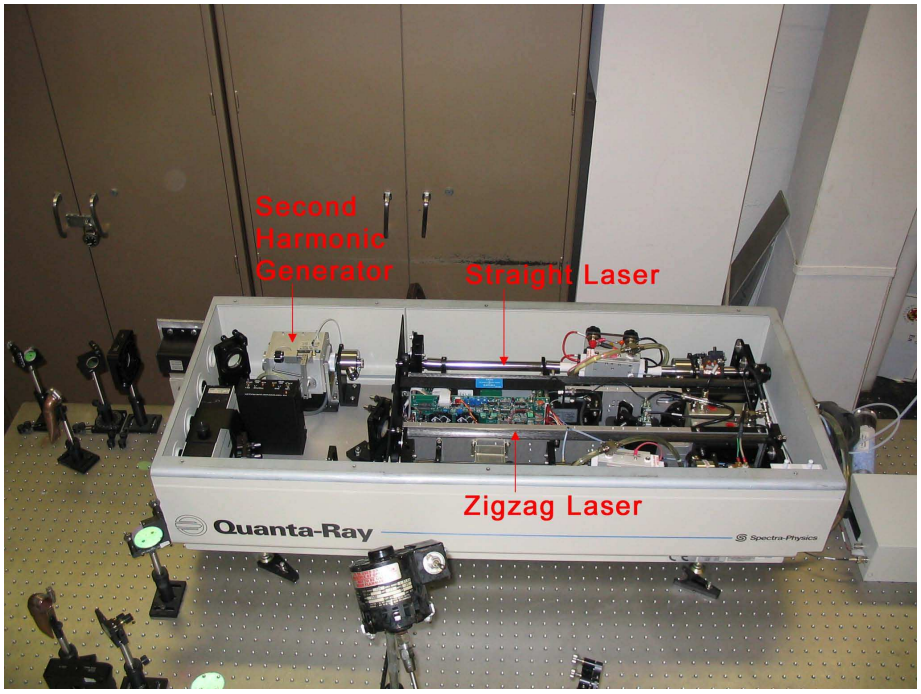

(b)

Figure 4.3: Two views of the holographic PIV setup showing (a) part of the reconstruction line and (b) the laser used for hologram recording.

optical path length between object and reference beams. Each laser head emits a beam, which is vertically polarized.

A number of optical components are used to manipulate the laser beam between the light source and optical detector. To ensure the stable injection seeding operation, the pulsed laser system has to fire constantly during the recording process. Therefore, a high-energy shutter, operated through a synchronizer, is employed to generate a single pair of laser pulses at the desired instant in time, see Figure 4.1. The synchronizer assures that the shutter will pass only one pair of pulses. The the laser pulse that pass through the shutter, are then split into two parts by a partial reflecting mirror that works as a beam splitter. The majority of the light is transmitted to illuminate the control volume. The reflected part is used as the reference beam.

The subject and reference beams are further manipulated before they reach the holographic plate. The subject beam is expanded to 70 mm in diameter with a convex lens, then collimated with a concave lens, and then directed through the tank cross section. After leaving the tank, it goes through the above-mentioned relay lens system to remove the light that is not disturbed by the bubbles. This lens system consists of two achromatic lenses with focal lengths of 300 mm positioned at a distance of 600 mm apart on an optical rail. The spatial filter is placed at the midpoint between the two lenses.

In order to adjust the intensity of the reference beam and, consequently, control the reference to object beam intensity ratio, a variable beam splitter is used. The variable beam splitter consists of a pair of half wave plates and a polarizing beam

splitter. The path length of the subject beam is matched with the reference beam to preserve the coherence length of the beams. The reference beam is then expanded, and collimated. The reference beam should be a high quality plane wave for easy reproduction during the reconstruction. Plane waves are preferred for producing a conjugate beam. The scattered light from bubbles/particles and the reference beam are then projected on a holographic plate.

Holographic plates serve as the optical detector in this system. The holographic plate, which has its emulsion side facing the flow field, records the resultant interference pattern of the subject and reference beams. The hologram is a 63 mm Slavish VRP (green sensitive) plate. For this type of emulsion, the proper exposure for optimal fringe contrast requires 150-400 μJ/cm^2. During each firing of the laser, one frame of the holographic plate is exposed for the duration of the two short laser pulses. To ensure the proper hologram exposure level, a variable beam splitter is used at the exit of the laser to reduce the output energy of the beam. Using this setup, a frozen scene of the sample volume is recorded simultaneously on a double exposure hologram.

4.4 Image reconstruction and data acquisition

A schematic of the image reconstruction setup is shown in Figure 4.4. After the exposed hologram is developed, it is put back into the plate holder in the reconstruction system. The light source is a 5 mW, continuous wave He-Ne laser with a wavelength of 632.8 nm. The beam is spatially filtered, expanded and then

collimated to 70 mm in diameter. To keep optical abberations at the minimum level, the relay lenses and the plate holder in the recording system are integrated into the reconstruction system as a single unit. The hologram is illuminated from its substrate side at an angle. The reconstructed wave front propagates back through the relay lenses and forms a 3D image.

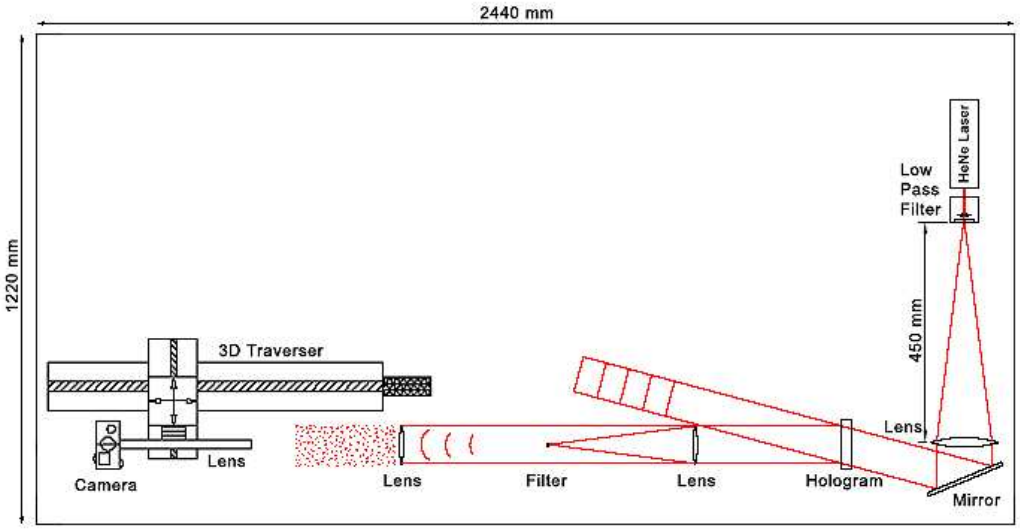

Figure 4.4: Reconstruction set up.

The 3D image is then digitized and saved in a computer using the follow system and procedure. The basic method is to record standard digital images with small depths of field over a 3D grid in the holographic image space. The camera used here was a Nikon D1x which has a sensor array of 3000 $\times$ 2000 pixels. The camera is equipped with a microscopic objective lens (Infinity Photo-Optical Company, Model K2) that has a small field of view and depth of field. The images are saved on the hard disc of a computer for image processing. With the microscopic objective lens setting used herein, each frame corresponds to a field of view of 9×6 mm^2 within the sample volume. This scale translates to a digitization resolution of 3 μm/pixel.

A 3-axis, precision translation stage is employed to move the camera in three-dimensions through the holographic space, see Figure 4.5. This stage is driven by a computer-controlled servo motor. The camera-traverser system is set to scan entire planes normal to the optical axis sequentially until the entire holographic volume has been recorded. In this way, each reconstructed 3D image is broken into a series of slices normal to the optical axis. Having a sample volume with a cross section of 54×54 mm^2, requires 54 images in each plane.

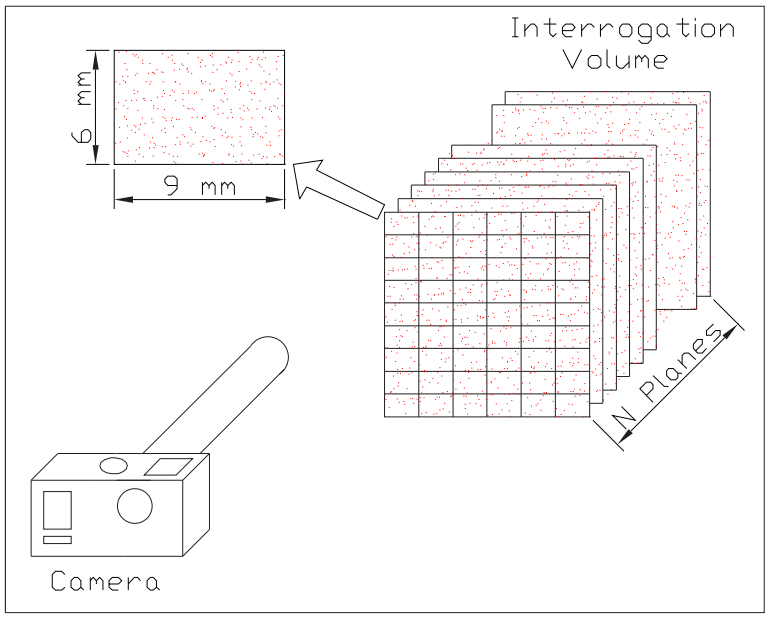

Figure 4.5: Digitization system of the hologram.

4.5 Preliminary testing

Since the wave tank was not ready to perform bubble and flow measurements of breaking bow waves, a small tank was built and used for preliminary tests of the holographic system. This tank is $11 \times 8 \times 9$ in^3 and made of the same plastic

material as the walls of the wave tank. During the experiments, the tank was filled with water, representing the wave tank. The rotating blade of a mixer was positioned very close to the water surface to draw air into the water and create a two-phase flow. The size and population of the bubbles could not be controlled in these experiments, but it was enough for preliminary tests of the optical system. Figure 4.9 shows a sample hologram taken in these experiments.

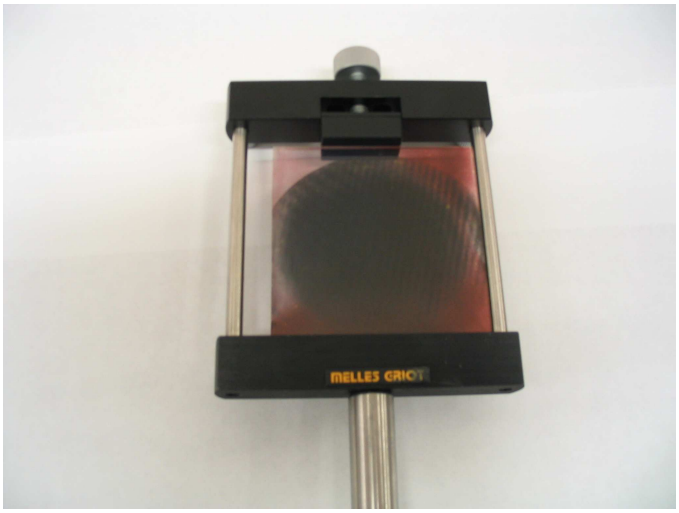

Figure 4.6: A sample hologram.

Figure 4.7 and 4.8 show a sample series of digitized images from the resulting hologram. In this particular case, the traverser/camera system was commanded to move along the depth of the hologram and take images at a spacing of 1 mm. Four images of the control volume taken at depth positions 0, 18, 42, and 60 mm are shown. These images show bubbles that are within the depth of focus of the camera lens. As the camera moves along the optical axis, these bubbles go out of focus and disappear while new bubbles come into the focus.

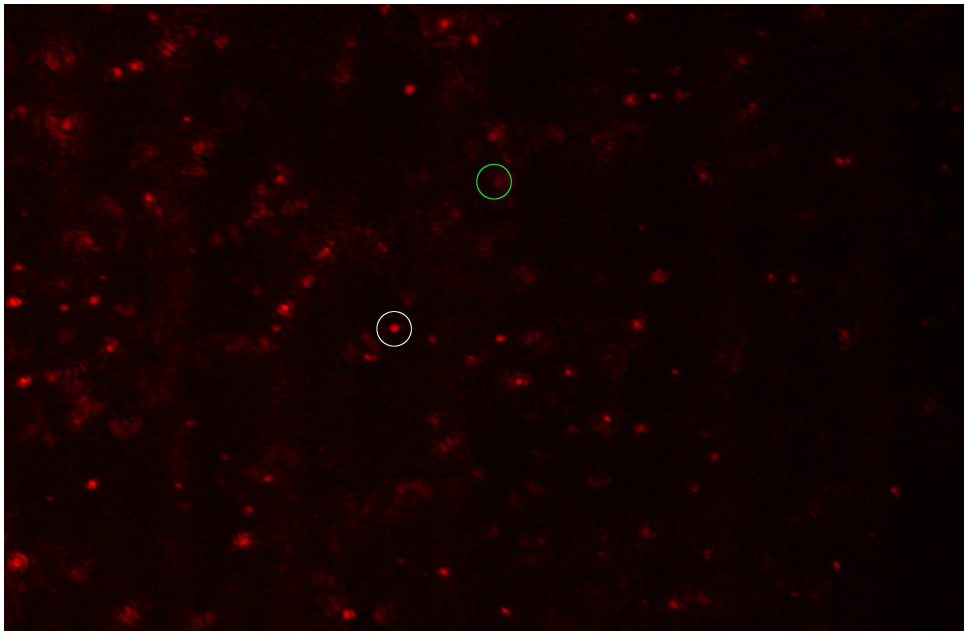

(a)

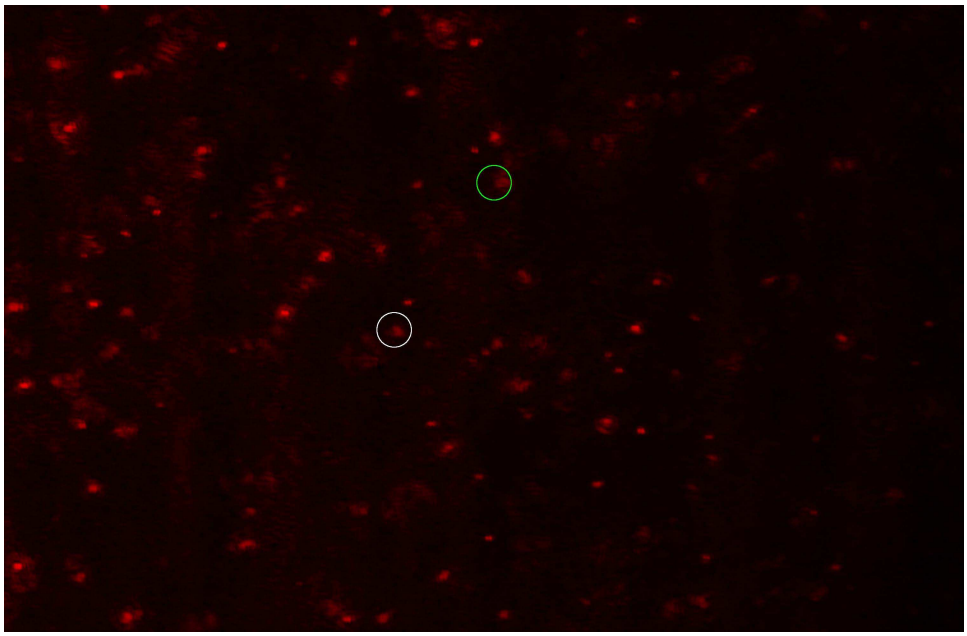

(b)

Figure 4.7: A sample reconstructed image at relative depths of (a) 0 and (b) 18 mm.

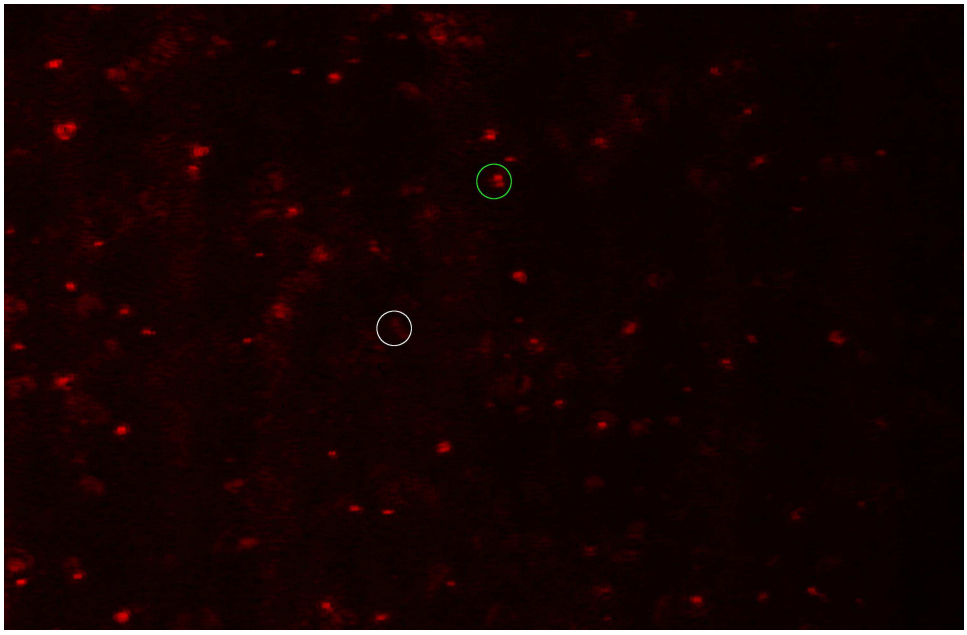

(a)

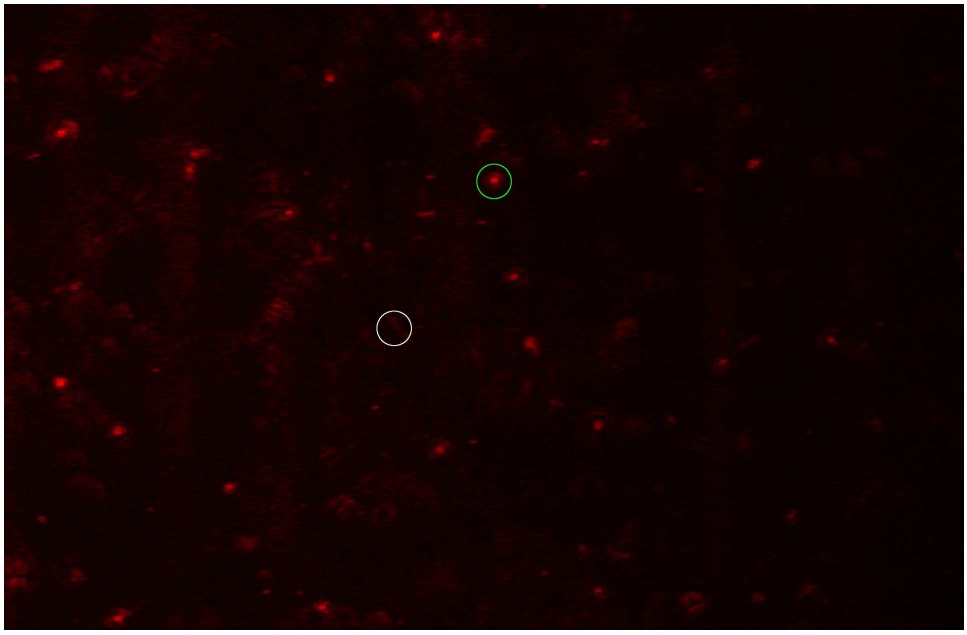

(b)

Figure 4.8: A sample reconstructed image at relative depths of (a) 42 mm and (b) 60 mm.

4.6 Proposed setup for experiments in the large wave tank

As mentioned above, this holographic technique was developed to study breaking bow waves. A schematic layout of the optical configuration for hologram recording in the large tank is shown in Figure 4.9. This system is planned to be used in the near future.

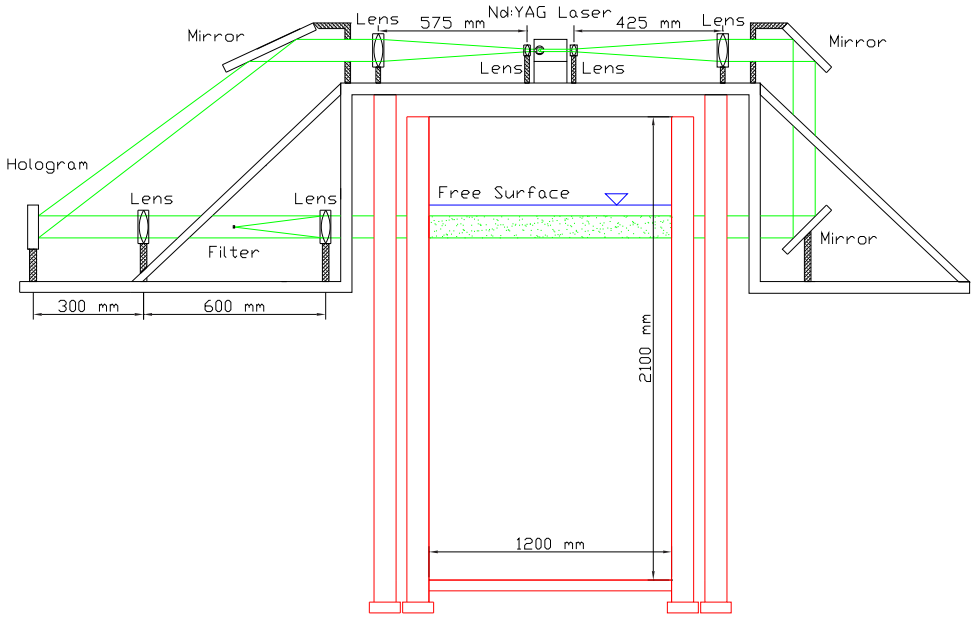

Figure 4.9: A schematic of the current holography (HPIV) configuration.

Chapter 5

Results and discussions

The wave shape data was taken and processed to determine the detailed behavior of the breaking bow wave. In the following, the 2D+T bow wave observations are presented first to show the main features of the bow wave. This is followed by descriptions of the wave patterns around the ship simulator; tests of repeatability of the experiments; motions of the water contact line including trajectories, maximum height, and velocities; wave crest properties such as trajectories, maximum height, and velocities; and jet properties including impact point location, angle of incidence, and jet tip velocities. Data on the maximum splash height is then presented. Finally, a scaling study is presented to examine the effects of the ship speed on some of the above properties.

5.1 The 2D+T bow wave observations

The waves were generated with the 2D+T wave maker at four different equivalent ship speeds: 16.5, 20, 25, and 27 knots. Flow visualization studies using either white light or the above-described surface profile measurement technique (LIF) were first performed to define the main features of the 2D+T bow wave. Since the wave pattern of interest was much wider than the combined field of view of the two cam-

eras, the measurement area was divided into four zones each covering a view of about 30 inches (the combined view of the two cameras). The movies are labeled by the zone number (zone 1 is closest to the wave maker) and the camera designation (A or B with the field of view of camera A closest to the wave maker). The measurements in each zone were, of course, performed in separate experimental runs. Several sets of images from the high-speed LIF movies are presented here to highlight various aspects of the wave generation and breaking process. First, sets of four images taken in zone 1 by camera A at equivalent ship speeds of 16.5, 20.0, 25.0 and 27.0 knots are shown in Figures 5.1, 5.2, 5.3, and 5.4, respectively[1]. For all speeds, the selected photographs were taken at 0.0, 0.371, 0.586, and 0.738 s after the start of the wave maker motion. These photographs were selected to show the breaker formation up to the point of impact of the plunging jet in the higher speed cases. The jet impact and the splash formation are shown in Figure 5.5 which is for an equivalent ship speed of 27 knots. In this figure, the photographs are all from camera B: photographs (a) and (b) are from zone 1; (c), (d), (e) from zone 2; and (f) from zone 3. Finally, Figures 5.6, 5.7, 5.8, and 5.9 show sample images of the wave formation process frozen at the same dimensionless times ($0.0t_0$, $0.16t_0$, $0.23t_0$ and $0.31t_0$, where t_0 is the total time of the wave maker motion) in the wave maker

[1]A light intensity pattern is seen in the foreground of each image. This light pattern originates from the glowing dye within the light sheet. In the high-speed movies, this intensity pattern is viewed from above the water surface with a look-down angle (about 30°); from this view point, any light reaching the foreground of the images from the glowing dye is refracted by the water surface between the light sheet and the camera (see 3.36).

motions at the four equivalent ship speeds. The values of t_0 are 3.393 s, 2.8 s, 2.24 s, and 2.074 s at equivalent ship speed of 16.5, 20, 25, and 27, respectively.

The four equivalent ship speeds were chosen to create a wide range of breaking behavior. At the 16.5-knot speed, the wave becomes quite steep and forms a very weak spilling breaker. A strong spilling breaker is formed at 20 knots. This equivalent ship speed was also used at the Naval Surface Warfare Center, Carderock for tests with the 5415 ship model. Experiments at this speed seemed to be useful as we could compare our findings with the real 3D model (which unfortunately includes a large sonar dome that is not simulated in our laboratory). At the two highest equivalent ship speeds, plunging breakers are found with the size of the plunging jet larger in the 27-knot case.

The photographs in Figures 5.1 to 5.9 can be used to show various aspects of the wave generation process. When the wave maker starts to move, it transmits energy to the fluid. The velocities of water particles that are in contact with the wave board are the same as the velocities of the adjacent material particles that make up the wave board itself. As a result of the horizontal acceleration of the wave board, a high-pressure region forms just under the water free surface. This high-pressure region accelerates the water particles near the free surface into a sheet that climbs up the wave board. This sheet soon forms a wave crest which moves ahead of the wave board. In this phase of the wave formation, the crest takes a smooth flat shape. Once the wave has reached its maximum height, gravity causes the wave to plunge back into the wave front face in the two highest speed cases and form spilling breakers for the two lower speed cases.

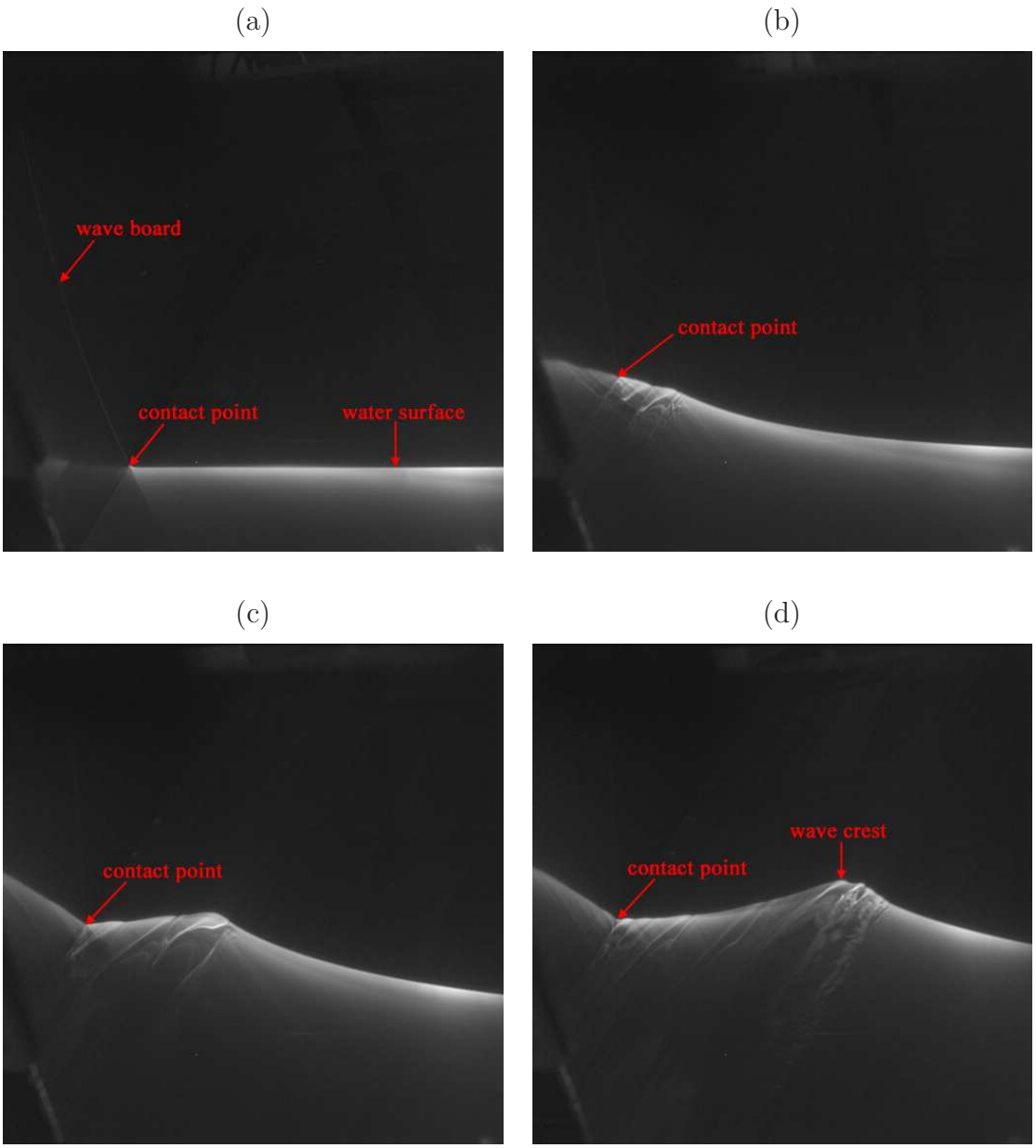

Figure 5.1: Wave formation process at four different times for equivalent ship speed of 16.5 knots. Time is (a) 0 s, (b) 0.371 s, (c) 0.586 s, (d) 0.738 s.

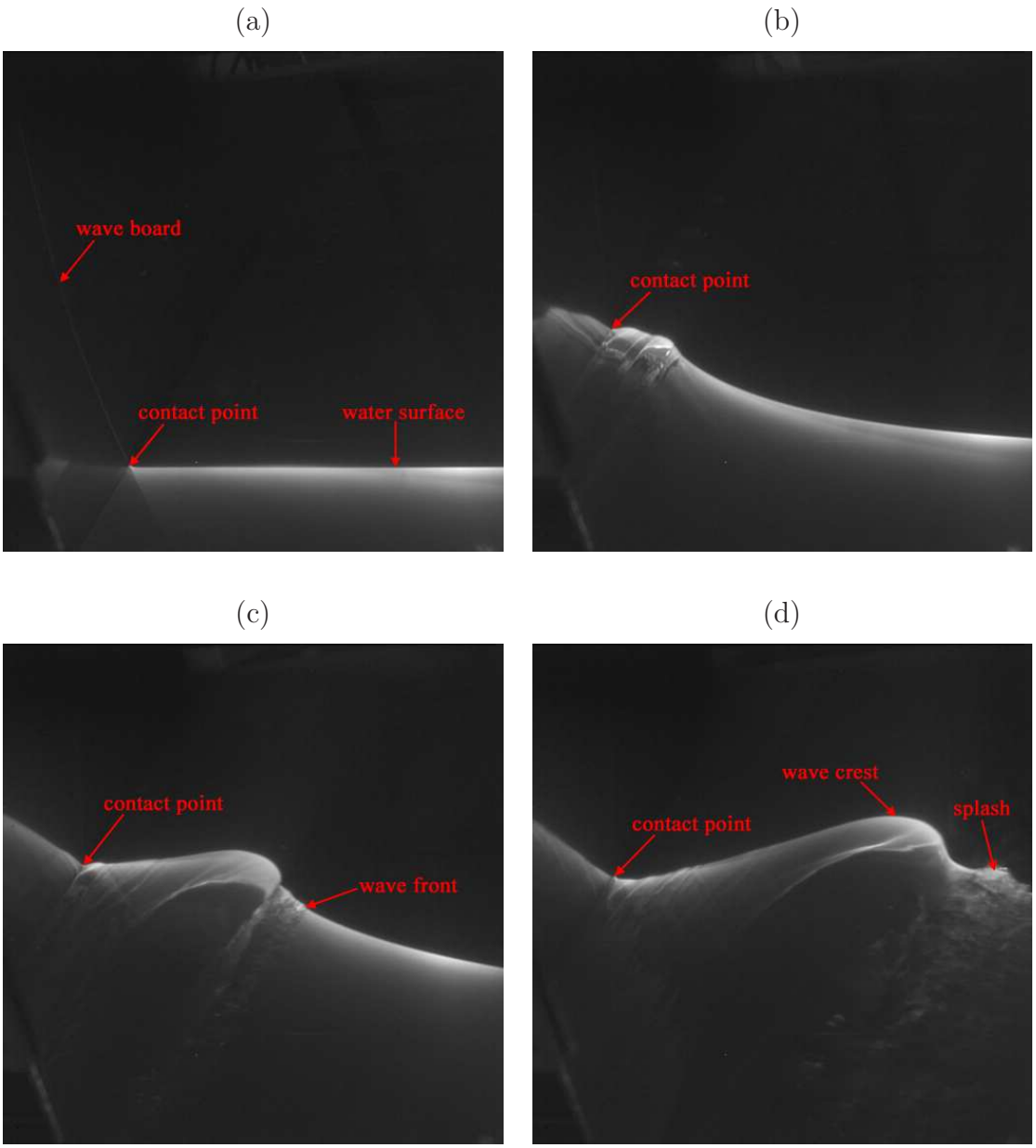

Figure 5.2: Wave formation process at four different times for equivalent ship speed of 20 knots. Time is (a) 0 s, (b) 0.371 s, (c) 0.586 s, (d) 0.738 s.

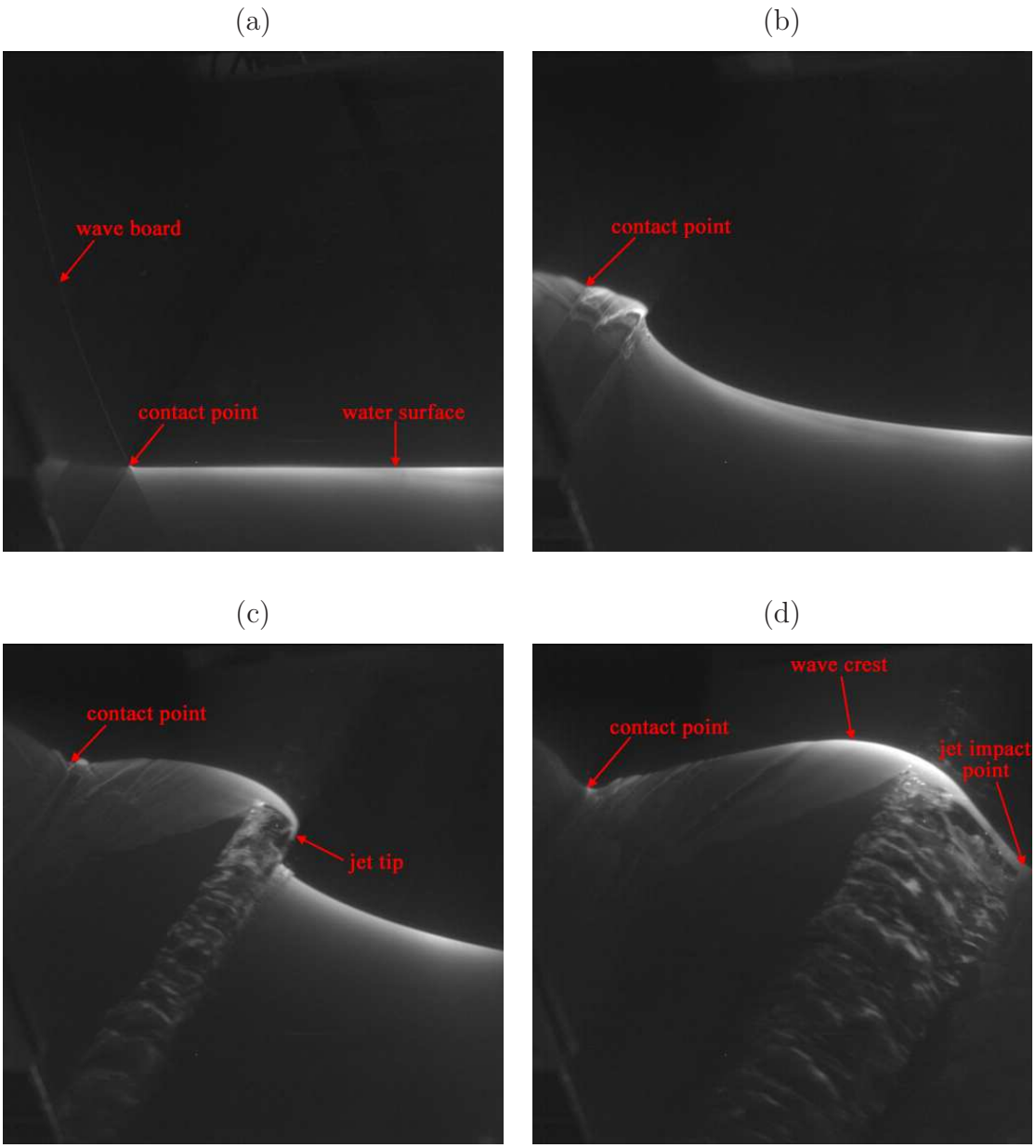

Figure 5.3: Wave formation process at four different times for equivalent ship speed of 25 knots. Time is (a) 0 s, (b) 0.371 s, (c) 0.586 s, (d) 0.738 s.

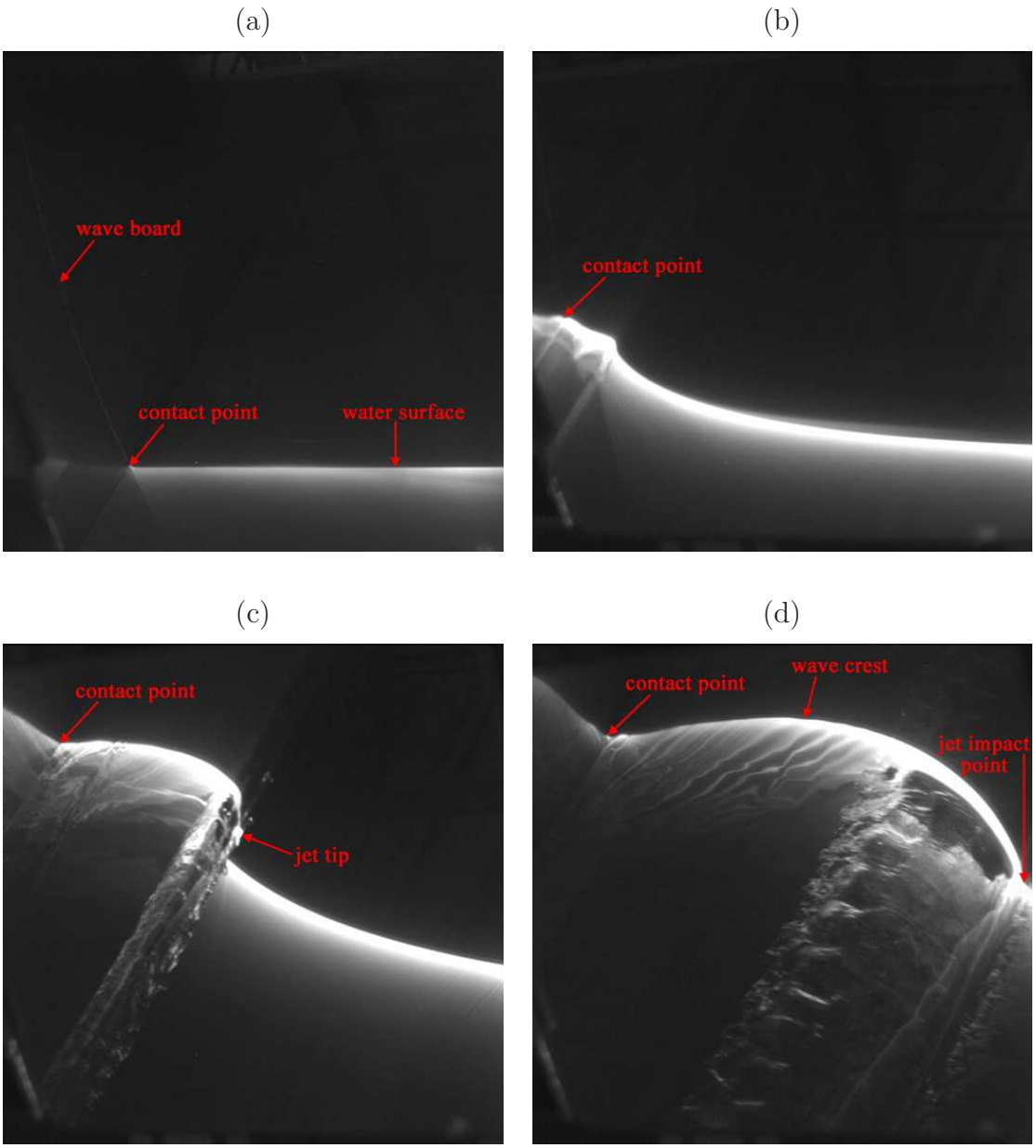

Figure 5.4: Wave formation process at four different times for equivalent ship speed of 27 knots. Time is (a) 0 s, (b) 0.371 s, (c) 0.586 s, (d) 0.738 s.

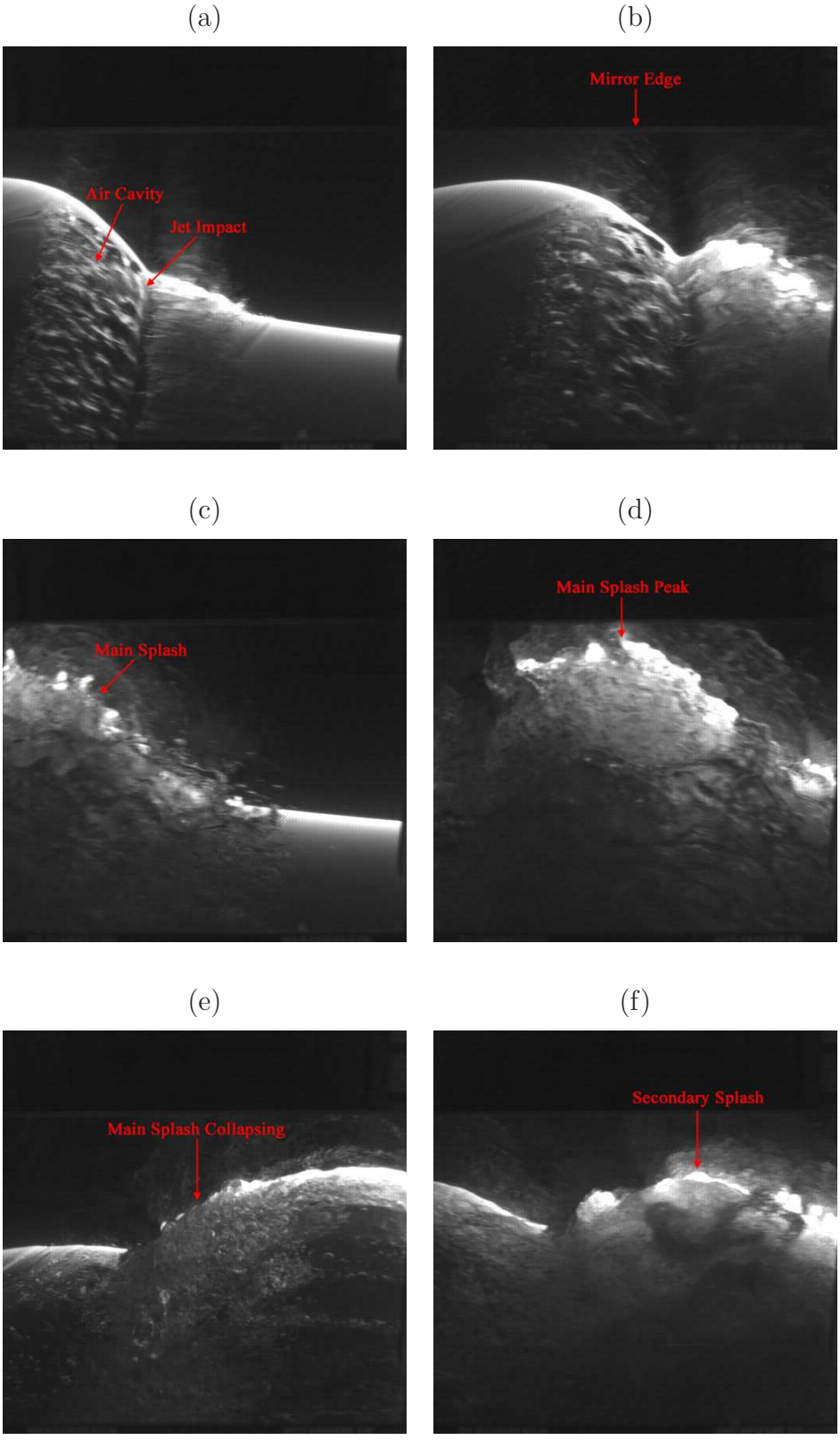

Figure 5.5: Splash formation process for equivalent ship speed of 27 knots. Time is (a) 0.816 s, (b) 0.926 s, (c) 1.020 s, (d) 1.160 s, (e) 1.430 s, (f) 1.445 s.

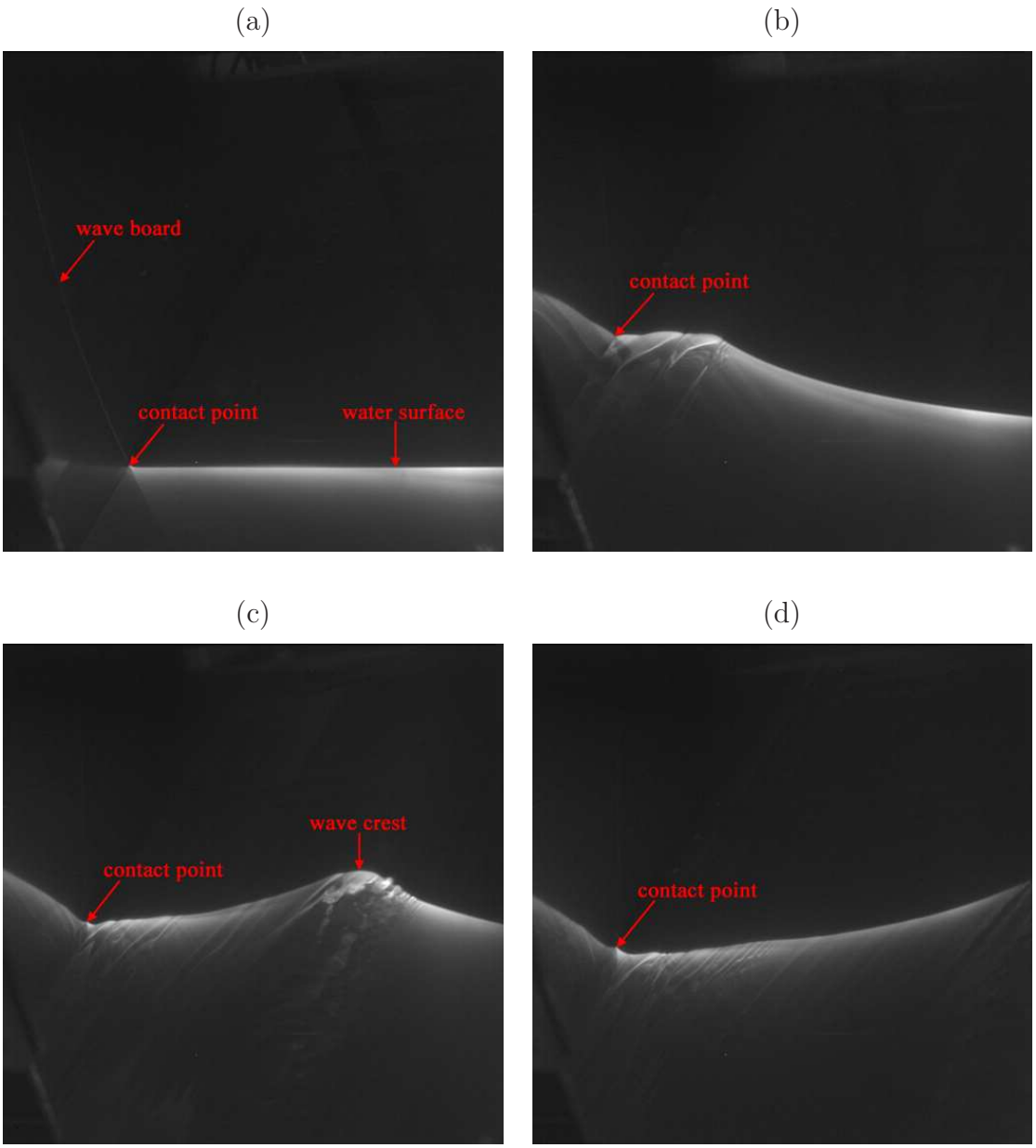

Figure 5.6: Wave formation process at four different times for equivalent ship speed of 16.5 knots. Time is (a) 0, (b) $0.16t_0$, (c) $0.23t_0$,(d) $0.31t_0$. t_0 is 3.393 s.

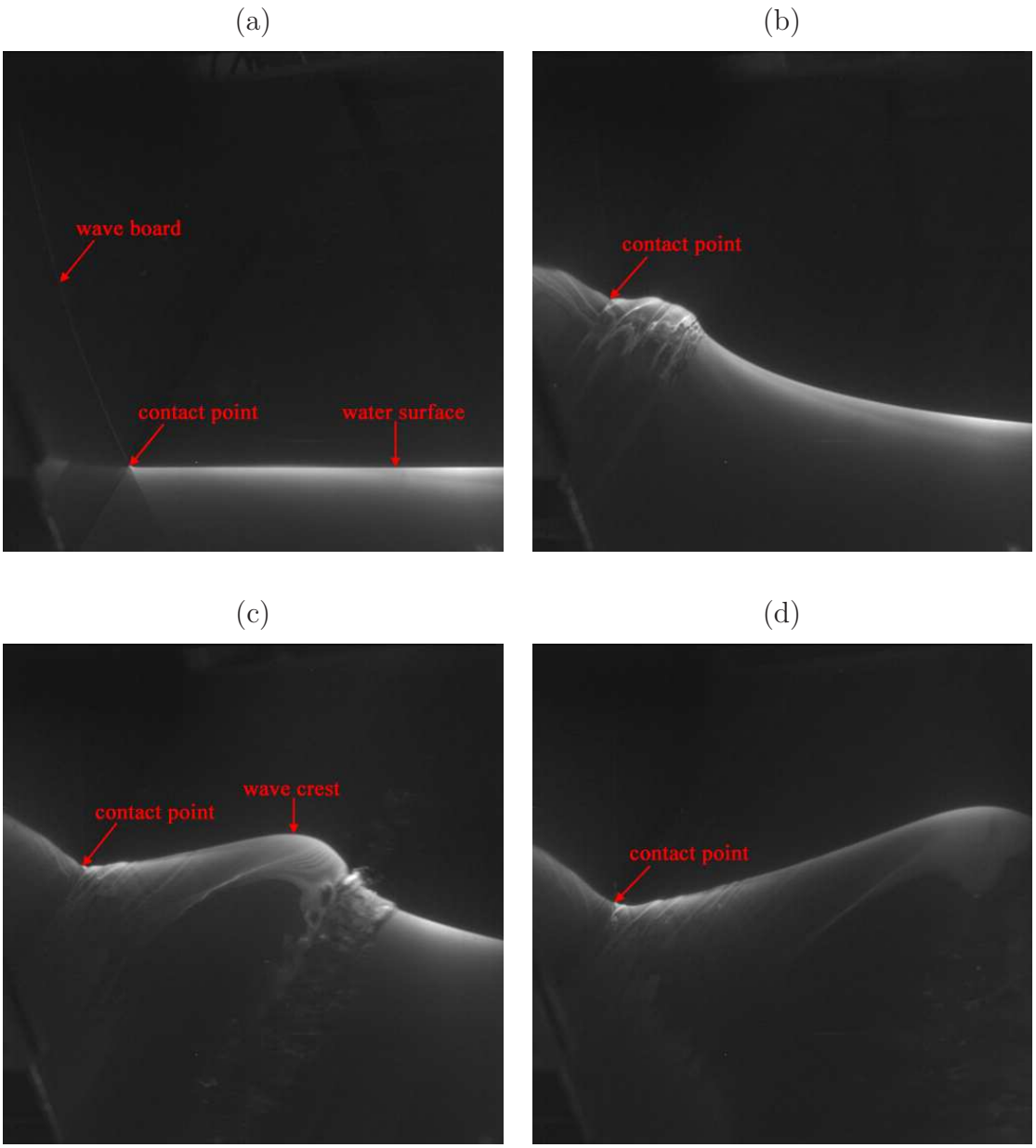

Figure 5.7: Wave formation process at four different times for equivalent ship speed of 20 knots. Time is (a) 0, (b) $0.16t_0$, (c) $0.23t_0$,(d) $0.31t_0$. t_0 is 2.8 s.

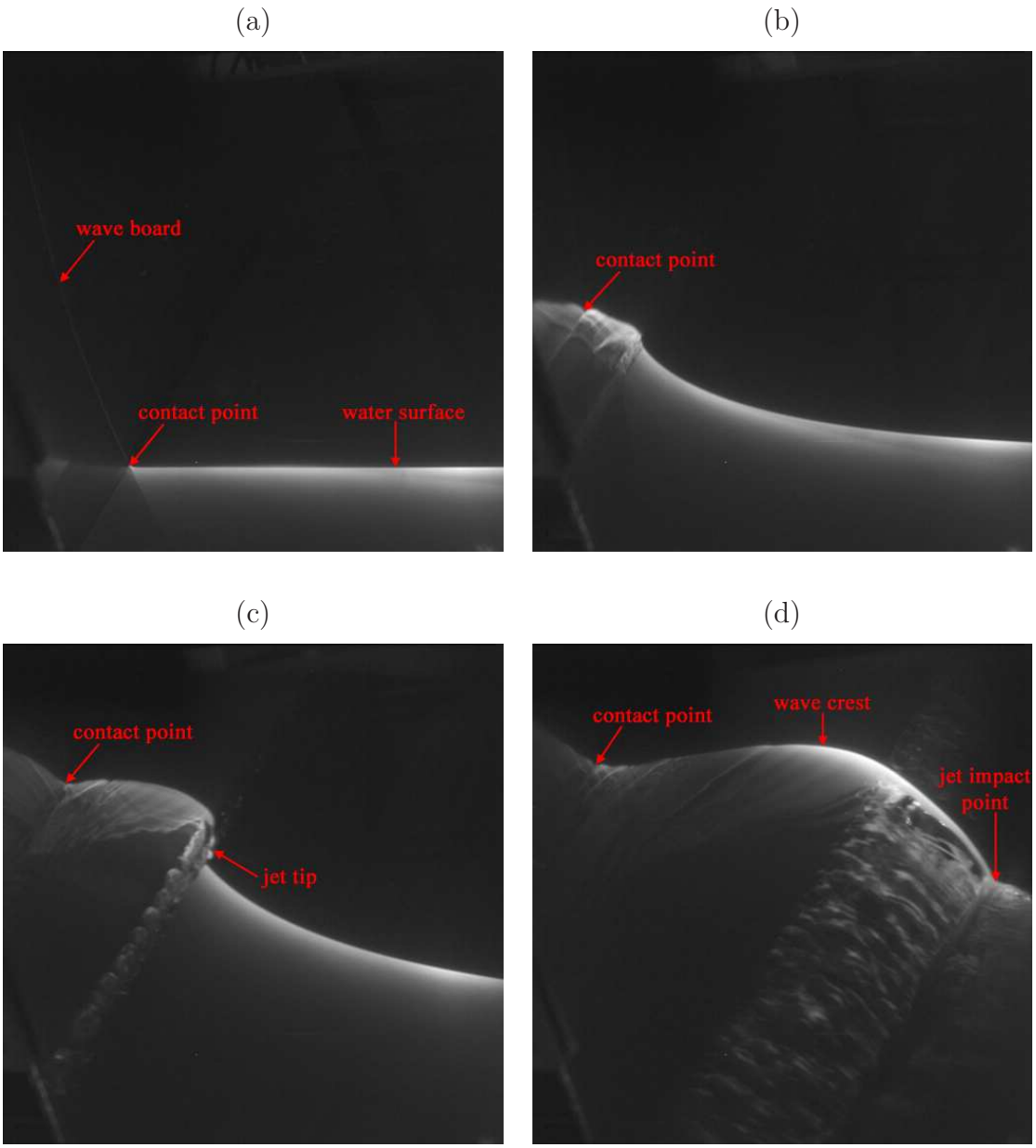

Figure 5.8: Wave formation process at four different times for equivalent ship speed of 25 knots. Time is (a) 0, (b) $0.16t_0$, (c) $0.23t_0$,(d) $0.31t_0$. t_0 is 2.24 s.

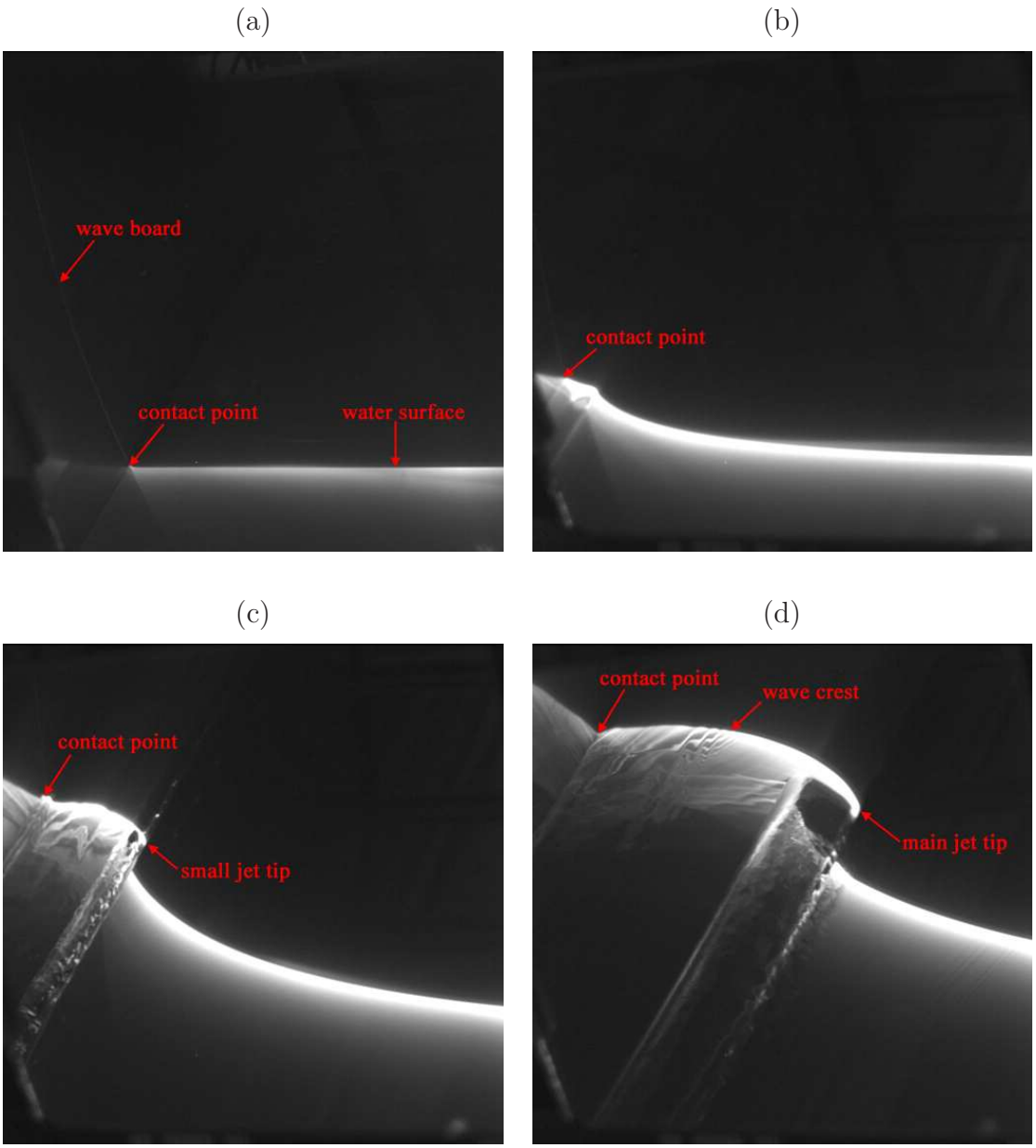

Figure 5.9: Wave formation process at four different times for equivalent ship speed of 27 knots. Time is (a) 0, (b) $0.16t_0$, (c) $0.23t_0$,(d) $0.31t_0$. t_0 is 2.074 s.

Detailed examination of the two higher speed cases indicates that there are two jet plunging events in each case–a small jet that forms and plunges early in the wave formation and a larger main jet that produces the main part of the air entrainment. The small and large jet can be seen near the plunge point in Figure 5.9(c)and (d), respectively. Both jets form and plunge during the evolution of the same wave crest. The cause of this multiple jet phenomenon is not known, but it is obviously related to intended or unintended details of the wave maker motion. The size and apparent strength of the main jet increases with the equivalent ship model speed.

Though the motion of the wave maker is highly two-dimensional, three dimensionality begins to appear in the free surface after the jet formation process is well underway. This three-dimensionality appears first as ripples on the underside of the jet and the jet tip. Later, after jet impact, the flow becomes fully turbulent and three dimensional drops and bubbles form, see Figure 5.3(c)and (d).

After the main jet impacts the front face of the wave, a splash region is formed ahead of the jet impact site, see Figure 5.5. Its likely that a portion of the water in the splash comes from the jet which bounces off the front face of the wave. No specific measurement has yet been made to quantify the source of the water in the splash. As will be shown in the later sections, the splash goes as high as the wave crest and becomes highly violent as the equivalent ship speed increases.

It is interesting to compare the sets of photographs taken at the same dimensional times (Figures 5.1 to 5.4) to those taken at the same dimensionless times (Figures 5.6 to 5.9) for the four equivalent ship speeds. From Figures 5.1 to 5.4 it can be seen that the phase of the wave development, for instance the point of jet

impact in the two higher speed cases or the initial spilling phase in the slower speed cases, occurs at roughly the same absolute time during the wave maker motion. This corresponds to different x locations on the equivalent 3D model hull. Equivalently, from Figures 5.6 to 5.9, it can be seen that at the same dimensionless times, which correspond to the same values of x in the 3D model hull, the wave is further evolved as the equivalent speed increases.

In order to make qualitative observations of the air entrainment process, movies were taken with the high speed camera looking under the free surface through the clear side walls of the tank. White light illumination was used for these movies. Figure 5.10 shows a sequence of four photographs extracted from the movie taken during the experiment with an equivalent ship speed of 25 knots. The most important features seen in the air-entrainment process are two clouds of bubbles under the free surface after the jet impacts the forward face of the wave and the splash forms. The cloud closest to the wave maker is due to air entrapped by the plunging jet and the other cloud results from the impact of the splash. The cloud from the splash moves away from the wave maker at a higher speed than the cloud due to the plunging jet; therefore, the separation between the clouds increases as time goes on. Also, the clouds appear to rotate in the clockwise direction. The width of the cloud from the jet impact and that from the splash are approximately 8.5 and 10.5 inches, respectively. The depths of the bottom edges of both clouds are approximately 11 inches. Note that these numbers are approximate; no exact measurements of the air entrainment process were made.

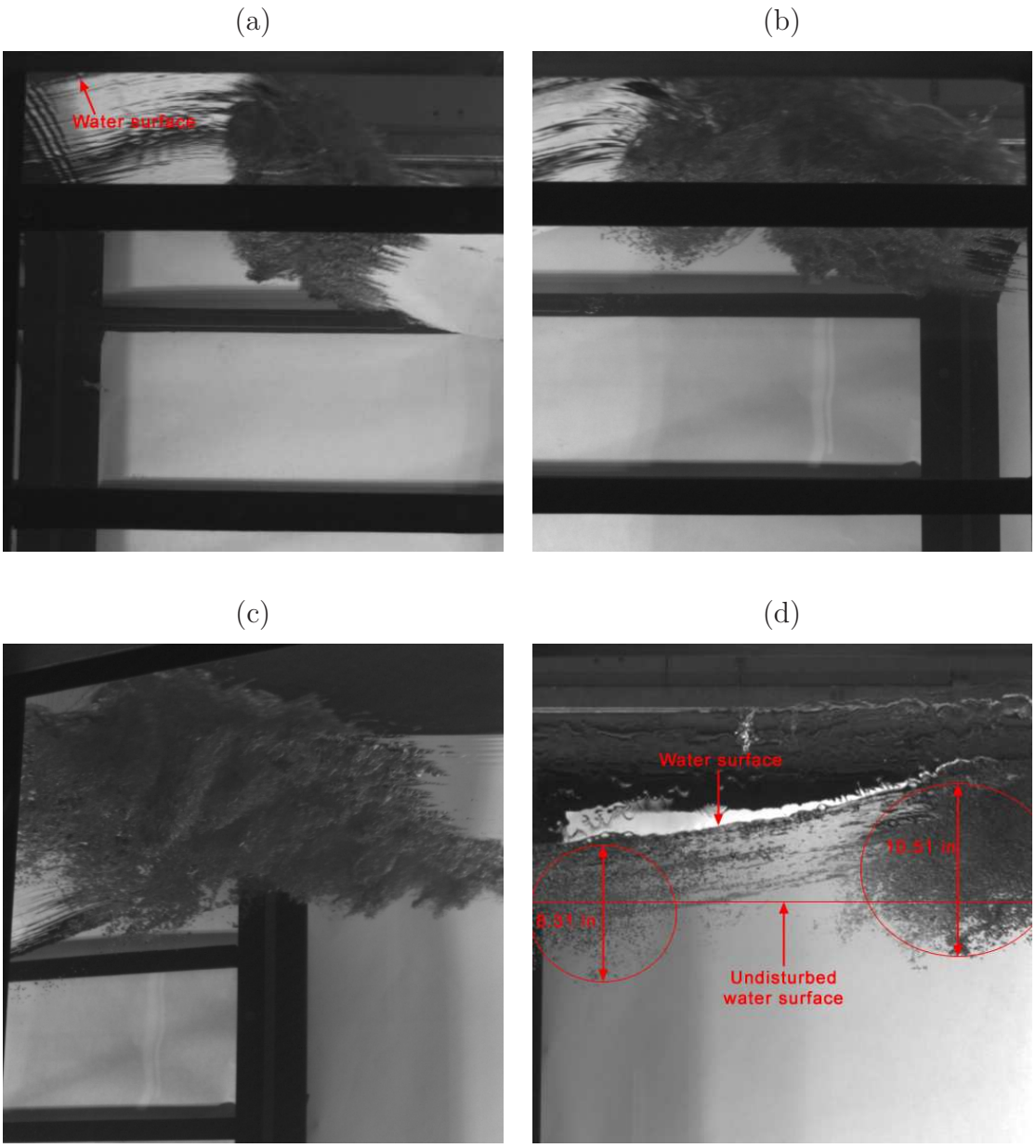

Figure 5.10: Air entrainment process at four different times for equivalent ship speed of 25 knots.

5.2 Measurements of the overall wave pattern around the ship simulator

As is explained in detail in the previous chapter, the water surface profile histories were measured with two high-speed digital movie cameras that were mounted on the instrument carriage. The cameras viewed the intersection of the laser light sheet (also fixed to the carriage) and the water surface at the center plane of the tank. Measurements were made over the entire domain of the wave motion up to the time of passage of the stern of the equivalent 3D ship model. This covers a distance out to approximately 1.5 beam widths from the centerline of the equivalent 3D model. Interestingly, this width compares well to the width of the breaking zones of full scale ships as seen in Figure 5.11.

The wave patterns for the four equivalent ship speeds are shown in Figures 5.12, 5.13, 5.14, and 5.15. In these figures, the horizontal axis is the distance (y) from the midplane of the equivalent ship model normalized by the beam ($b = 2.82$ m) and the vertical axis is the height (z) of each point on the water surface normalized by the draft ($d = 0.9144$ m). The plots cover a distance of about 1.4 beams horizontally. In these plots, there are black and red lines. Black lines represent the data from images taken by camera A, while red lines are from the images taken by camera B, see Figure 3.40. There are four sets of black and red lines representing four different measurement zones on each plot. The data from both cameras from all zones were patched together to give the wave pattern around the ship model. In all cases, the time between consecutive profiles is 0.078 s, representing every 20^{th} frame of the

Figure 5.11: A typical wave pattern around a real ship.

images taken by each camera, which recorded 256 frames per second.

Figure 5.12 shows the wave pattern around the wave maker at the equivalent ship speed of 16.5 knots. At the early stages of the wave maker motion, most of the water surface is horizontal. The first motion of the water surface is a rapid rise next to the wave board. At this stage, the water surface away from the wave board does not move. As time goes on, the water moves away from the equivalent ship model centerline and the water surface far away from the wave board starts rising. As seen in Figure 5.12, a secondary wave forms between the first wave crest and the wave board at a point about $0.25b$ away from the ship centerline. This wave is much smaller than the main wave, which grows as high as $0.2d$ from the undisturbed water surface. At this ship model speed, the amplitude of the secondary wave reaches only about $0.02d$. This wave never grows large enough to break.

At the ship model speed of 20 knots, the wave breaking becomes more violent, see Figure 5.13. The wave is steep with a crest height as high as $0.25d$. A small jet forms of the forward face of the crest and its impact initiates a spilling breaking process. Figure 5.14 shows the wave pattern around the simulated ship model at an equivalent ship speed of 25 knots. At this speed, the wave becomes steeper and gets as high as $0.36d$. Figure 5.15 shows the wave pattern around the simulated ship model at the equivalent ship speed of 27 knots. At this speed the breaking appears more violent and the crest height reaches $0.38d$, the highest value of this test series.

Each set of experiments was conducted three times to confirm the repeatability of the measurement technique from run to run. These three profiles are plotted in Figure 5.16 and 5.17 for the cases with equivalent ship speeds of 20 knots and

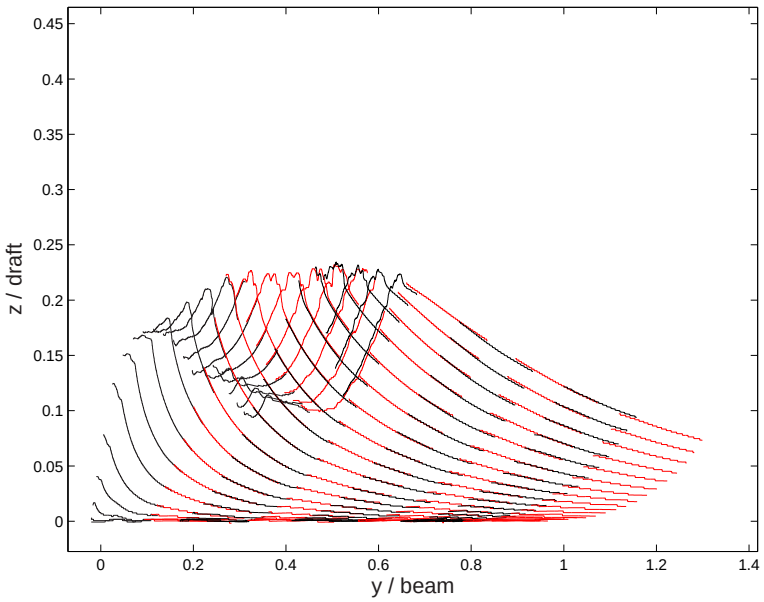

Figure 5.12: Profile histories of the bow wave generated by 2D+T wave maker at equivalent ship speed of 16.5 knots; Time interval between the profiles is 0.078 s; beam(b)=2.82 m and draft(d)=.914 m.

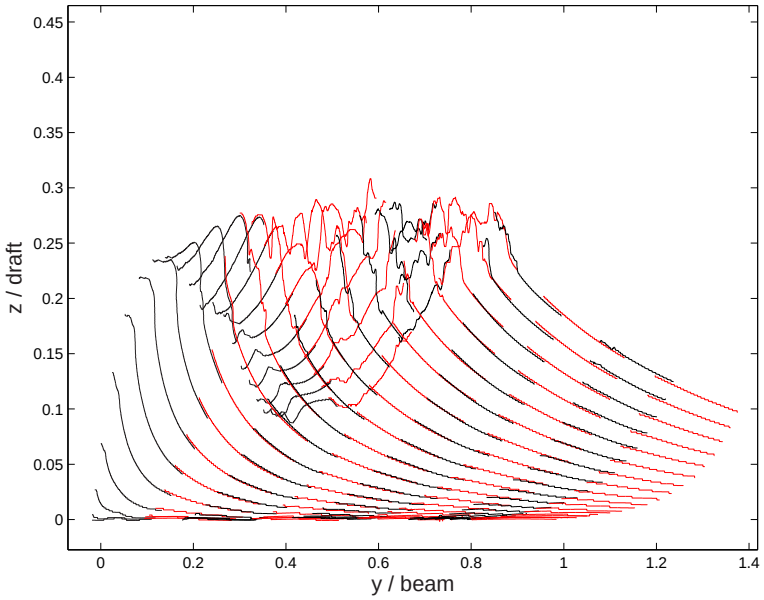

Figure 5.13: Profile histories of the bow wave generated by 2D+T wave maker at equivalent ship speed of 20.0 knots; Time interval between the profiles is 0.078 s; beam(b)=2.82 m and draft(d)=.914 m.

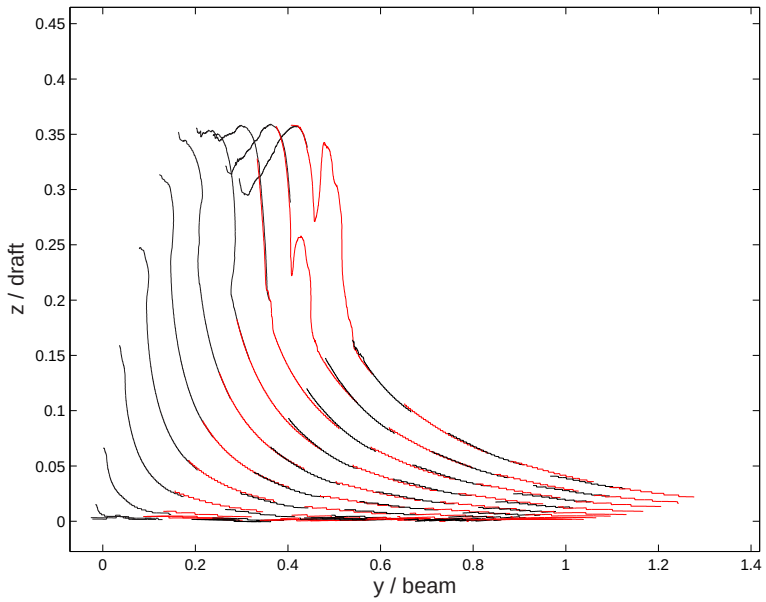

Figure 5.14: Profile histories of the bow wave generated by 2D+T wave maker at equivalent ship speed of 25.0 knots; Time interval between the profiles is 0.078 s; beam(b)=2.82 m and draft(d)=.914 m.

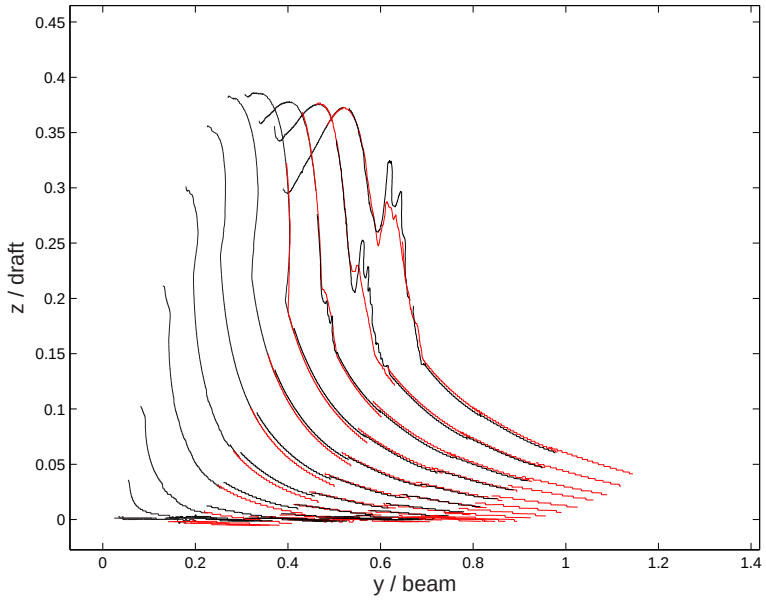

Figure 5.15: Profile histories of the bow wave generated by 2D+T wave maker at equivalent ship speed of 27.0 knots; Time interval between the profiles is 0.078 s; beam(b)=2.82 m and draft(d)=.914 m.

27 knots, respectively. These profiles are from zones 1 and 2 only. In addition to the curves from individual runs, curves obtained by averaging the data from the three runs are also presented. These average curves were obtained with a nearest neighbor method. In this averaging method, the coordinates of a point on one of the three curves is selected and averaged with the coordinates of the closest points on the other two curves. As can be seen in the figures, in regions before the plunging jet impact or away from the ensuing turbulent impact site and splash, the three realizations of the wave profile are nearly identical and nearly equal to the average profile. This shows that the wave maker produces highly repeatable motions from run to run. In the impact and splash regions turbulence is created and this adds randomness to the surface profile shapes. Thus, there is a larger run to run variation in these regions.

The run to run RMS values about the mean curve were also plotted to show a quantitative measure of the variation of the wave profiles from run to run, see Figures 5.18 and 5.19 for the two equivalent ship speeds of 20 knots and 27 knots, respectively. Smaller RMS values are seen over the non-turbulent part of the wave profiles while larger RMS values are seen in the jet impact and splash regions.

5.3 Comparison of the 2D+T with the 5415 ship model results

The 2D+T wave maker simulates the bow wave generation of the 5415 model built at the Naval Surface Warfare Center, Carderock. In this section, some features of the wave systems of the two models are compared and contrasted. However, the

(a)

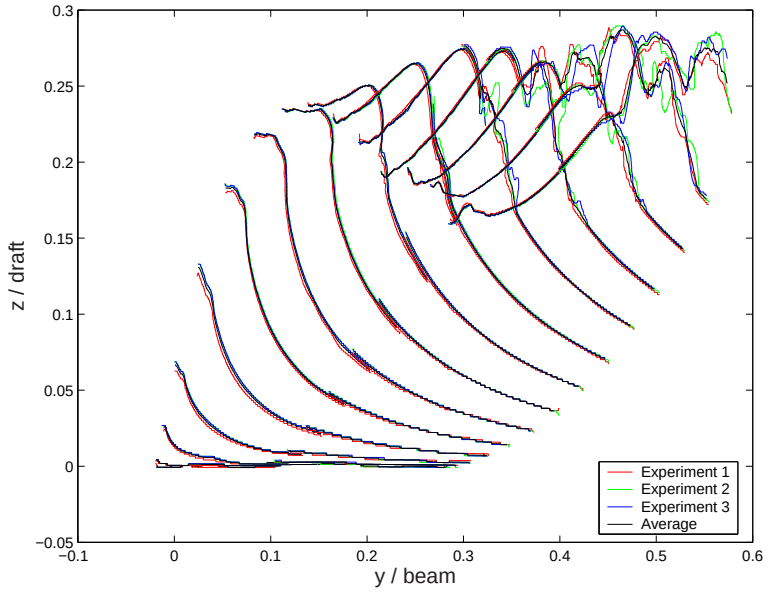

(b)

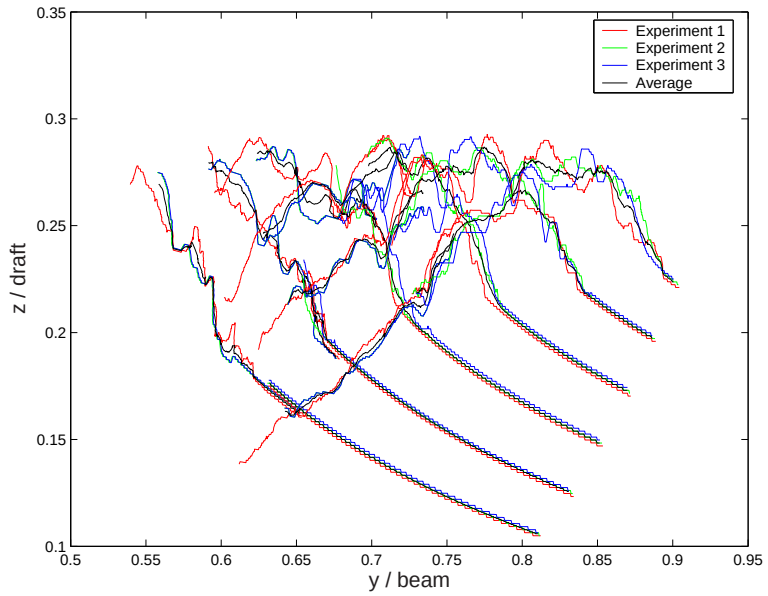

Figure 5.16: Profile histories of the bow wave generated by the 2D+T wave maker at equivalent ship speed of 27.0 knots from three different runs along with the averaged profile from (a) zone 1 (b) zone 2; Time interval between the profiles is 0.078 s; beam(b)=2.82 m and draft(d)=.914 m.

(a)

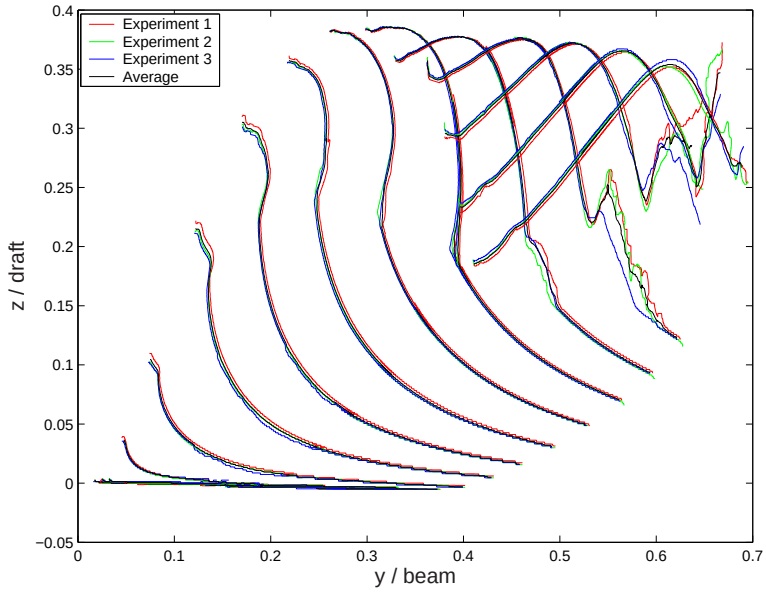

(b)

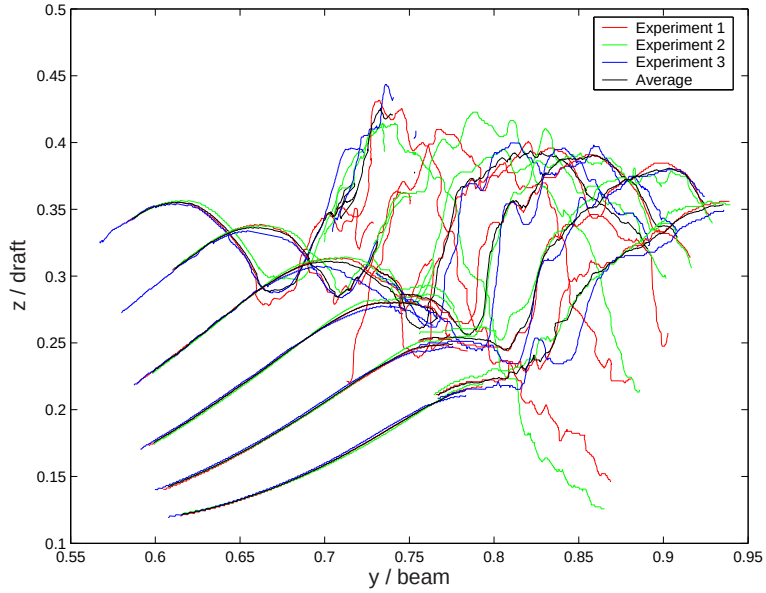

Figure 5.17: Profile histories of the bow wave generated by 2D+T wave maker at equivalent ship speed of 27.0 knots from three different runs along with the averaged profile from (a) zone 1 (b) zone 2; Time interval between the profiles is 0.078 s; beam(b)=2.82 m and draft(d)=.914 m.

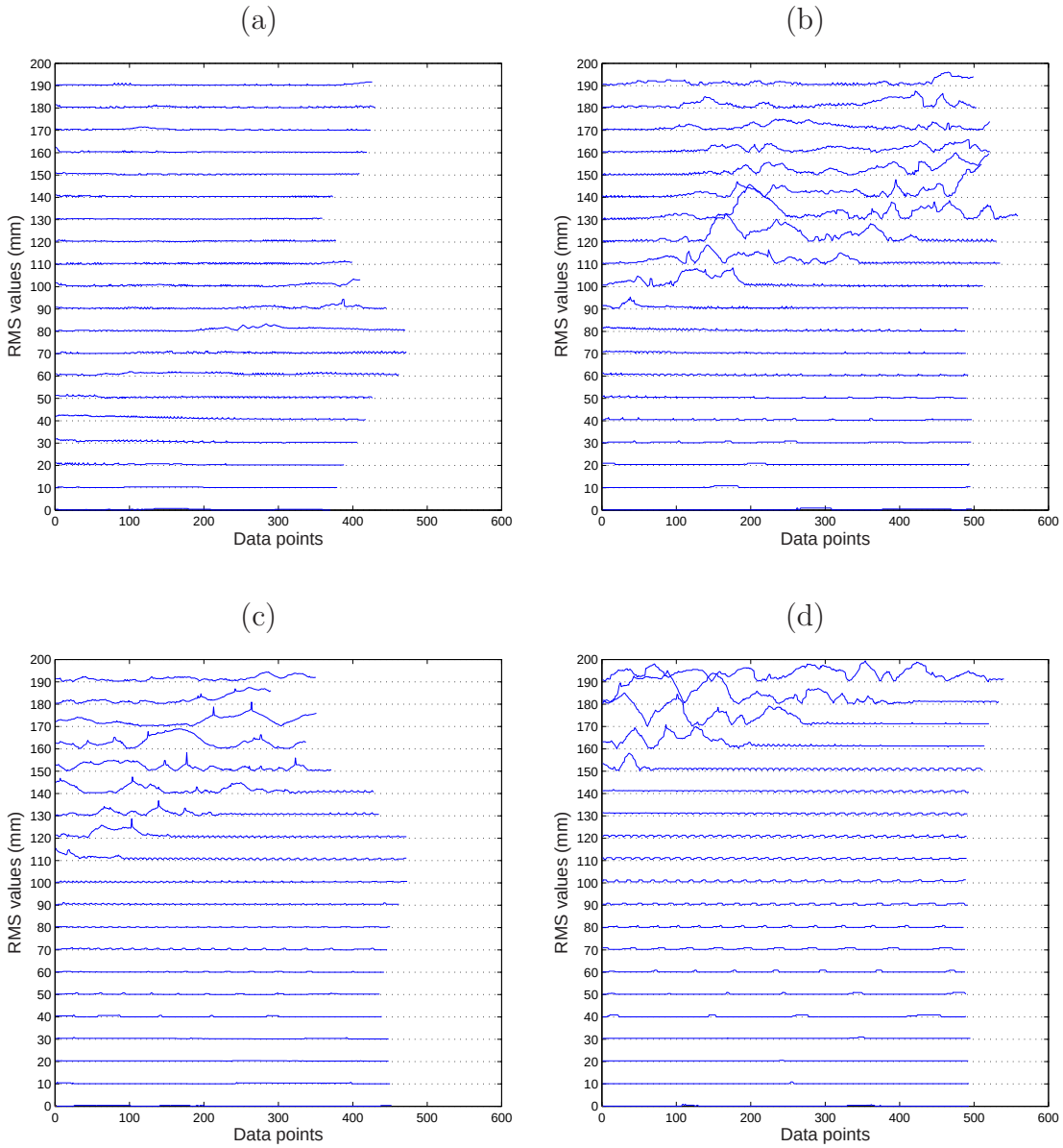

Figure 5.18: Curves of RMS surface fluctuations about the mean wave profiles from three different runs under the same conditions at different times of the wave formation and breaking process for an equivalent ship speed of 20 knots. Horizontal axis represents the data point along each wave profile. Each curve was elevated by 10 mm on the vertical axis for clarity. Curves are from (a) zone 1, camera A, (b) zone 1, camera B, (c) zone 2, camera A, and (a) zone 2, camera B.

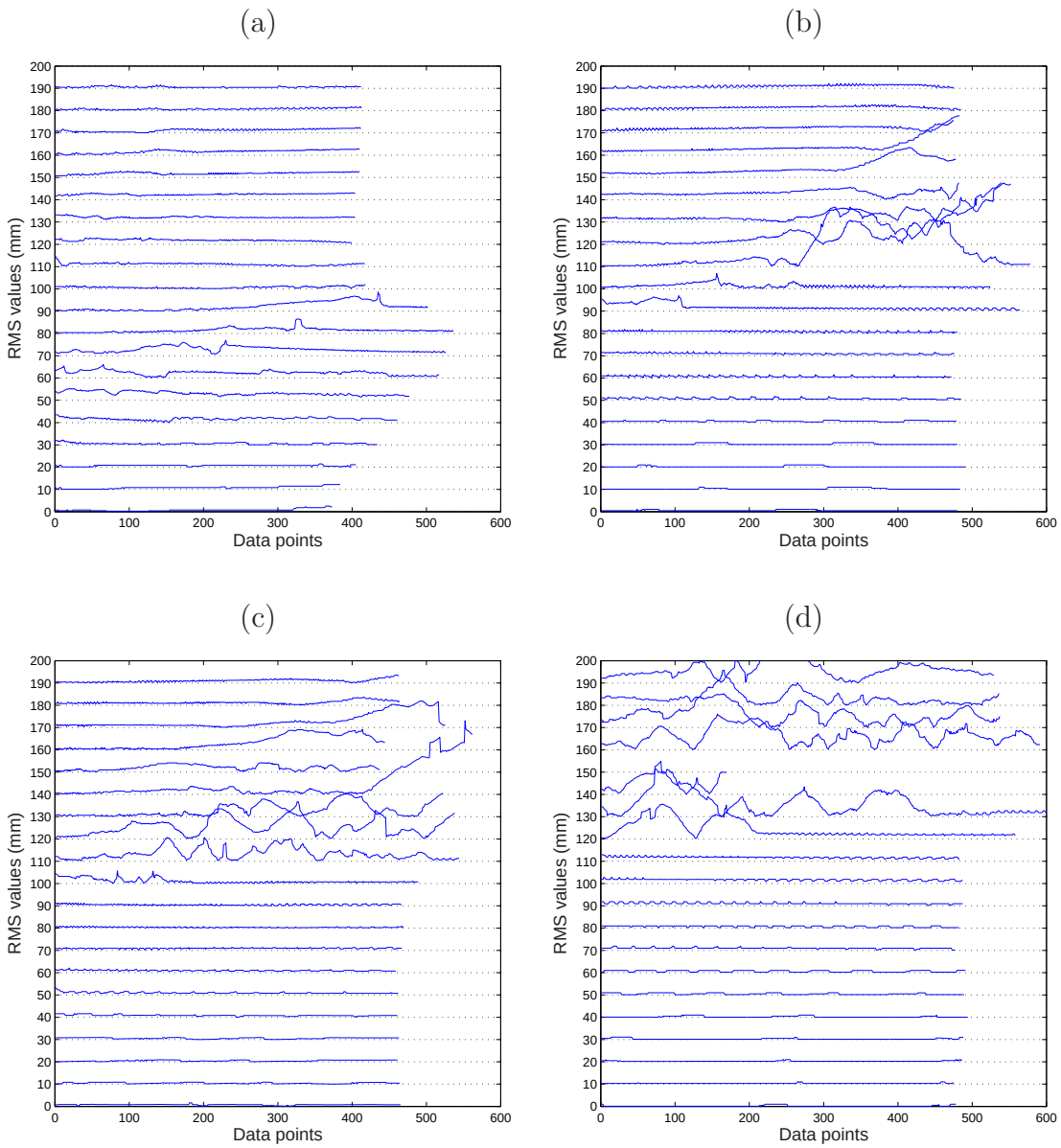

Figure 5.19: Curves of RMS surface fluctuations about the mean wave profiles from three different runs under the same conditions at different times of the wave formation and breaking process for an equivalent ship speed of 27 knots. Horizontal axis represents the data point along each wave profile. Each curve was elevated by 10 mm on the vertical axis for clarity. Curves are from (a) zone 1, camera A, (b) zone 1, camera B, (c) zone 2, camera A, and (a) zone 2, camera B.

reader is reminded that the 5415 model has a large sonar dome in the bow region and this feature of the hull is not simulated by the 2D+T wave maker. Since it is well known that large submerged structures at the bows of ships modify the wave systems, one should not expect excellent quantitative agreement between the two wave patterns.

Figure 5.20 shows sample photographs of the waves around the bow of the 5415 model at equivalent full scale ship speeds of 20 and 30 knots. At each model speed, one photograph taken at different times is included to show the temporal variation of the wave pattern due to turbulence. Key features of the wave pattern are labeled to facilitate the following discussion. In the low speed (20 knots) case, a fairly strong spilling breaker is found at the bow. A little further downstream, a secondary non breaking wave crest can be seen. Both the spilling breaking bow wave and the secondary wave also are found in the 2D+T wave field at the 20-knot speed, see Figure 5.2. The 30-knot case for the 5415 model can be compared to the 27-knot case for the 2D+T wave maker. In both the 5415 and 2D+T wave systems (see Figure 5.4 for the 2D+T waves), a strong plunging breaker is found along with a violent splash up after the jet impact. In both cases, clouds of air bubbles are entrained under the free surface at the crest and the splash region. These bubbles can be seen as they come to the surface in the photographs in in Figure 5.20 and the from the above surface view in Figure 5.4. The entrainment region under the crest is seen to be smaller than that under the splash in both studies. Also of interest are the bubble pictures for the 25-knot case for the 2D+T wave maker in Figure 5.10. These photographs show that the region of bubbles under the crest separates from

(a)

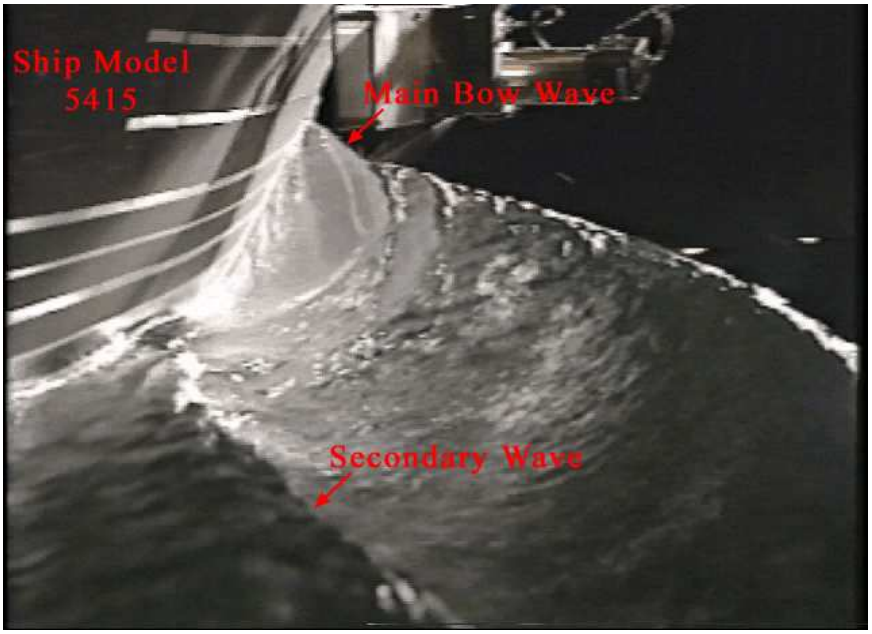

(b)

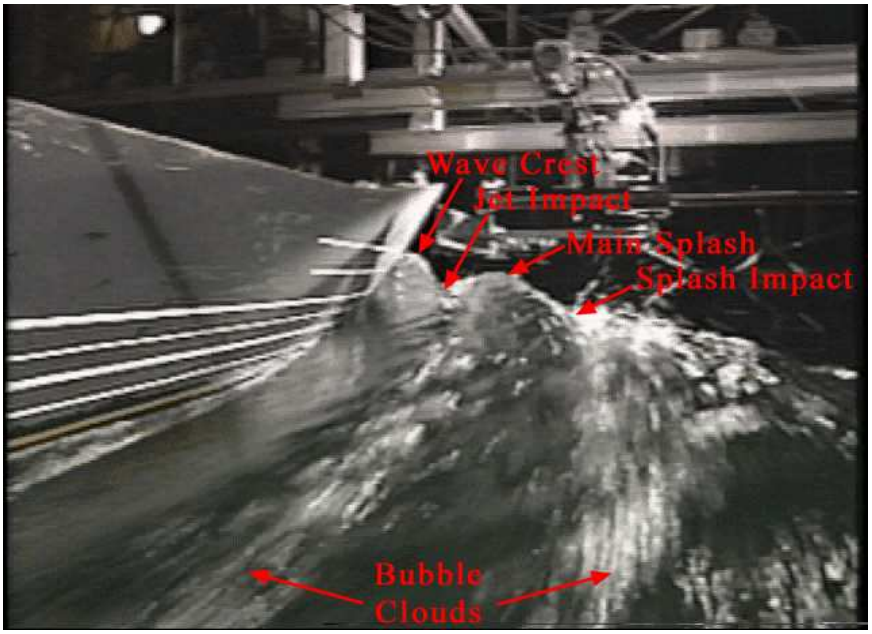

Figure 5.20: Wave formation process in the 3D model 5415 at full-scale speeds of (a) 20 knots and (b) 30 knots.

the region under the splash as time proceeds (see above discussion). This behavior is also obvious from the bubble trails in the free surface photographs of the 5415 wave pattern at the 30-knot speed.

Plots of the contact line height versus streamwise position for the 5415 model were found on the Naval Surface Warfare Center's web site. The contact line data for the 2D+T wave maker was obtained as described in the following subsection. A comparison of these two data sets (full scale ship speeds of 20 and 30 knots for the 5415 model and the four values mentioned perviously for the 2D+T wave maker) is given in Figure 5.21. Both sets of data were normalized by the appropriate ship model length for streamwise positions and draft for the water surface height. As mentioned previously the equivalent length of the 2D+T model is $L = 21.03$ m.

The data for the 5415 and 2D+T models have the same trend; however, non-dimensional surface heights for the 5415 model are considerably higher for the 20-knot and 30-knot speeds when compared to the data for the 20-knot and 27-knot speeds for the 2D+T model. These differences may be caused by the removal of the bulb in the 2D+T model, the changes in the 2D+T model shape at the stem as discussed in the previous chapter, or the 2D+T approximation itself.

5.4 Geometric properties of 2D+T bow waves

5.4.1 Water contact line with the wave board

The water contact lines were obtained for four different equivalent ship speeds in the 2D+T experiments. In these experiments, the contact points are first ob-

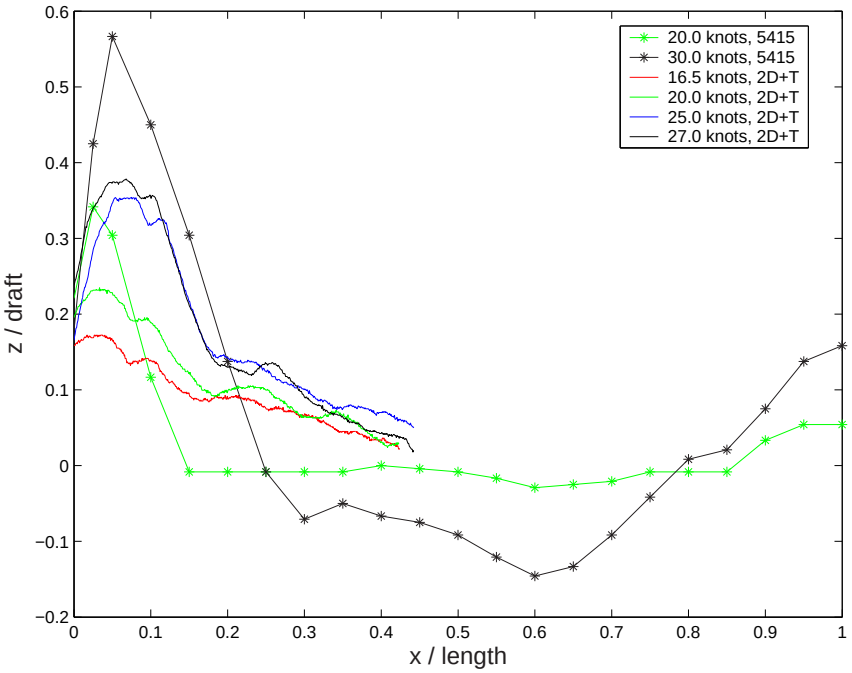

Figure 5.21: The height of the water contact line of the 2D+T measurements at various equivalent ship speeds along with the data of the 5415 model; length(L)=21.03 m and draft(d)=.914 m for 2D+T; length(L)=5.72 m and draft(d)=.305 m for 5415 model.

tained at different times and then the time coordinate is transferred into a spatial into streamwise distance using the 2D+T conversion $x = Ut$. The variables are normalized, unless otherwise noted. The streamwise distance is normalized by the length of the ship model ($L = 21.03$ m), transverse direction distance by the beam of the ship ($b = 2.82$ m), and the water surface height by the the draft of the model ($d = .9144$ m). Also, the height of the contact point is measured from the undisturbed water surface in all cases.

The projection of the contact lines on to the mid-plane of the equivalent ship model (along the steamwise direction) is shown in Figure 5.22. As seen in the figure, the water surface rises up to 15, 22, 33, and 36 percent of the draft for equivalent ship speeds of 16.5, 20, 25, 27 knots, respectively. Further downstream from the peak in the contact height, the water surface falls as the bow wave detaches from the ship hull. The main part of the wave maker energy is probably discharged by this point. However, the contact line rises again as the wave board expansion continues (equivalent to the growth in ship model cross sectional area). This second rise in the contact line height is seen in all four equivalent ship speed cases, see Figure 5.22. The reason the rise is very small, could be related to the slow change in ship model cross-section area as it approaches mid-ship.

The three-dimensional locations of the maximum height of the contact point (peak of the contact line) in equivalent ship model coordinates (x-streamwise, y-transverse and z-vertical, see Chapter 1) are plotted against the Froude number in Figure 5.23. As seen in the figure, the location of the peak of the contact line in the streamwise direction is a strong function of the Froude number. At the same

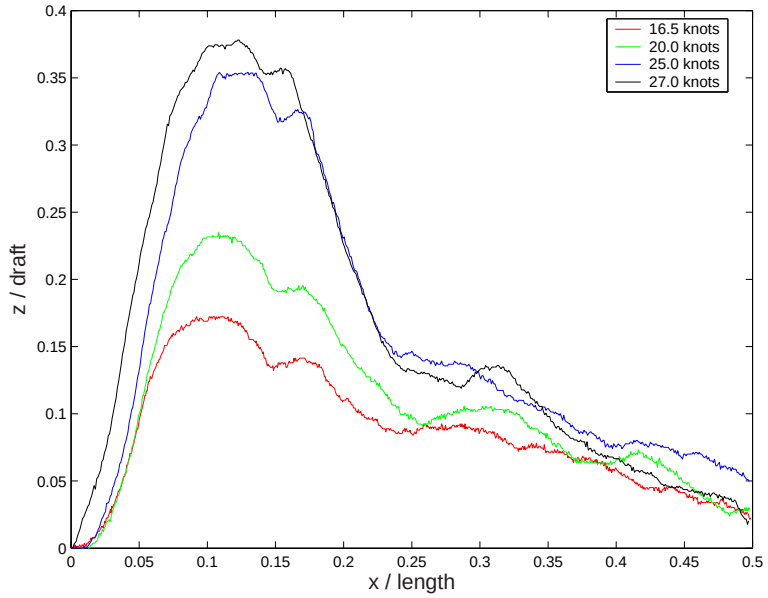

Figure 5.22: The height of the water contact line of the bow wave generated by 2D+T wave maker at various equivalent ship speeds in xz-plane; length(L)=21.03 m and draft(d)=.914 m.

time, the height and transverse location of the peak is less effected by the Froude number. The results show that, at the lowest ship speed, the y and z values of the position of the maximum contact point height are about equal.

Figure 5.24 shows the horizontal velocity of the contact point versus time at various equivalent ship speeds. In this figure, the horizontal axis is time (equivalent to streamwise location from the stem of a ship model) normalized by the time at which the wave maker completes motion, t_0, and the vertical axis is the horizontal velocity of the contact point normalized by the maximum speed of the wave maker's top drive channel. The values of t_0 are 3.393, 2.8, 2.24, and 2.074 s and the maximum top channel speeds are 0.82, 0.996, 1.24, and 1.34 m/s for equivalent ship speeds of 16.5, 20, 25, and 27 knots. Also shown in the figure are curves of the horizontal

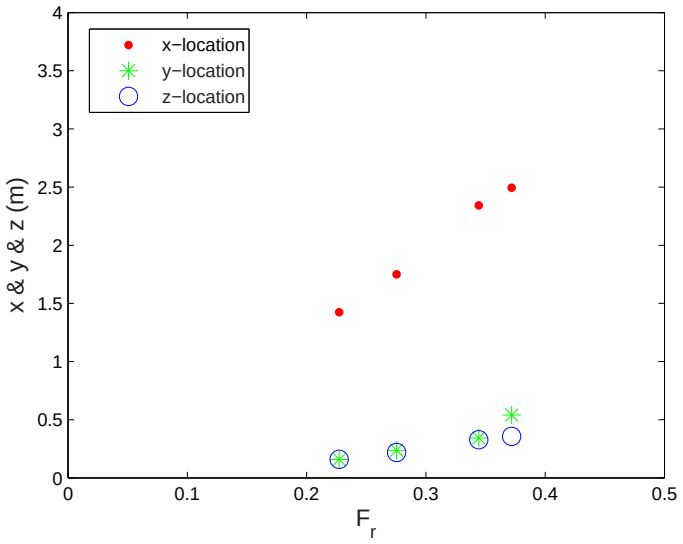

Figure 5.23: Three-dimensional location of the peak of the contact line at various Froude numbers ($F_r = u_m/\sqrt{gL_m}$, where g is gravity, u_m and L_m are the speed and length of the equivalent 3D ship model).

velocity of the top drive channel for each equivalent ship speed.

As can be seen in Figure 5.24, the contact-point velocity distribution is quite noisy in spite of the fact that the curves of y and z positions versus time are very smooth. The main cause of this noise is the high spatial frequency of our data. Therefore, we decided to remove the high-frequency information contained in the position data before taking the derivative.

In order to smooth the data, for each point in the data set a second order polynomial was fitted to a set of points clustered around the point of interest using a least squares algorithm. The slope of the polynomial at that center point was taken as the velocity. This calculation was repeated for each point in the data set. This curve fitting process removed most of the high-frequency noise. The remaining

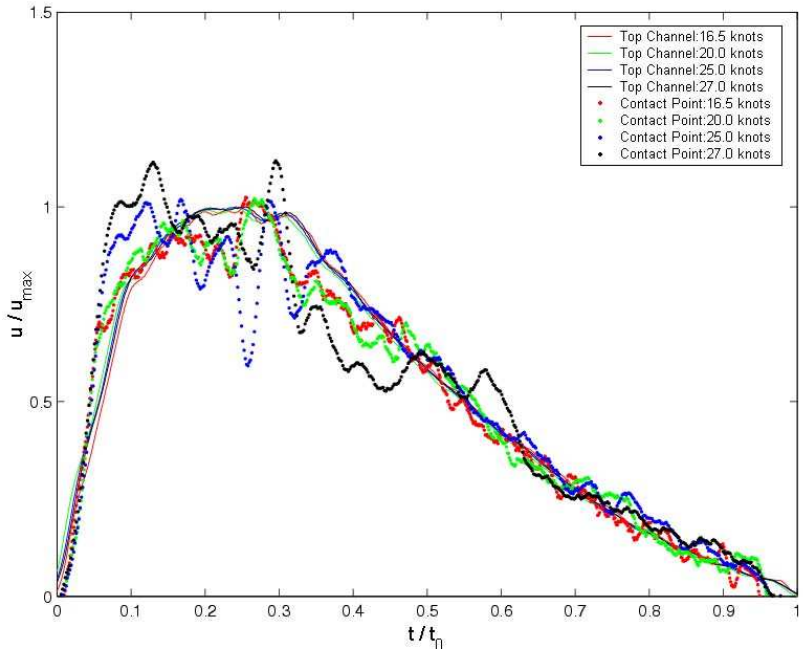

Figure 5.24: Horizontal (y-component) velocity of the contact point at various equivalent ship speeds as a function of time; t_0 = 3.393, 2.8, 2.24, and 2.074 s and u_{max} = 0.82, 0.996, 1.24, and 1.34 m/s for equivalent ship speeds of 16.5, 20, 25, and 27 knots.

noise level in the data will be discussed in the next section where the wave crest results are discussed.

When the wave maker is at rest, the undisturbed water surface is 6 inches below the wave maker top drive channel. During the wave maker motion, the water surface rises and soon passes the height of the top drive channel. At this point, the y-component of the velocity of the contact point is equal the velocity of the top drive channel. This point is seen in Figure 5.24 as an intersection of the contact-point and top-drive-channel curves for each equivalent ship speed. This intersection occurs at times less than $0.1t_0$ for all cases.

5.4.2 Wave crest properties

Wave crest properties are important because they lead to the formation of the plunging jet and the subsequent air entrainment process. Figure 5.25 shows the trajectories (z/d versus y/b, see Figure 1.3) of the highest point on the water surface profile for the four equivalent ship speeds. In all cases, the trajectories rise rapidly at small y/b and then level off or at least rise more slowly. The data shows that the maximum height of the crest increases with increasing equivalent ship speed. The physical meaning of these curves requires some explanation. Initially, the highest point on the water surface is the contact point while later in the wave maker motion the wave crest propagates away from the wave board and the highest point moves to the wave crest. These transitions in the location of the highest point on the water surface can be seen in the figure as obvious discontinuities in the curves at positions

ranging from $0.1y_{crest}/b$ for the lowest equivalent ship speed to $0.2y_{crest}/b$ for the highest equivalent ship speed. The reason for this gap is that as the highest point goes from the contact point to the wave crest, the water surface in that region is flat and the y-coordinate of the highest point is difficult to locate. The curves end when the splash forms; the splash eventually becomes the highest point on the profile but this data is not shown in the figure.

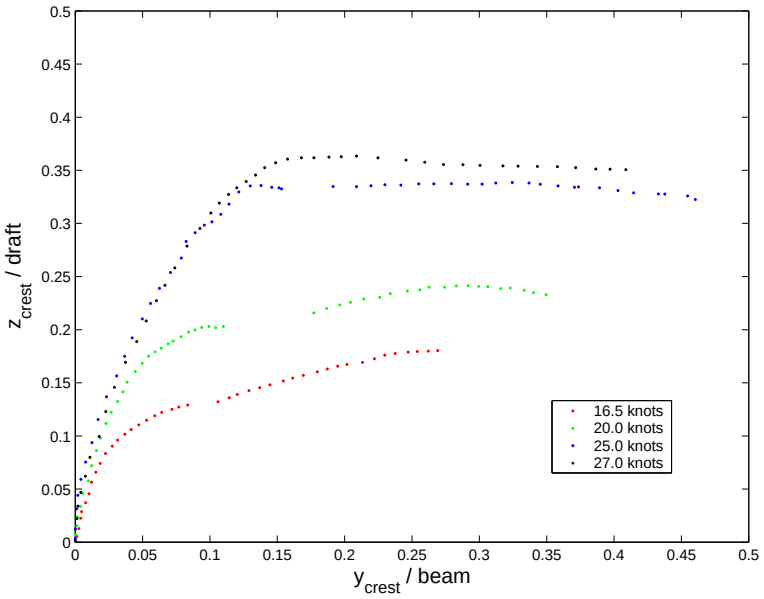

Figure 5.25: Trajectories in the yz-plane of the highest point on the wave profile at various equivalent ship speeds; beam(b)=2.82 m and draft(d)=.914 m.

Figure 5.26 shows trajectories of the wave crest at various equivalent ship speeds in the xy-plane. This is actually the plan view of the waves about the equivalent 3D ship model ($x = Ut$ and $y = 0$ is the midplane of the ship). The horizontal axis (y/b) shows the distance of the wave crest from the keel (equivalent to the ship center line) and the vertical axis represents the streamwise distance along the equivalent ship model (x/L). The 2D+T calculations of Tulin and Wu

(1996) indicate that for normal ship slenderness ratios (beam/length) of 0.1-0.2, the divergent bow wave crests tend to be straight. In our experiments the slenderness of the equivalent ship is 0.13 (2.82/21.03). The crest trajectories shown in Figure 5.26 are straight lines in agreement with the earlier calculations.

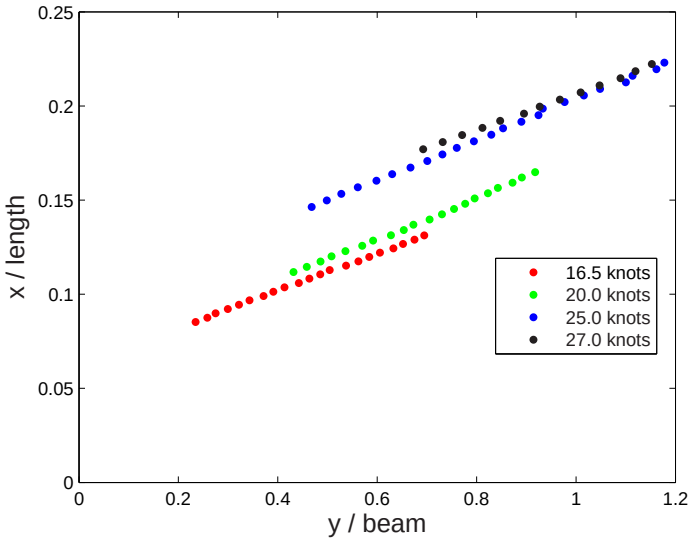

Figure 5.26: Trajectories in xy-plane of the crest of the bow wave generated by 2D+T wave maker at various equivalent ship speeds; length(L)=21.03 m and beam(d)=2.82 m.

The location of the maximum height of the wave crest in the streamwise and transverse directions along with the maximum wave crest height were plotted against the Froude number in Figure 5.27. For clarity in the plot, the vertical axis has dimensions of meters. As can be seen in the figure, the maximum height of the bow wave increases monotonically with Froude number. The location of the maximum height of the wave increases in x (the streamwise direction) and y (the transverse direction) as the Froude number increases up to 0.34 but then at the highest Froude

number the x and y values decrease. These decreases seem logical since the x and y locations of the maximum height are not expected to increase indefinitely as the Froude (ship speed) tends to infinity. As the ship speed increases, the energy put into the wave formation process increases and the wave becomes strongly nonlinear and breaks. Therefore, not getting a monotonically increasing function for the streamwise and transverse location of the maximum height is not surprising. Later in this chapter, in the subsection on scaling, we will discuss the effects of the Froude number on the maximum height of the wave crest as well as on the location of the plunging jet impact point.

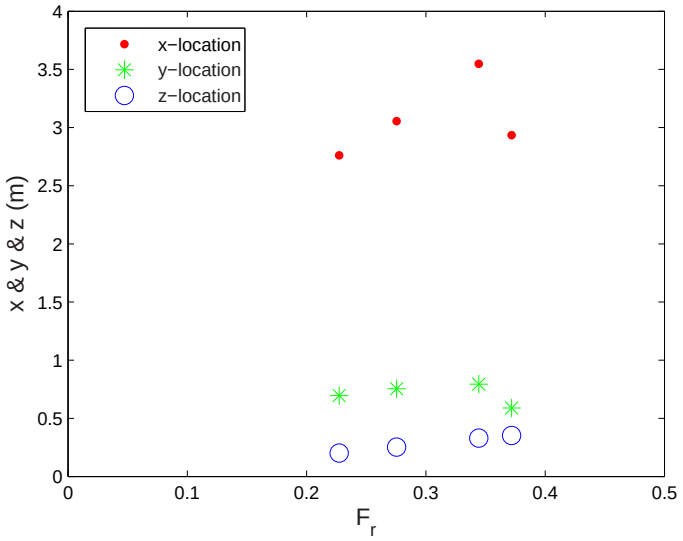

Figure 5.27: Three-dimensional location of the maximum height of the wave crest at various Froude numbers ($F_r = u_m/\sqrt{gL_m}$, where g is gravity, u_m and L_m are the speed and length of the equivalent 3D ship model).

Figure 5.28 and 5.29 show the horizontal and vertical velocities of the highest point on the wave profile for the four equivalent ship speeds as a function of time.

Also shown in Figure 5.28 is the speed of the top drive channel of the wave maker. All velocities are normalized by the maximum velocity of the top drive channel (u_{max} = 0.82, 0.996, 1.24, and 1.34 m/s for equivalent ship speeds of 16.5, 20, 25, and 27 knots, respectively) and time is normalized by the wave maker run time (t_0 = 3.393, 2.8, 2.24, and 2.074 s for equivalent ship speeds of 16.5, 20, 25, and 27 knots, respectively). As discussed in the previous subsection, because of the low level of noise in the large number of position data points, the curves of the computed velocities of wave profile features are highly noisy. Thus, in order to get the velocities shown in the figure, the smoothing technique discussed in the above subsection on the contact point motion was used. In the figure, the last point before the wave crest detaches from the wave board (for subsequent times the highest point of the profile moves from the contact point to the wave crest) occurs in the range $u/u_{max} = 1 \pm 0.1$. Note that the curves for the horizontal velocities of the points of maximum height in Figure 5.28 closely follow the curves for the top drive channel until the drive channel reaches its maximum speed. Thereafter, the highest point moves to the crest and its horizontal velocity continues to increase to a maximum of about $1.8u_{max}$. The maximum value depends on the equivalent ship speed but there is no clear trend in the data. While these curves seem to be a good representation of the horizontal velocity of the contact point, the crest velocity is probably more accurately calculated by fitting a straight line to the data (see the curves of transverse position of the crest versus x ($t = x/U$) in Figure 5.26) than using the above-described local derivative calculation method. Horizontal crest velocities obtained with this linear fit are discussed in the section on scaling at the

end of this chapter.

The curves of the dimensionless vertical velocity all increase to a maximum early in the motion and then fall to near zero at $t/t_0 = 0.2$. The maximum of the curves increases monotonically from about $0.5u_{max}$ at 16.5 knots to $0.75u_{max}$ at 27.0 knots and the time of the maximum increases monotonically from about $0.4t_0$ to $0.75t_0$ as well.

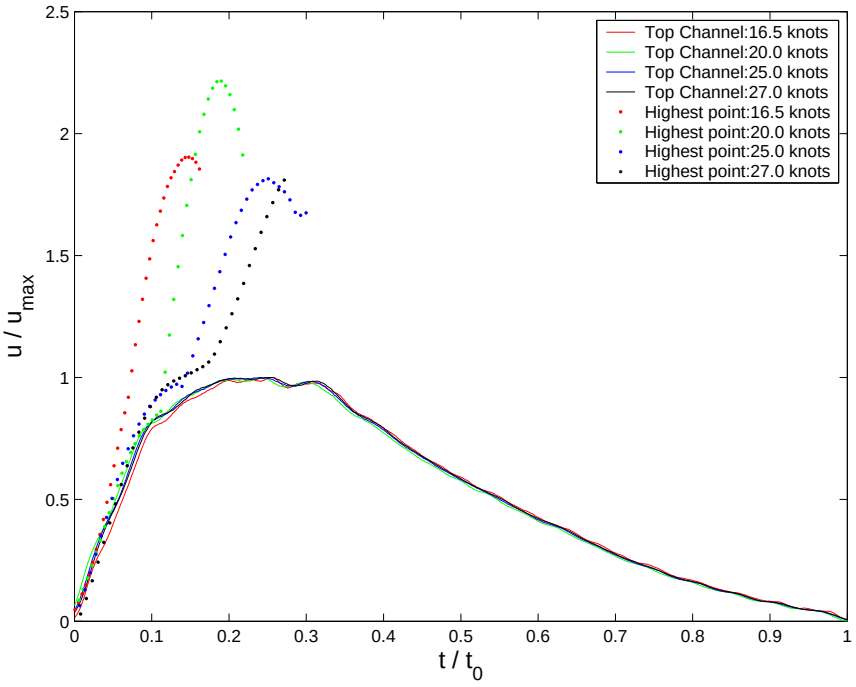

Figure 5.28: Horizontal (y-component) velocity of the highest point on the wave profile at various equivalent ship speeds as a function of time; $t_0 = 3.393$, 2.8, 2.24, and 2.074 s and $u_{max} = 0.82$, 0.996, 1.24, and 1.34 m/s for equivalent ship speeds of 16.5, 20, 25, and 27 knots.

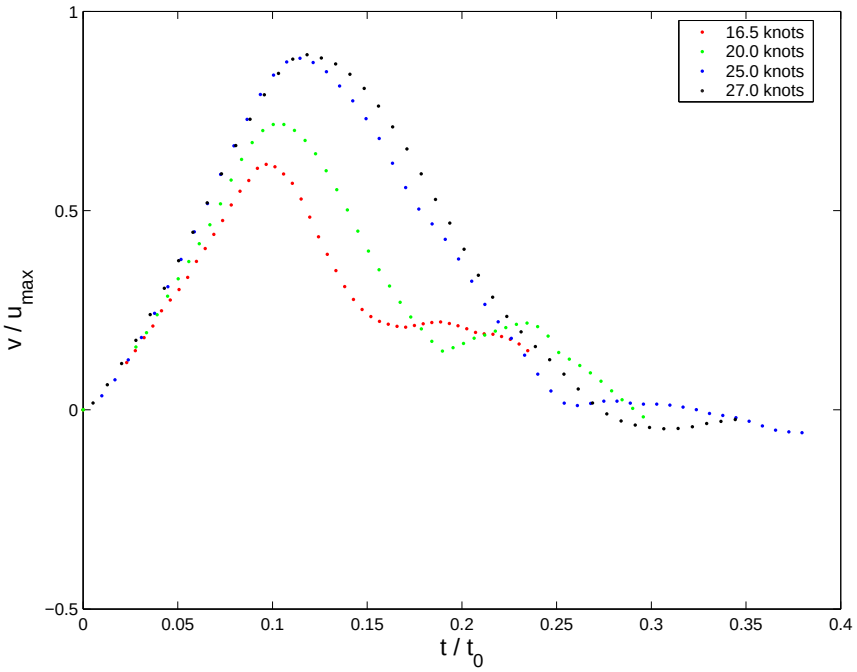

Figure 5.29: Vertical (z-component) velocity of the highest point on the wave profile at various equivalent ship speeds as a function of time; t_0 = 3.393, 2.8, 2.24, and 2.074 s and u_{max} = 0.82, 0.996, 1.24, and 1.34 m/s for equivalent ship speeds of 16.5, 20, 25, and 27 knots.

5.4.3 Jet properties

Some characteristics of the plunging jet were also obtained from the wave profiles. Understanding this feature of the bow wave breaker is important for understanding the air entrainment process. Many researchers have identified jet thickness, velocity and impact angle as key features for modeling air entrainment by plunging jets. In the present experiments, the trajectory of jet tip including the jet impact point on the front face of the wave and the magnitude and direction of the jet tip velocity were measured. The jet thickness could not be measured as we were unable to see inside the cavity under the jet with the present equipment in the Hydrodynamics Laboratory. This measurement is planned using a bore scope in future experiments.

Figure 5.30 shows the trajectories of the jet tip at equivalent ship speeds of 25 and 27 knots. The horizontal axis is the position of the jet tip in the transverse direction normalized by the beam and the vertical axis is the height of the jet tip normalized by the draft. (In this series of experiments, out of four equivalent ship speed cases that we tested, only two of them had plunging jets. Thus, only two curves are shown in the figure.) As seen in the figure, the jet begins to fall as soon as it forms and its y position continuously increases. Analysis shows that the jet tip travels a parabolic path until it impinges the front face of the wave. The vertical acceleration of the tip is found to be 8.5 and 7.6 m/s^2 for the 25 and 27 knot cases, respectively. It is not surprising that the vertical acceleration is different from the acceleration of gravity, since the jet tip is a geometrical feature of the surface rather

than the center of mass of a material body. Inspection of the jet tip trajectory reveals that the jet impacts the free surface at a point which is higher than the undisturbed water surface.

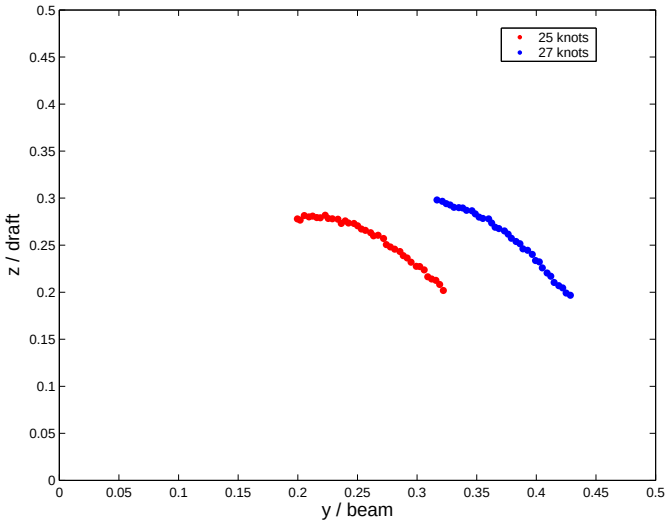

Figure 5.30: Trajectories of the jet tip of the bow wave generated by 2D+T wave maker at various equivalent ship speeds in yz-plane; beam(b)=2.82 m and draft(d)=.914 m.

Figure 5.31 shows the three-dimensional location of the jet impact point in the reference frame of the equivalent ship as a function of Froude number. As seen in the figure, as the equivalent ship speed increases, the jet impacts the front face of the wave further away from the ship centerline in the transverse direction and closer to the ship stem in the streamwise direction.

Since the horizontal (y) and vertical (z) positions of the jet tip are available at all times, the horizontal (u) and vertical (v) components of the velocity of the jet tip can be calculated by differentiating the curves $y(t)$ and $z(t)$, respectively. The

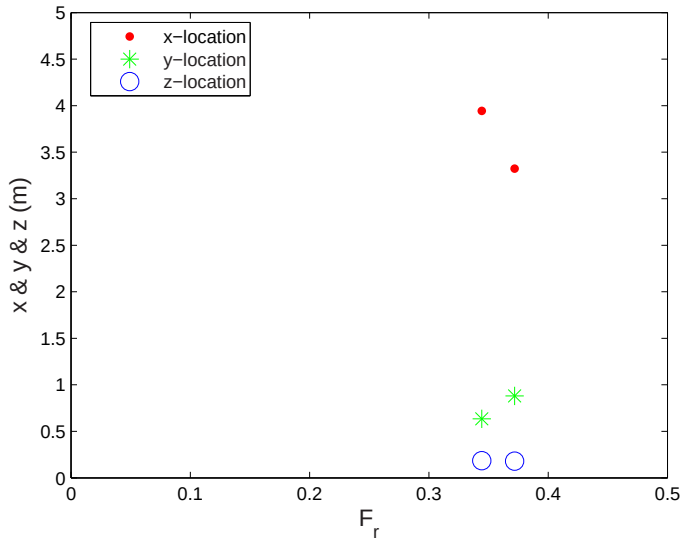

Figure 5.31: Three-dimensional location of the jet impact point as a function of various Froude numbers ($F_r = u_m/\sqrt{gL_m}$, where g is gravity, u_m and L_m are the speed and length of the equivalent 3D ship model).

jet impact speed can be calculated through

$$v_j = \sqrt{u_i^2 + v_i^2} \tag{5.1}$$

where u_i and v_i are the horizontal and vertical components of the jet tip velocity at the time of impact on the free surface. Figure 5.32 shows the jet impact speed as a function of Froude number. The jet speeds were normalized by their corresponding equivalent ship model speeds, u_m. As can be seen in the figure, there is little change in the normalized speed between the two Froude numbers. In future experiments, we plan to use a wider range of equivalent ship speeds that produce plunging jets in order to further explore this result.

Using the horizontal and vertical components of the velocities of the jet tip at

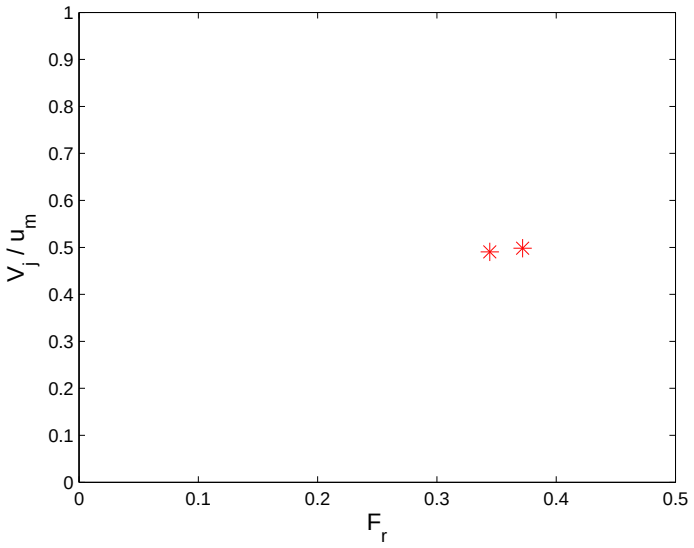

Figure 5.32: Jet impact speed (v_j/u_m, where u_m is the speed of the equivalent 3D ship model) versus Froude number ($F_r = u_m/\sqrt{gL_m}$, where g is gravity, u_m and L_m are the speed and length of the equivalent 3D ship model).

the time of impact, the angle of incidence of the jet can be obtained,

$$\alpha = \tan^{-1}(v_i/u_i). \tag{5.2}$$

This angle is measured relative to the undisturbed free surface and is plotted as a function of Froude number in Figure 5.33. As seen in the figure, the incidence angle is about 25° and increases slightly increases as the Froude increases.

5.4.4 Splash properties

Understanding the plunging jet and resulting splash behaviors are important in the sense that they are crucial in the generation of vorticity and circulation and the entrainment of air. Once the plunging jet hits the front face of the wave, a splash appears in front of the impact point. The water in the splash is probably

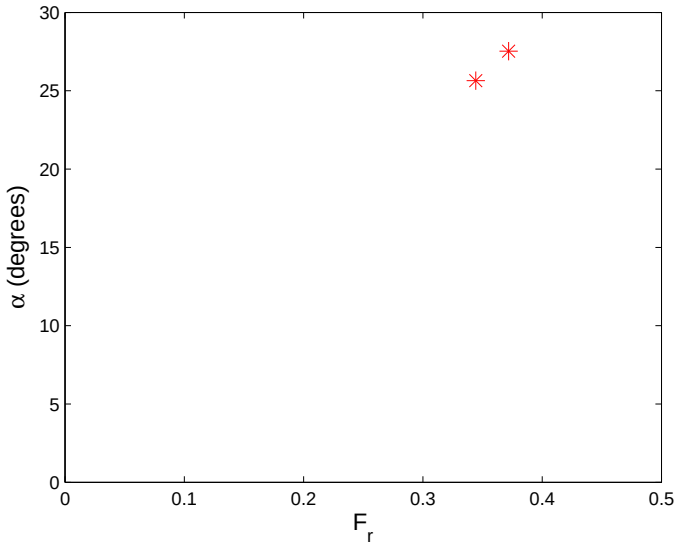

Figure 5.33: Jet incidence angle relative to undisturbed water surface for various Froude numbers ($F_r = u_m/\sqrt{gL_m}$, where g is gravity, u_m and L_m are the speed and length of the equivalent 3D ship model).

composed of water from the jet and water from below the impact point. The closure of the cavity resulting from the jet formation and impact creates a clockwise rotating vortex as seen from a point of view with the wave moving from left to right. The main splash projects forward in the form of two-phase flow. The impact of this air-water mixture on the undisturbed free surface occurs over a large area, entraps a great deal of air and creates another clockwise vortex.

Obtaining the profile of the splash is exceedingly difficult because of the poorly defined free surface of this air-water mixture. The only reliable quantity that could be measured was the height of the splash peak. Figure 5.34 shows the trajectories of the splash peak at equivalent ship speeds of 25 and 27 knots. The maximum height of the splash is almost the same ($\approx 0.45d$) for these two ship speeds. Note that the

maximum height of the splash in both cases goes even higher than the corresponding maximum height of the wave crest ($\approx 0.36d$ and $0.38d$ for equivalent ship speeds of 25 and 27 knots, respectively), see Figure 5.25.

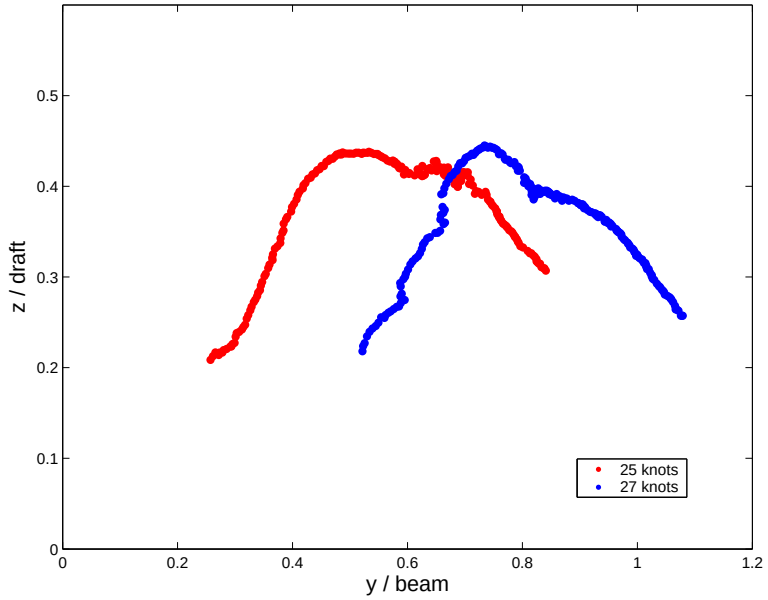

Figure 5.34: Trajectories of the splash peak at various equivalent ship speeds in yz-plane; beam(b)=2.82 m and draft(d)=.914 m.

5.5 The effects of Froude number on the bow wave characteristics

5.5.1 The effects of the Froude number on the contact point height

The effects of changes in the equivalent ship model speed on the maximum height of the contact point are studied. The maximum height of the contact point is plotted against the Froude number in Figure 5.35. As the speed of the ship model and consequently the Froude number increases, the maximum height of the contact point increases monotonically. A curve was fitted onto the four points in order to

obtain a mathematical form for this data. A functional form of $z_{max}/d = AF_r^n$, where A and n are unknown constants, was used. This function has the advantage of automatically going through the assumed data point at the origin of the plot. (The maximum contact line height should be zero for zero Froude number, i.e. zero forward speed.) The constants of the function were obtained using the least squares method applied to a straight line in log-log coordinates. Our results indicate that the maximum height of the contact point scales with the Froude number to the power of 1.67.

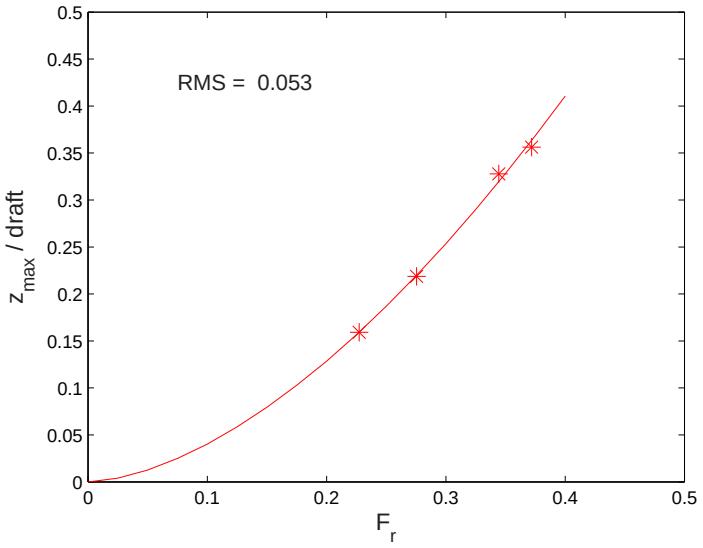

Figure 5.35: Maximum height of the contact line at various Froude numbers ($F_r = u_m/\sqrt{gL_m}$, where g is gravity and u_m and L_m are the speed and length of the equivalent 3D ship model); asterisk: data points; solid line: $z_{max}/d = 1.9F_r^{1.67}$.

5.5.2 The effects of the Froude number on the wave crest characteristics

The maximum height of the bow wave is plotted against Froude number in Figure 5.36. This figure shows a monotonically increasing bow wave height with increasing Froude number. As in the contact point maximum-height plot discussed in the previous section, the functional form $z_{max}/d = AF_r^n$, where A and n are unknown constants, was used to obtain a mathematical form for the data. The least squares method resulted in $n = 1.15$ in this case.

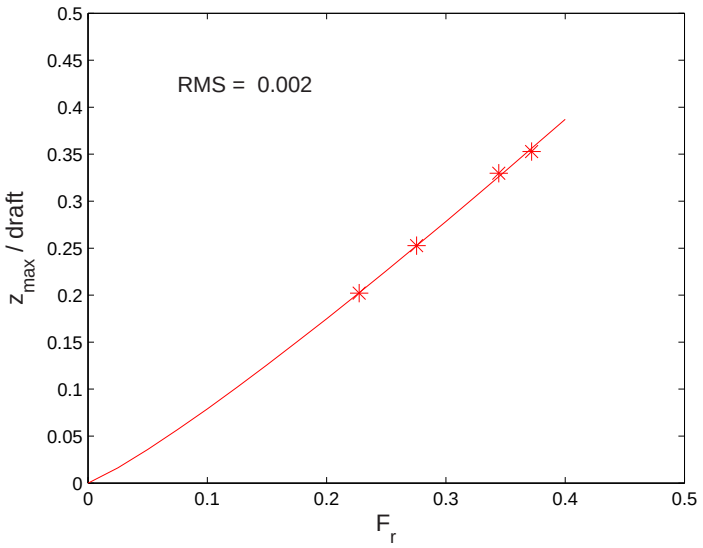

Figure 5.36: Maximum height of the wave crest at various Froude numbers ($F_r = u_m/\sqrt{gL_m}$, where g is gravity and u_m and L_m are the speed and length of the equivalent 3D ship model); asterisk: data points; solid line: $z_{max}/d = 1.1F_r^{1.15}$.

The effects of the equivalent ship speed on the bow wave crest angle and the y-component of the wave crest speed were also studied. Figure 5.37 shows how the bow wave angle changes with Froude number. As mentioned earlier in this chapter,

the bow wave angle is the angle between the crest line and the ship center line as seen from above in the equivalent 3D ship model system. Our data shows that as the Froude number increases, the wave angle remains nearly constant with an average value of about 24° and an RMS variation of ±1.2°.

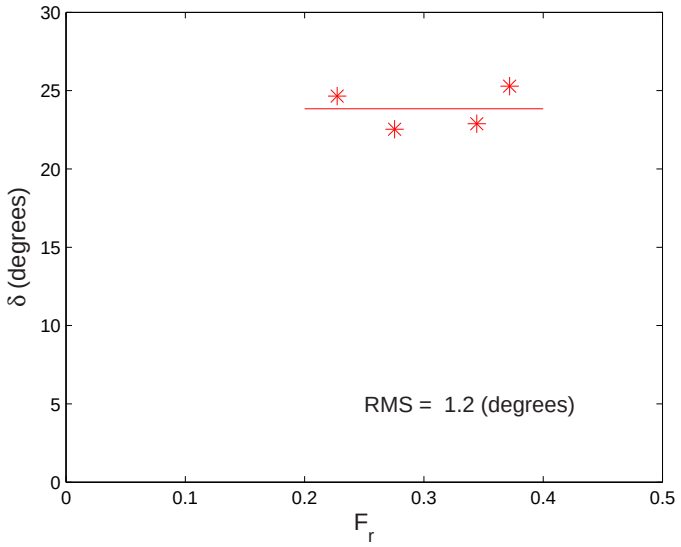

Figure 5.37: Divergent wave angle with the ship model centerline at various Froude numbers ($F_r = u_m/\sqrt{gL_m}$, where g is gravity, u_m and L_m are the speed and length of the equivalent 3D ship model); asterisk: data points; solid line: average value.

Figure 5.38 shows how the y-component of the bow wave phase velocity changes with Froude number. The phase velocity is normalized with the corresponding ship model speed. There is little deviation of the data points about their average value of about $0.45u_m$, where u_m is the speed of the equivalent 3D ship model. The RMS value is only $0.02u_m$. This average value also translates to $1.8u_{max}$, where u_{max} is the maximum speed of the top 2D+T wave maker drive channel.

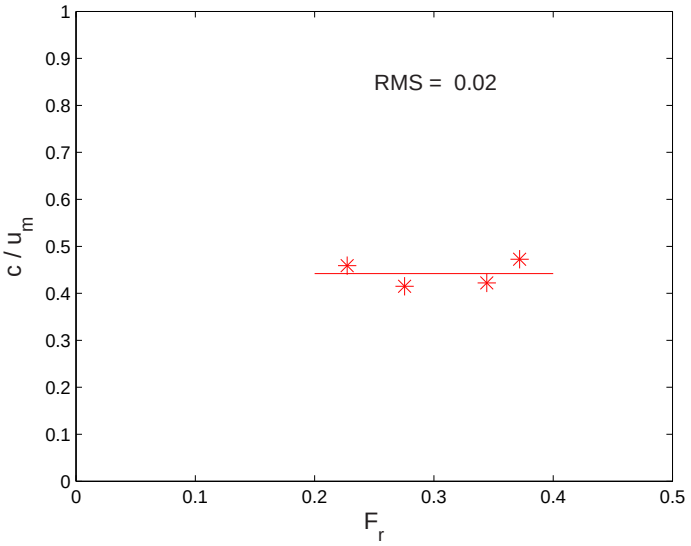

Figure 5.38: The y-component of the bow wave phase velocity (c/u_m, where u_m is the speed of the equivalent 3D ship model) versus Froude number ($F_r = u_m/\sqrt{gL_m}$, where g is gravity and L_m is the length of the equivalent 3D ship model); asterisk: data points, solid line: average value.

Chapter 6

Conclusions and future work

This dissertation is part of a larger investigation of the dynamics of breaking bow waves. The full research program is aimed at understanding the relationships between the breaking waves, the hull shape, and the Froude number; the entrainment of air bubbles into the flow; and the generation of turbulence and vorticity. In order to produce waves that are large enough to correctly model the effects of surface tension and therefore produce realistic air entrainment, a technique known as 2D+T that is used in numerical analysis was adapted to the laboratory. In the 2D+T technique, a two-dimensional wave maker moves horizontally and deforms in a manner that mimics the profile of the three-dimensional ship hull as it passes a fixed vertical plane oriented perpendicular to the ships path. The wave profile at each instant in time (t) corresponds to the wave profile in the 3D ship at a cross stream plane located at $x = Ut$, where U is the speed of the equivalent ship model.

In this thesis, the 2D+T experimental facility was developed and tested, an extensive series of measurements of the time history of the water surface profiles for four equivalent ship speeds was performed, and a holographic system for measuring bubble size distributions and motions was developed and tested in a bench top experiment. Detailed accomplishments and conclusions of this work are given below.

- The first 2D+T wave maker was installed, perfected and tested. Ship models simulated by this wave maker can have drafts as large as 0.914 m and the waves produced typically are on the order of 2 m in length. These waves are very energetic and produces large clouds of air bubbles during breaking.

- Cinematic and photographic evidence indicates that the spilling and plunging breaking bow waves, the splashing during plunging jet impact and the location and behavior of the regions of bubbly flow are qualitatively the same in the 3D ship flow and the 2D+T flow.

- The water surface/hull contact line trajectories for the 2D+T wave maker and the corresponding 3D ship model are quite similar even though the large sonar dome in the 3D model can not be simulated by the 2D+T wave maker (or 2D+T calculations).

- The main wave crest produced by the 2D+T wave maker moves at a speed of $0.45u_m$, where u_m is the the speed of the equivalent 3D ship model, for all equivalent ship speeds tested herein. Note that $0.45u_m = 1.8u_{max}$, where u_{max} is the maximum speed of the top wave maker drive channel in each case.

- The trajectories of the the maximum height of the wave converted into an equivalent 3D ship model system are straight lines. The bow wave angle, which is the angle between the wave crest line and the ship center line, remains remains almost constant with an average value of about 24° and an RMS variation of ±1.2°.

- The maximum height (z_{max}) of the main wave crest produced by the 2D+T wave maker increases monotonically with equivalent 3D ship model speed according to $z_{max}/d = 1.1F_r^{1.15}$, where d is the draft, and $F_r = u_m/\sqrt{gL}$, where L is the length of the equivalent 3D ship model.

- The maximum height ($z_{c_{max}}$) of the free surface contact line produced by the 2D+T wave maker increases monotonically with equivalent 3D ship model speed according to $z_{max}/d = 1.9F_r^{1.67}$.

- The jet created by the breaking wave impacts the front face of the wave at a speed of about $0.5u_m$, where u_m is the the speed of the equivalent 3D ship model, for equivalent ship speeds of 25 and 27 knots. Also, the jet incidence angle relative to undisturbed water surface was found to be about 25° for equivalent ship speed of 25 knots and slightly increases as the Froude number increases.

- It was found that the maximum height of the splash is almost the same ($\approx 0.45d$) for equivalent ship speeds of 25 and 27 knots and the maximum height of the splash in both cases goes even higher than the corresponding maximum height of the wave crest ($\approx 0.34d$ and $0.37d$ for equivalent ship speeds of 25 and 27 knots, respectively).

- Modified in-line holography is an effective method for measuring bubble populations in the 2D+T experiments.

As mentioned before, this thesis is part of a larger project, which is still going

on. A few ideas for future work are listed as below:

- Exploration of the wave pattern and flow field around a second ship model should be pursued to compare with the present results.
- A detailed investigation of scaling with geometric hull shape parameters for ships with flat side walls at various angles of inclination to the undisturbed water surface using the current wave maker.
- Flow field measurements in the breaking waves using particle image velocimetry.
- Exploration of the splash characteristics resulting from the plunging jet impact to characterize its content.
- Employment of a bore scope system to see inside the cavity under the plunging jet in order to obtain information about the jet thickness and the air entrainment process.
- Employment of the holographic PIV system for bubble size and motion measurements.
- Development of a shadowgraph technique for bubble measurements in the later stages of breaking when moderate size bubbles are in the flow.
- Development of an impedance-based probe for bubble measurements in the early stages of breaking when large bubbles exist in the flow.

BIBLIOGRAPHY

[1] Adrian R. J., 1991, Particle imaging techniques for experimental fluid mechanics, *Annual Review of Fluid Mechanics*, **23:** 261-304.

[2] Barnhart D. H., R. J. Adrian and G. C. Papen, 1994, Phase-conjugate holographic system for high resolution particle image velocimetry, *Applied Optics*, **33:** 7159-7170.

[3] Battjes J. A. and T. Sakai, 1981, Velocity field in a steady breaker, *Journal of Fluid Mechanics*, **111:** 421-437.

[4] Blackshire J. L. , W. M. Humphreys and S. M. Bartram, 1994, 3-dimensional, 3-component velocity measurements using holographic particle image velocimetry (HPIV), *AIAA Paper*, **94:** 2645.

[5] Bonmarin P., 1989, Geometric properties of deep-water breaking waves, *Journal of Fluid Mechanics*, **209:** 405-433.

[6] Bouguet J. Y., 2004, Camera Calibration Toolbox for Matlab, http://www.vision.caltech.edu/bouguetj/calib_doc, MRL: Intel Corp.

[7] Chan R. K. and R. L. Street, 1970, A numerical model for water waves, *Technical Report, Department of Civil Engineering, Stanford University*, **135**.

[8] Chen G., C. Kharif, S. Zaleski and J. Li, 1999, Two-dimensional Navier-Stokes simulation of breaking waves, *Physics of Fluids*, **11**(1)**:** 121-133.

[9] Cointe R., 1990, Numerical simulation of a wave channel, *Engineering Analysis with Boundary Elements*, **7**(4)**:** 167-177.

[10] Cointe R. and M. P. Tulin, 1994, A theory of steady breakers, *Journal of Fluid Mechanics*, **276:** 1-20.

[11] Collier R., C. Burckhardt and L. Lin, 1971, Optical Holography, Academic Press, New York.

[12] Dabiri D., and M. Gharib, 1997, Experimental investigation of the vorticity generation within a spilling water wave, *Journal of Fluid Mechanics*, **346:** 113-139.

[13] Dommermuth D. G., D. K. P. Yue, R. H. Rapp, E. S. Chen and M. K. Melville, 1988, Deep-water breaking waves: a comparison between potential theory and experiments, *Journal of Fluid Mechanics*, **89:** 432-442.

[14] Dong R. R., J. Katz, and T. T. Huang, 1997, On the structure of bow waves on a ship model, *Journal of Fluid Mechanics*, **346:** 77-115.

[15] Duncan J. H., 1981, An experimental investigation of breaking waves produced by a towed hydrofoil, *Proceedings of the Royal Society of London, Series A*, **377:** 331-348.

[16] Duncan J. H., 1983, The breaking and nonbreaking resistance of a two-dimensional hydrofoil, *Journal of Fluid Mechanics*, **126:** 507-520.

[17] Duncan J. H., H. Qiao, H. Behres and J. Kimmel, 1994, The formation of a spilling breaker, *Physics of Fluids*, **6:**(8) 2558-2560.

[18] Duncan J. H., H. Qiao, V. Philomin and A. Wenz, 1999, Gentle spilling breakers: crest profile evolution, *Journal of Fluid Mechanics*, **379:** 191-222.

[19] Gabor D., 1948, A new microscopic principle, *Nature*, **161:** 777.

[20] Goodman J. W., 1968, Introduction to Fourier Optics, McGraw-Hill, New York.

[21] Gray C. and C. A. Greated , 1993, A processing system for the analysis of particle displacement holograms , In *Optical Diagnostics in Fluid and Thermal Flow, SPIE Proc.*, **2005:** 636.

[22] Grilli S. T., J. Skourup, and I. A. Svendsen, 1989, An efficient boundary element method for nonlinear water waves, *Engineering Analysis with Boundary Elements*, **6**(2)**:** 97-107.

[23] Jahne B. and P. Giebler, 1994, *Proceedings of the Conference on Computer Vision and Pattern Recongnition*, Seattle, 20-23 June.

[24] Kerman B. R., 1988, Sea surface sound- Natural mechanisms of surface generated noisein the ocean, Dordrecht, Kluwer, 639.

[25] Lammare E. and W. K. Melville, 1991, Air entrainment and dissipation in breaking waves, *Nature*, **351:** 469-472.

[26] Lammare E. and W. K. Melville, 1992, Instrumentation for the measurement of void-fraction in breaking waves - Laboratory and field results, *IEEE Journal of Oceanic Engineering*, **17**(2)**:** 204-215.

[27] Lammare E. and W. K. Melville, 1994, Void-fraction measurements and sound speed fields in bubble plumes generated by breaking waves, *Journal of Acoustical Society of America*, **95:** 1317-1328.

[28] Lessard, R. R., and S. A. Zieminski, 1971, Bubble coalescence and gas transfer in aqueus electrolytic solutions, *Ind. Eng. Chem. Fundam.*, **10:** 260-269.

[29] Lin J. C. and D. Rockwell, 1994, Instantaneous structure of a breaking waves, *Physics of Fluids*, **6:**(9)**:** 2877-2879.

[30] Lin J. C. and D. Rockwell, 1995, Evolution of a quasi-steady breaking waves, *Journal of Fluid Mechanics*, **302:** 29-44.

[31] Longuet-Higgins M. S., 1960, Mass-transport in the boundary layer at a free oscillating surface, *Journal of Fluid Mechanics*, **8:** 293-306.

[32] Longuet-Higgins M. S., 1992, Capillary rollers and bores, *Jouranal of Fluid Mechanics*, **240:** 659-679.

[33] Longuet-Higgins M. S., 1996, Capillary jumps on deep water, *Journal of Physical Oceanography*, **26**(9)**:** 1957-1965.

[34] Longuet-Higgins M. S., 1997, Progress towards understanding how wave break, *Proceedings of the 21th Symposium on Naval Hydrodynamics*, pp. 7-28, Trondheim, Norway, June 1996.

[35] Longuet-Higgins M. S. and E. D. Cokelet, 1976, The deformation of steep surface waves on water. I. A numerical method of computation. *Proceedings of the Royal Society of London, Series A*, **358:** 157-184.

[36] Longuet-Higgins M. S. and J. S. Turner, 1974, An entraining plume model of a spilling breaker, *Journal of Fluid Mechanics*, **63:** 1-20.

[37] Meng H. and F. Hussain , 1995, In-line recording and off-axis viewing (IROV) for holographic particle image velocimetry, *Applied Optics*, **34:** 1827-1840.

[38] Miller M., T. Nennstiel, J. H. Duncan, A. A. Dimas, and S. Prostler, 1999, Incipient breaking of steady waves in the presence of surface wakes, *Journal of Fluid Mechanics*, **383:** 285-305.

[39] Miyata H., 1980, Characteristics of nonlinear wavesin the near-field of ships and their effects on resistance, *Proceedings of the 13th Symposium on Naval Hydrodynamics*, 335-351. Shipbuilding Research Association of Japan.

[40] Miyata H. and T. Inui, 1984, Nonlinear ship waves, *Advances in Applied Mechanics*, **24:** 215-288.

[41] Monahan E. C. and C. R. Zeitlow, 1969, Laboratory comparisons of fresh-water and salt-water whitecaps, *Journal of Geophysical Research*, **74:** 6961-6966.

[42] Monahan E. C., Q. Wang, X. Wang, and M. B. Wilson, 1994, Air entrainment by breaking waves: A Laboratory assessment, *Aeration Tech. ASME Fluids Engineering Division*, **187:** 21-26.

[43] New A. L., P. McIver and D. H. Peregrine , 1985, computations of overturning waves, *Journal of Fluid Mechanics*, **150:** 233-251.

[44] Peregrine D. H. and I. A. Svendsen, 1978, Spilling breakers, bores, and hydrolic jumps, *16th International Conference on Coastal Engineering*, Hamburg, New York, Aug. 27-Sep. 3, pp. 540-550.

[45] Rapp R. and W. K. Melville, 1990, Laboratory measurements of deep water breaking waves. *Philosophical Transactions of the Royal Society of London, Series A*, **331:** 735-800.

[46] Roth G. L., D. T. Mascenik and J. Katz, 1999, Measurements of the flow structure and turbulence within a ship bow wave, *Physics of Fluids*, **11**(11)**:** 3512-3523.

[47] Schultz W. W., J. Huh and O. M. Griffin, 1994, Potential energy in steep and breaking waves, *Journal of Fluid Mechanics*, **278:** 201-208.

[48] Slauenwhite D. E. and B. D. Johnson , 1999, Bubble shattering: Differences in bubble formation in fresh water and seawater, *Journal of Geophysical Research*, **104**(C2)**:** 3265-3275.

[49] Stokes G. G., 1880, Consideration relative to the greatest height of oscillatory irrotational waves which can be propagated without change of form, *Mathematical and Physical Papers* **1:** 225-228, Cambridge University Press.

[50] Tulin M. P., 1996, Breaking of ocean waves and downshifting, *Waves and Nonlinear Processes in Hydrodynamics*, Ed. J. Grue, B. Gjevik and J. E. Weber, 177-190. Dordrecht, Neth.: Kluwer Acad.

[51] Tulin M. P. and M. Wu, 1996, Divergent bow waves, *Proceedings of the 21th Symposium on Naval Hydrodynamics*, Trondheim, Norway, June 1996.

[52] Wang P., Yao Y. and M. P. Tulin, 1994, Wave group evolution, wave deformation, and breaking: simulation using LONGTANK, a numerical wave tank, *International Jouranl of Offshore and Polar Engineering*, **4**(2)**:** 200-205.

[53] Wang Q. and E. C. Monahan, 1995, The influence of salinity on the spectra of bubbles formed in breaking wave simulations, *Sea Surface Sound 94*, M. J. buchingham and J. R. Potter, Eds., World Scientific, 312-319.

[54] Zhang J. and J. Katz, 1994, Off-axis HPIV with forward light scattering from particles, *Proceedings of the ASME Fluids Engineering Division summer Meeting*, **191:** 173-177.

[55] Zhang J., B. Tao and J. Katz, 1997, Turbulent flow measurement in a square duct with hybrid holographic PIV, *Experiments in Fluids*, **23:** 373-381.